UNIVERSITY OF NOVA GORICA
SCHOOL OF APPLIED SCIENCES

STUDIES FOR THE COMMISSIONING OF FERMI@ELETTRA: A FREE-ELECTRON LASER BASED ON THE PRINCIPLE OF SEEDED HARMONIC GENERATION

MASTER'S THESIS

Jurij Urbančič

ADVISERS:
Prof. Dr. Giovanni De Ninno
Dr. Simone Di Mitri

Ajdovščina, 2011

UNIVERZA V NOVI GORICI
FAKULTETA ZA APLIKATIVNO NARAVOSLOVJE

PREUČEVANJE ZAGONA FERMI@ELETTRA: LASER NA PROSTE ELEKTRONE, KI TEMELJI NA PRINCIPU GENERIRANJA HARMONIK

MAGISTRSKO DELO

Jurij Urbančič

MENTORJA:
Prof.Dr. Giovanni De Ninno
Dr. Simone Di Mitri

Ajdovščina, 2011

Povzetek

Cilj projekta je prispevati k razvoju novega laserja na proste elektrone (ang. Free Electron Laser - FEL), ki bo služil kot izvor močnega, ultra-hitrega, koherentnega sevanja. Pokrival bo široko spektralno območje od VUV do mehkih rentgenskih žarkov. FERMI@Elettra je prvi obrat, ki temelji na principu generiranja harmonik. Izvor elektromagnetnega polja, ki interagira z elektroni v undulatorju je zunanji (seed) laser. Posledično pride na koncu undulatorja do koherentnega sevanja elektronov z izbrano harmoniko zunanjega laserja. Brez zunanjega laserja ne dosežemo koherentnega sevanja. Princip delovanja zunanje seed konfiguracije je bil eksperimentalno dokazan, vendar ostajajo številna vprašanja odprta. Med drugimi: a) občutljivost časovne in spektralne stabilnosti FEL-a glede na fluktuacijo elektronskega snopa in zunanjega laserja; b) učinek dinamike elektronskega snopa na delovanje FEL-a; c) možnost dosega meje Fourierjeve transformacije optičnega pulza.

Naš cilj je definirat začetne eksperimentalne pogoje in predvideti pričakovano delovanje FELa. Zagon FELa vključuje poskusno dejavnost (diagnostika in optimizacija FEL delovanja) in primerjavo med teoretičnimi napovedmi in eksperimentalnimi rezultati. Magistrska naloga temelji na sodelovanju med Univerzo v Novi Gorici (Slovenija) in Sincrotrone Trieste Elettra laboratory (Italija), kjer je dejavnost tudi potekala.

Ključne besede: laser na proste elektrone, sinhrotron, sinhrotronska svetloba, ultra-relativistični snop elektronov, undulator, rentgenski žarki, vakuumska ultravioličná svetloba, FERMI@Elettra, Elettra, generiranje harmonik, preučevanje zagona.

Abstract

Aim of this project is to contribute to the development of a new Free-Electron Laser (FEL) source for the generation of powerful, ultra-fast, coherent radiation in a wide spectral region, ranging from VUV to soft X-rays. FERMI@Elettra is the first facility based on the principle of seeded harmonic generation. In a seeded FEL, the electromagnetic field interacting with electrons at the beginning of the undulator is provided by an external, high power, laser (the seed). As a result, at the end of the undulator electrons emit coherent radiation at the harmonics of the seed wavelength. Such a longitudinal (temporal) coherence is instead not achieved in unseeded FEL's. The working principle of the seeded approach has been experimentally demonstrated, but several issues remain currently open. Among others: a) the sensitivity of temporal and spectral FEL output stability to unavoidable shot-to-shot fluctuations of electron beam and seed laser characteristics; b) the impact of electron-beam dynamics (e.g., microwave and wakefield instabilities, coherent synchrotron radiation) on FEL performance; c) the possibility of generating Fourier transform limited optical pulses.

Our goal is to define the start-up experimental conditions and predict the expected performance of FEL. The FEL commissioning involved the experimental activity (i.e., diagnostics and optimization of the FEL output) and in the comparison between theoretical predictions and experimental data. This master thesis is based on the joint FEL activities carried out at the Sincrotrone Trieste Elettra laboratory (Italy) and at the University of Nova Gorica (Slovenia).

Key words: free electron laser, synchrotron, synchrotron radiation, ultra-relativistic electron beam, undulator, X-rays, vacuum ultraviolet radiation, FERMI@Elettra, Elettra, harmonic generation, commissioning studies.

Acknowledgements

First of all, I would like to thank my advisors Giovanni De Ninno and Simone Di Mitri for their guidance throughout my work, help and valuable suggestions. A big thanks goes also to Benoit Mahieu, Eugenio Ferrari, Carlo Spezzani, Enrico Allaria, and others of the Accelerators Group at Elettra who provided me with the necessary help during my visit. Last, but not least, I want to express my gratitude to my parents and to grandparents for their unconditional support throughout my studies.

Contents

Povzetek i

Abstract ii

Acknowledgements iii

1 Introduction 1

- 1.1 From synchrotron radiation to Free Electron Lasers 1
- 1.2 FEL Principle and Configurations 3
  - 1.2.1 Oscillator Configuration 3
  - 1.2.2 Single-pass configuration 4
- 1.3 The Scientific Case 5
- 1.4 FELs: state of the art 6
- 1.5 Outline of this Thesis 7

2 Accelerator and FEL physics 9

- 2.1 Introduction 9
- 2.2 Beam Optics and Dynamics 9
  - 2.2.1 Transverse Particle Dynamics 11
  - 2.2.2 Longitudinal Particle Dynamics 13
  - 2.2.3 Wakefield Effects 17
- 2.3 Undulators 18
  - 2.3.1 Undulator Field 18
  - 2.3.2 Equations of motion in an undulator 20
  - 2.3.3 Undulator Radiation 21
- 2.4 The Free Electron Laser 22
  - 2.4.1 Equations of motion for electrons in the FEL 24
  - 2.4.2 Amplification of the FEL in the low gain regime 26
  - 2.4.3 FEL amplification in the high gain regime 27
  - 2.4.4 Bunching 28
  - 2.4.5 Harmonic Generation 30

3 The FERMI Facility **33**
3.1 Introduction . . . 33
3.2 Principle of Operation . . . 34
3.3 General Layout . . . 35
3.4 The Photoinjector . . . 36
  3.4.1 Electron Source and RF Gun . . . 37
  3.4.2 Photocathode and Drive Laser Systems . . . 37
3.5 Accelerator . . . 38
  3.5.1 Overview of Design Specifications . . . 38
  3.5.2 Bunch Compressor . . . 39
3.6 Undulators . . . 40
3.7 The Seed Laser . . . 41
3.8 Experimental Area . . . 42
3.9 Expected Performance . . . 44

4 Commissioning of the FERMI FEL **45**
4.1 Introduction . . . 45
4.2 Measurements of the Electron Beam . . . 45
  4.2.1 Electron Generation and Acceleration . . . 46
  4.2.2 Beam Profile . . . 48
  4.2.3 Energy Spread Measurement . . . 50
  4.2.4 Time Jitter . . . 50
  4.2.5 Emittance Measurements . . . 52
4.3 Seed Laser and Electron Beam Overlap . . . 56
  4.3.1 Spatial Overlap . . . 56
  4.3.2 Temporal Alignment . . . 57

5 Generation of Coherent Harmonics **61**
5.1 Introduction . . . 61
5.2 Measurement of the FEL Emission . . . 61
  5.2.1 Optimization of the FEL Emission . . . 62
  5.2.2 FEL Spectrum . . . 65
5.3 Effect of the Seed Laser on the Electron Bunch . . . 67
5.4 Bunch Length Compression . . . 68

6 GENESIS Simulations **71**
6.1 Introduction . . . 71
6.2 Preliminary (time-independent) Calculations . . . 71
6.3 Expected Performance: Time-Dependent Mode . . . 73
  6.3.1 Seed Laser . . . 74
  6.3.2 Electron Beam . . . 74
  6.3.3 Performance . . . 75
6.4 Comparison: Experiments vs. Simulations . . . 79

7 Conclusion and Perspective **81**

A Description of GENESIS parameters **83**

B Input files for GENESIS **85**

Bibliography **87**

List of Figures

1.1 An electron beam passing through an undulator of period λ_u 2

1.2 Historical evolution of peak brightness [3]. 3

1.3 Target wavelength and linac energy of present and future FELs in single-pass configuration. SASE: VISA (USA), SCSS (Japan), FLASH (Germany), SPARC (Italy), Japanese-XFEL, European-XFEL, LCLS (USA). Seeded HG: DUV-FEL (USA), FERMI (Italy), Arc-en-ciel (France), BESSY-FEL (Germany). 6

1.4 Comparison between X-FEL projects and 3rd generation synchrotron light sources in terms of peak brightness [16]. 7

2.1 Coordinate system to describe the motion of particles in the vicinity of the nominal trajectory. 10

2.2 The phase space ellipse of particle motion in the x-x' plane. 12

2.3 Wideroe linac structure [22]. 14

2.4 Phase space diagrams for a synchronous phase $\psi_s = \pi$ [23]. 17

2.5 Schematic view of a planar undulator magnet with alternating polarity of the magnetic field and of the sine-like trajectory of the electrons. 18

2.6 Determination of the constants of integration from the field value B_0 in the middle of poletip. 19

2.7 Intensity distribution of the undulator radiation. 22

2.8 Electron motion in the FEL field. The phase shift relative to the laser wave is ploted along the horizontal axis, and the energy difference from the resonance energy is plotted vertically. Two different types of electron motion are plotted and may be visualized in terms of corresponding pendulum motion. 26

2.9 Amplification or gain curve of the FEL [28]. 27

2.10 Motion of electrons with a flat phase distribution as they pass through the FEL. a) shows the motion when $\gamma_{\text{start}} = \gamma_r$ and b) the motion when $\gamma_{\text{start}} > \gamma_r$ [29]. 28

2.11 Bunching evolution. a) Electrons are randomly distributed in phase (initial condition). b) Electrons start bunching in a λ_s scale and the wave is eventually amplified. 29

2.12 Evolution of the electron-beam phase space of one wavlength of the seed laser. a) initial distribution, b) energy modulation c) spatial modulation (bunching) d) slightly overbunching e-f) overbunching [30]. 30

2.13 Seeded Harmonic Generation scheme. 31

2.14 Evolution of the bunching in an electron bunch. 31

3.1 A view of the FERMI facility. 33
3.2 FERMI@Elettra machine layout, including a) the linear accelerator, b) the undulator hall and c) the experimental hall. The SP1 to SP6 points are location of the electron beam spectrometer lines for beam dump and diagnostics. 35
3.3 The photoinjecor at FERMI. 36
3.4 The FERMI@Elettra FEL photoinjector. a) RF Gun, b) Solenoid, c) Pop-in screens, d), e) booster accelerating sections. 37
3.5 The accelerator hall. 39
3.6 Bunch compressor diagnostics layout. 40
3.7 Undulator hall of FEL-1. 41
3.8 The seed laser system. (a) Ti:Sapphire oscillator, (b) Ti:Sapphire amplifier, (c) diode laser. 42
3.9 The beam dump area. 43
3.10 The experimental area. 43

4.1 (*Up*) Spot of the photoinjecor laser and (*down*) its temporal profile. 46
4.2 Q.E. map before (*left*) and after (*right*) the Ozone gas treatment. This map of the photocathode Q.E. over the region of interest is obtained by sweeping a small size laser spot over the cathode and measuring the emitted electron current. 47
4.3 Scan of the charge measured by a Faraday cup vs. RF phase of the gun. The arrow indicates the selected phase. 47
4.4 Deflection of the electron bunch: the centroid remains on axis while at the end of the bunch the transverse force F_t has opposite directions. 48
4.5 Vertical deflection of the uncompressed electron beam on a YAG screen. 49
4.6 Vertical deflection of the electron beam compressed with factor $\sim$6 on a YAG screen. 49
4.7 The electrons trajectory in a bunch compressor. 51
4.8 Layout of the FERMI BC1 area. A collimator is used in case we want to select just parts of the electron bunch. 51
4.9 Time jitter as a function of the bunch length compression factor. 52
4.10 Parabolic fitting of horizontal beam size σ_x^2 as a function of $Z = kl$ for a compressed bunch with $E_{\text{tot}} = 322.79$ MeV. 55
4.11 Normalized emittance measurement done in the BC1 area vs the compression factor. The dashed square is horizontal emittance ε_x and thick circle is the vertical emittance ε_y. 56
4.12 Seed laser and the electron beam at the a) beginning and b) end of the modulator, before the alignment. 57
4.13 Seed laser and the electron beam at the a) beginning and b) end of the modulator, after the alignment. 57
4.14 Optical transition radiation (OTR) and seed laser on electron-optical sampling (EOS) CCD. 58
4.15 OTR and seed laser a) before and b) after the temporal overlap. 59

5.1 Intensity of the coherent emission, measured by means of a fast photodiode. The trace a) shows the time profile of a single pulse with the photodiode. The b) trace shows a sequence of seeded FEL pulses and c) is the spontaneous emission of the electron beam. 62
5.2 Seed laser temporal delay scan vs. FEL intensity. 63
5.3 FEL intensity vs. seed laser power scan. 63
5.4 Intensity vs. the dispersive section strength. 64
5.5 (*Left*) The output intensity as a function of the tuned gap of the modulator. (*Right*) The output intensity as a function of the tuned gap of the radiators. 64
5.6 Comparison between an a) non optimized and b) optimized FEL emission, acquired on a YAG screen. 65
5.7 Layout of PADReS. 65
5.8 Non optimized spectrum of FEL radiation at 52 nm. 66
5.9 The spectrum of coherent harmonic radiation at 52 nm. 66
5.10 The effect of the seed laser on the electron beam. The arrow indicates the spot of the interaction of the electron beam with the seed laser. 67
5.11 The appearance of a second peak in the FEL spectrum due to the overbunching and chirp in the electron beam distribution. 68
5.12 FEL with uncompressed electron beam: more stable, less intense. 69
5.13 FEL with compressed electron beam (compression factor 4): less stable, more intense. 69

6.1 Output power at 52 nm as a function of the seed power. 72
6.2 Output power at 52 nm as a function of the dispersive section strength (in "GENESIS" units). 72
6.3 Output power as a function of the tuned wavelength of the modulator. 73
6.4 The output power as a function of the tuned wavelength of the radiator. 73
6.5 Temporal profile of the seed laser. 74
6.6 a) The profile of the electron bunch in terms of current vs. time; b) the electron beam energy (in GENESIS units) at the beginning of the modulator vs. time. 75
6.7 The electron beam energy profile at radiator exit. 75
6.8 (*Top*) Bunching at the beginning of the modulator and (*bottom*) bunching at the entrance of the radiator. 76
6.9 Bunching profile at the exit of the radiators. 77
6.10 a) The temporal profile and b) spectrum of the harmonic signal with the electron beam in slight overbunching. 77
6.11 The electron beam in deep overbunching. 78
6.12 a) The output power and b) FEL spectrum. 78

List of Tables

2.1 The most important multipoles in beam steering and their principal effects on the beam motion. 10

3.1 Nominal electron beam and FEL parameters. 34
3.2 Temporal specifications for the UV laser pulse. 37
3.3 Main electron beam specifications. 39
3.4 The expected electron beam and FEL performance. 44

4.1 Energy spread at different energies and at different positions (shown in Fig. 2.2, Chapter 2) along the linac. 50
4.2 Horizontal emittance measured at the end of the linac for different compression factors. 56
4.3 Seed laser parameters. 57

6.1 Main Parameters used to during the time dependent simulations. 74
6.2 Comparison between experiments and simulations. 79

A.1 A description of the input parameters for GENESIS simulations. 83

B.1 The input files for GENESIS simulations. 85

Chapter 1

Introduction

The need of coherent and intense pulsed radiation is spread among many research disciplines, such as biology, nanotechnology, physics, chemistry and medicine [1]. The synchrotron light, produced by the spontaneous (incoherent) emission of relativistic electrons passing through magnetic devices, only partially meets these requirements. A new kind of light source has been conceived and developed in the last decades, the result of a continuous effort of improving the performance of available light sources. This source is the Free Electron Laser (FEL).

1.1 From synchrotron radiation to Free Electron Lasers

It is well known that a charged particle in acceleration emits electromagnetic radiation. When the energy of the particle becomes comparable to that of its rest mass, the relativistic effects induce a highly directional emission and a significant increase in the total radiated flux (the number of photons per second per unit area). Such an emission is called synchrotron radiation.

Synchrotron radiation was first observed in 1947 [2] and it was initially considered as a problematic phenomenon, since it caused an undesired loss of the energy of accelerated particles. Only in the 50's it was realized that this radiation could be very useful in all scientific applications in which the structure of a particular material or sample can be studied through its interaction with light.

The first synchrotron light sources relied on accelerators built for elementary particle research, where the particles were accelerated inside the ring. In these devices, the magnetic field of bending and other magnets had to change with particle's energy. This turned out to be very demanding and also very unstable. The problem was solved with storage-rings (SR). Here the preliminary acceleration of particles is achieved by means of an external accelerator. After achieving the desired energy the particles are injected into the storage-ring, where they circulate during many hours. This improved significantly the overall stability of emitted radiation.

The main disadvantage of a storage ring is that in curves the particles radiate over a large cone in the broad angle and thus only a small part of the radiation can be used for experiments. To solve this problem, the light production, initially relying on simple bending magnets (dipoles), was gradually committed to undulators, i.e. array of periodically spaced dipole magnets of alternating polarity. An illustration of the trajectory of an electron beam passing through the undulator is shown in Fig. 1.1. Electrons traversing the periodic magnetic structure are forced to undergo oscillations and therefore produce radiation that is much more intense and concentrated in an angle and energy spectrum significantly narrower than in the case of a simple dipole magnet. Undulators also allow us to produce radiation with different polarization (from planar to elliptical).

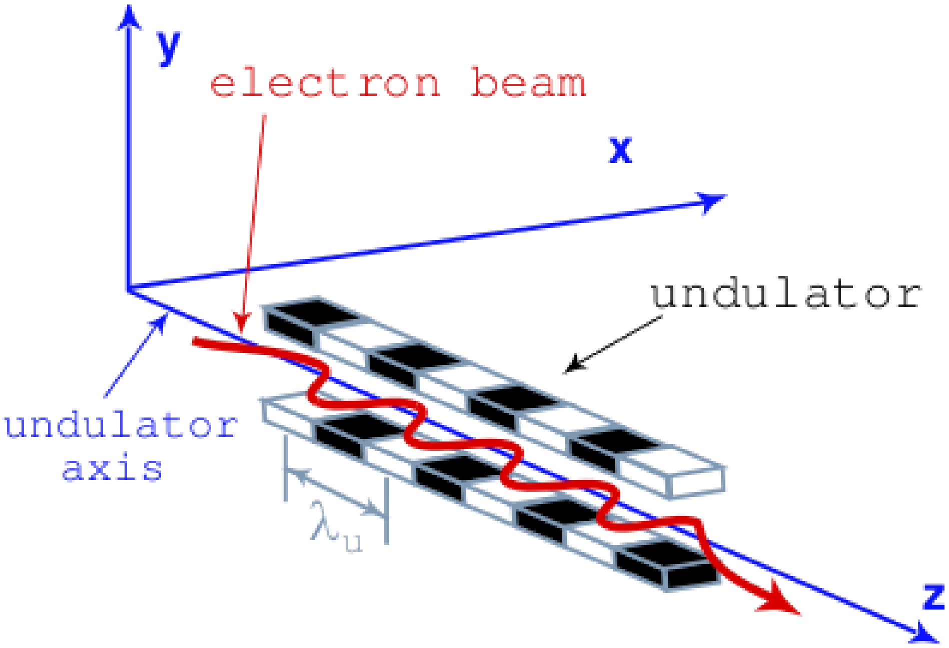

Figure 1.1: An electron beam passing through an undulator of period λ_u

Today's synchrotron light sources take full advantage of undulators' feature and are designed with long dedicated straight sections to incorporate these devices. This allowed to achieve an increase in peak brightness (defined as the number of photons per pulse per unit solid angle, emitted from the unit surface of the source in a given frequency band) of around 11-12 orders of magnitude, if compared to the first synchrotrons. The evolution of synchrotron light sources in terms of peak brightness is shown in Fig. 1.2.

After this impressive development, the development of light sources based on the electron beams has now reached a crossroad. In fact, detailed studies have shown that the brightness of radiation from synchrotrons can not be increased significantly due to the limit reached in peak current and emittance.

For the next generation of UV/X-ray sources, the scientific community has oriented itself towards the development of devices that are not based on the spontaneous emission from electrons when they pass through magnetic structures, but relies instead on the interaction of the electron beam with a co-propagating electromagnetic field. Under proper conditions, the interaction between the particles and the field can result in the coherent amplification of the co-propagating wave, at both its original (fundamental) wavelength and at its higher harmonics. A device based on this principle is called FEL. The electron beam can be provided by a linear accelerator (linac) or a storage-ring.

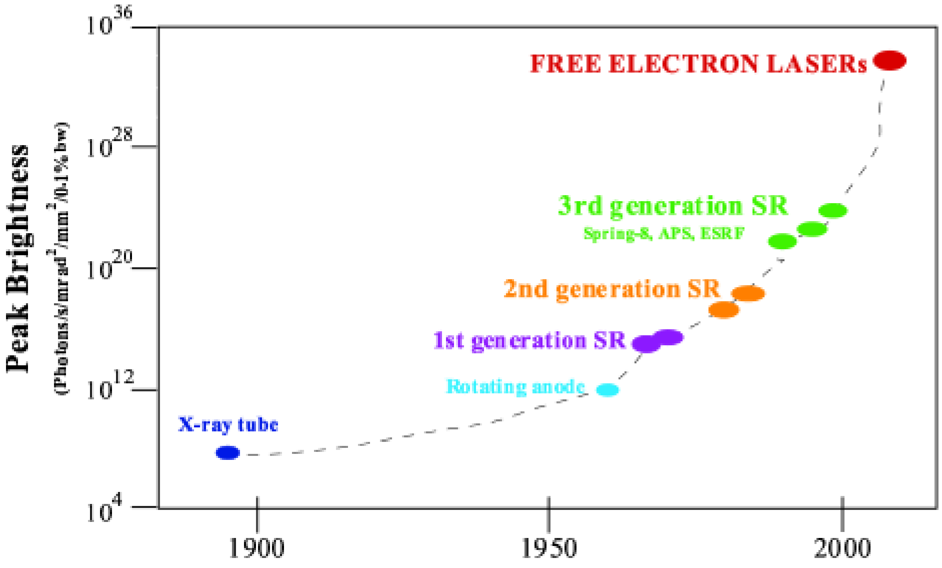

Figure 1.2: Historical evolution of peak brightness [3].

1.2 FEL Principle and Configurations

Potentially, the FEL radiation is temporally and spatially coherent, almost Fourier transform limited, has a high flux and can be tuned over a wide range of wavelengths (from angstroms to hundreds of micrometers/few millimeters). In some configurations this radiation has also a variable polarization as well as a stable temporal structure. The FEL principle relies on the stimulated emission from a relativistic electron beam propagating in the static and periodic magnetic field provided by an undulator. The wavelength of the stimulated emission is fixed by the electron beam energy and by the characteristics of the undulator field. The stimulated emission is induced when electrons interact with an electromagnetic wave that co-propagates with them through the undulator. If the wave that initiates the process (seed) is coherent, the electrons emit radiation which is also coherent. Two main FEL configurations can be distinguished: the single-pass configuration, where the amplification of the electromagnetic wave occurs in one passage through the undulator, and the oscillator configuration, in which the electromagnetic wave is stored in an optical cavity and lasing is achieved as the result of a large number of light-electron interactions inside the undulator.

1.2.1 Oscillator Configuration

The oscillator configuration is characterized by an optical cavity that encloses the undulator (or a couple of undulators with a magnetic chicane in between, i.e., the optical klystron). Generally, the electron beam can be provided either by a linear accelerator or a storage ring. The first case is usually related to FELs that produce infrared radiation. The second option concerns FELs in the visible-UV range. This kind of devices have been developed since the second generation of storage-ring light sources.

The circulating electron bunches produce synchrotron radiation passing through the magnetic field provided by the optical klystron. The emitted radiation is stored into the optical cavity and amplified during many successive interactions with the electron beam until lasing is achieved. The FEL radiation, being fully coherent, may act as a seed for the generation of high order harmonics of the fundamental wavelength which is stored in the optical cavity. These harmonics are not amplified turn after turn because they are not stored in the optical cavity. Indeed, the optical cavity mirrors have a narrow-band (few nm) high reflectivity, which is centered around the fundamental wavelength.

1.2.2 Single-pass configuration

In the single-pass configuration, the amplification of the co-propagating wave is achieved in one passage of the electron beam. We can distinguish two processess - the Self Amplified Spontaneous Emission (SASE) [4] and Harmonic Generation (HG) [5]. In the SASE process a linear accelerator (linac) provides the electrons that pass through a long (tens of meters) chain of undulators. The spontaneous emission produced by electrons at the entrance of the undulator couples to the beam itself and gets amplified. SASE sources are relatively simple to implement (if compared to externally seeded FELs) and are characterized by very high brightness. However, they show an incoherent temporal structure, resulting from the envelope of a series of micro-pulses with random intensity and duration.

The lack of temporal coherence can be overcome using a coherent seed to drive the process. In this case the electrons behave as an active medium to generate radiation at the harmonics of the seed. The most efficient HG scheme relies on at least two independent undulators, the second one being tuned to one of the harmonics of the first. The external seed, e.g. a laser, is focused in the first undulator and synchronized with the incoming electron bunch. The laser-electron interaction produces energy modulation in the particle distribution. This modulation is converted in spatial separation (bunching) in a short magnetic section placed between the undulators, called dispersive section. Performing a Fourier analysis, the spatial bunch distribution shows harmonic components of the fundamental wavelength. Therefore, in the second undulator the electron beam emits coherent radiation at the selected harmonic wavelength. The higher the harmonic number, the lower the efficiency of the process. Therefore, in order to reach the VUV/X-ray spectral range, the seed laser wavelength has to be as short as possible. Unfortunately, below 200 nm there are no conventional lasers with enough peak power ($\sim$100 MW) and the desired tunability.

It is important to stress that new-generation single-pass FELs are based on linear accelerators [6]. Electron bunches delivered by such devices are generally characterized by higher peak current and lower relative energy spread compared to bunches circulating into a SR. As a consequence, linac-based FELs can be expected to produce optical pulses with energy three-four orders of magnitude larger than the ones produced by SR-based FELs. However, for SR-based FELs, due to re-circulation of the beam, the mean energy and current distribution are thermalized by long-lasting periodic dynamics. Hence, in principle, these sources are characterized by an excellent shot-to-shot stability. Vice versa, successive electron bunches delivered by a linac are generally characterized by significant fluctuations of the mean electron beam energy and current. This may result in a remarkable shot-to-shot fluctuations of the emitted harmonic power

[7]. Moreover, SR allows to produce harmonic pulses at relatively high repetition rate (order of 1 kHz or even higher) to the benefit of average harmonic power. Only FELs based on superconducting linacs can reach analogous performance, while normal conducting devices are limited to repetition rates of the order of 100 Hz. Finally, the coherent FEL light generated by a SR is naturally synchronized to the synchrotron radiation emitted by undulators and bending magnets. This makes easier the design and the realization of pump-probe experiments.

1.3 The Scientific Case

Four classes of information, depending on the photon energy, can be extracted from the study of the interaction of radiation with matter [8]. Electronic processes in the valence band and collective mode excitations in elastic and inelastic scattering processes can be studied using photons with energy between the UV and far VUV regions (wavelength between 200 nm and 40 nm).

Photons in the extremely soft X-ray range ($\lambda \sim$10 nm) allow to taking advantage of the specificity of shallow core levels of chemical elements to obtain phase contrast images, also by microscopy. Photons with wavelength around 1 nm, comparable to the typical inter-atomic distances, are mainly used in materials science, in particular to study deeper core levels, such as the L2, L3 edges of transition metals, and thus of many magnetic systems, superconductors and highly correlated electronic systems. They also allow the study of the K-edges of oxygen and carbon, which are the main constituents of organic and biological materials and are used in technological applications such as nano-fabrication. From the above one can conclude that radiation sources with wavelength in the UV (200 nm) to soft X-ray (1 nm) range have great relevance for the very large and important fields concerning the study of chemical, physical and material properties suitable for technological applications.

If one adds to the high brilliance, typical of FEL radiation, polarization and control of the beam temporal structure, one sees that it becomes possible to study the mechanisms of structural dynamics of a wide range of materials and material states, covering both hard and soft matter.

To study ultra-fast dynamics (from picoseconds to femtoseconds) in matter, one can use the pump-probe (or stroboscopic) technique, based on exciting a sample with a suitable wavelength (pump) followed by probing the excited sample with a radiation pulse, in general of a different wavelength, whose duration is shorter than the characteristic time of the process under observation. The delay time between the pulses is optically controlled so that the short pulse works as a probe of the temporal evolution of the process under observation. The two wavelengths can be delivered by the same source or from two (appropriately correlated) different sources.

FERMI@Elettra is a single-pass FEL located next to the third-generation synchrotron radiation facility ELETTRA. The FERMI project is divided in two phases called FEL-1 and FEL-2. FEL-1, covering the 100 to 20 nm wavelength range, is designed to operate in the time domain and in two complementary modes of operation: a) high stability mode and b) a high intensity mode. FEL-2, covering the 20 to 4 nm wavelength range, is designed to operate in the frequency domain (high energy resolution) and with relatively long photon pulses ($\sim$ 1 ps). These design choices will yield a source quite unique among the other FELs under construction or proposed for construction in Europe, USA and Japan.

1.4 FELs: state of the art

In order to set a frame of reference for the experimental results presented in this thesis, the current status of the FEL sources is described here, focusing in particular on next-generation single-pass FELs, since this is the configuration used at FERMI@Elettra. Linac-based FELs aim at providing radiation with pulse length of about hundreds of femtoseconds in the soft and hard X-ray range. Some prototypes have been realized in the recent past in order to test both the SASE and Harmonic Generation principles. Among experiments in SASE regime, LEUTL (Low Energy Undulator Test Line) (Advanced Photon Source, Argonne, USA) has reached the 530 nm (2000) [9]; VISA (Visible to Infrared SASE Amplifier) at Accelerator Test Facility of Brookhaven National Laboratory (USA), produced FEL radiation at 840 nm (2001) [10]; TTF (Tesla Test Facility) [or FLASH (Free-electron LASer in Hamburg)] at DESY (Germany), reached the 4.12 nm (2010) [11]; SCSS (Spring-8 Compact SASE Source) at Spring-8 (Japan) down to 50 nm (2006) [12] and LCLS (Light Coherent Light Source) at Standford (USA) reached 0.15 nm (2009) [13]. The High Gain Harmonic Generation (HGHG) scheme has been tested at Deep Ultra Violet - FEL (National Synchrotron Light Source, BNL, USA) and reached harmonic radiation at 193 nm (2006) [14]. Seeding was achieved at SPARC FEL and they reached 197 nm in 2010 [15]. Another facility based on the seeded configuration is FERMI@Elettra that reached 17 nm in 2011.

The projects under development based on SASE are: SCSS XFEL (Spring-8, Japan) 0.1 nm in 2011, and European XFEL (DESY, Germany) 0.1 nm in 2014.

Other proposed seeded-FELs are: Soft X-ray FEL (Berlin, Germany) with shortest wavelength 1.2 nm, Arc-en-ciel (Saclay, France), shortest wavelength: 1 nm. An overview of the main projects is given in Fig. 1.3.

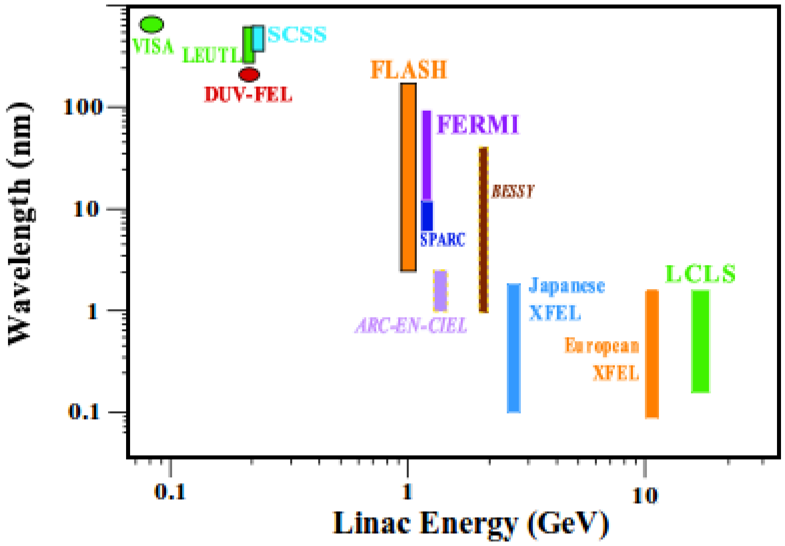

Figure 1.3: Target wavelength and linac energy of present and future FELs in single-pass configuration. SASE: VISA (USA), SCSS (Japan), FLASH (Germany), SPARC (Italy), Japanese-XFEL, European-XFEL, LCLS (USA). Seeded HG: DUV-FEL (USA), FERMI (Italy), Arc-en-ciel (France), BESSY-FEL (Germany).

The improvement in terms of peak brightness of the X-FEL projects with respect to a typical 3rd generation synchrotron light source (such as Elettra) is of several orders of magnitude, as shown in Fig. 1.4. As it can be seen, FELs based on storage-rings (SRFELs) produce a radiation with intermediate brightness.

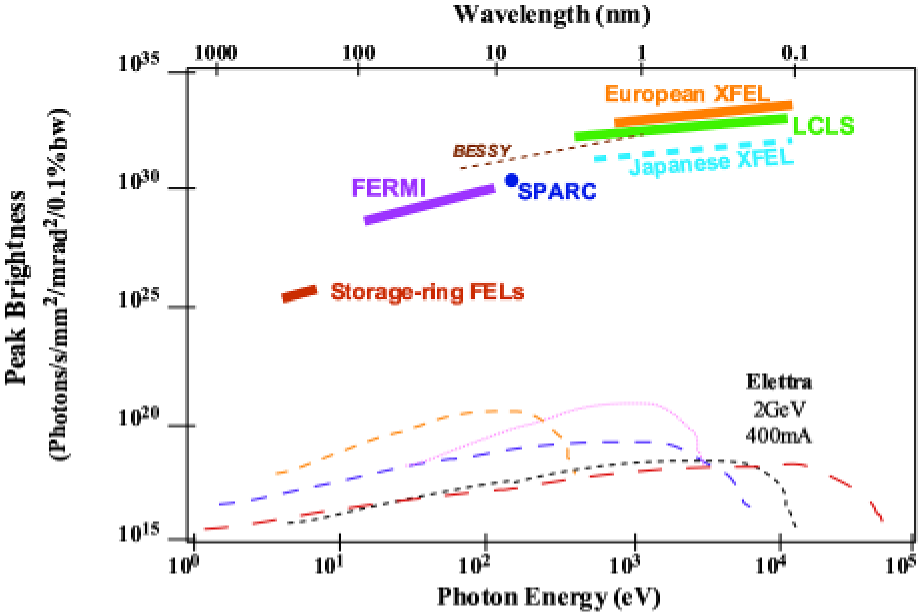

Figure 1.4: Comparison between X-FEL projects and 3rd generation synchrotron light sources in terms of peak brightness [16].

The seeded single-pass configuration has been implemented only three times on storage-ring FELs. Proof of principle of generation of coherent harmonic radiation at 355 nm was first performed at LURE (Orsay, France) using a Nd:YAG laser [17]. Coherent emission at 260 nm, the third harmonic of a Ti:Sapphire laser, was observed at UVSOR (Okazaki, Japan) [18]. The last case was Elettra SRFEL that reached 87 nm in 2009. One of the key parameters of light sources is the pulse duration, which determines the temporal scale of the physical (or chemical, or biological) process that is possible to investigate. Presently, the trend is to work with pulse durations of the order of 100 fs (rms). In the near future, the aim is to reach below the femtosecond scale, approaching as much as possible the attosecond range.

1.5 Outline of this Thesis

In this thesis we go through the commissioning of the FERMI@Elettra and present the results obtained in harmonic generation. We also performed simulations to get a comparison between theoretical predictions and experimental data.

The structure of this work is the following. Chapter 2 reviews the basic accelerators and FEL physics used in this work. Chapter 3 is devoted to the description of the FERMI@Elettra single-pass FEL facility. In Chapter 4 we present the most important part of my thesis, the commissioning of the FERMI FEL. The main goal is to characterize the electron beam inside the linear accelerator and activate the FEL. Chapter 5 is dedicated to the presentation of the harmonic generation and characterization of the source. We also optimized the FEL emission in order to make it available to the users. In Chapter 6 we present the GENESIS simulation of the coherent harmonic radiation and compare the results with experiments. Chapter 7 reviews the obtained results and gives a conclusion.

Chapter 2

Accelerator and FEL physics

2.1 Introduction

In this chapter we give an introduction to the basic ingredients that are neccesary for the description of the FEL process. Since the FEL is an accelerator-based light source, the main components are an accelerator that provides a relativistic electron beam and an undulator magnet. For this reason we must start with accelerator physics and particle beam dynamics. We can distinguish between linear and circular accelerators. In circular accelerators the particles follow a closed path over and over again and so cover an extremely large total path length within the accelerator. Our focus is on linear accelerators, since this is the configuration used at FERMI.

2.2 Beam Optics and Dynamics

When an accelerator is constructed, the nominal trajectory of the particle beam is fixed. Circular machines (such as storage rings) may have a complicated trajectory shape consisting of numerous curves connected by straight sections. The trajectory may also be a straight line, as is the case in linear accelerators. Individual particles within a beam always have a certain angular divergence, and without further measures the particles would eventually hit the wall of the vacuum chamber and be lost.

Therefore, it is necessary to fix the particle trajectory and repeatedly steer the diverging particles back onto the ideal trajectory. This can be done by means of electromagnetic fields ($\boldsymbol{E}$ and $\boldsymbol{B}$), in which particles of charge e and velocity $\boldsymbol{v}$ experience the Lorentz force

$$\boldsymbol{F} = e\,(\boldsymbol{E} + \boldsymbol{v} \times \boldsymbol{B}) = \dot{\boldsymbol{p}}. \tag{2.1}$$

To describe the motion of a particle in the vicinity of the nominal trajectory we introduce a Cartesian coordinate system $K = (x, z, s)$, whose origin moves along the trajectory of the beam (Fig. 2.1). The axis along the beam direction is s, while the horizontal and veritcal axes are labelled x and z respectively. We assume that the particles move essentially parallel to the s-direction ($\boldsymbol{v} = (0, 0, v_s)$) and the magnetic field has only transverse components and has the form $\boldsymbol{B} = (B_x, B_z, 0)$. For a particle moving in the horizontal plane through the magnetic field there is a balance between the Lorentz force and the centrifugal force that leads us to the relation

$$\frac{1}{R(x,z,s)} = \frac{e}{p} B_z(x,z,s), \tag{2.2}$$

where p is the particle's momentum and R is the radius of curvature of the trajectory.

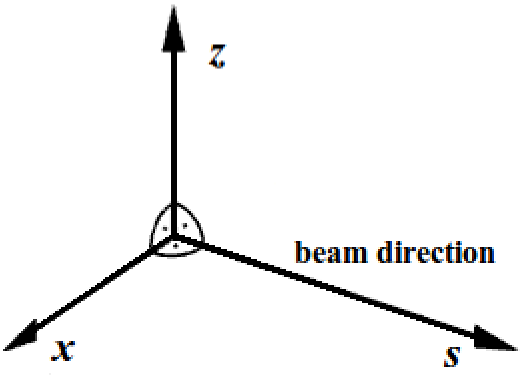

Figure 2.1: Coordinate system to describe the motion of particles in the vicinity of the nominal trajectory.

Since the transverse dimensions of the beam are small compared to the radius of curvature of the particle trajectory, we may expand [19] the magnetic field in the vicinity of the nominal trajectory and get the expression

$$\begin{aligned} \frac{e}{p} B_z(x) &= \frac{e}{p} B_{z0} + \frac{e}{p}\frac{\mathrm{d}B_z}{\mathrm{d}x} x + \frac{1}{2!}\frac{e}{p}\frac{\mathrm{d}^2 B_z}{\mathrm{d}x^2} x^2 + \frac{1}{3!}\frac{e}{p}\frac{\mathrm{d}^3 B_z}{\mathrm{d}x^3} x^3 + \cdots \\ &= \underbrace{\frac{1}{R}}_{\text{dipole}} + \underbrace{\frac{kx}{1}}_{\text{quadrupole}} + \underbrace{\frac{1}{2!} m x^2}_{\text{sextupole}} + \underbrace{\frac{1}{3!} o x^3}_{\text{octupole}} + \cdots . \end{aligned} \tag{2.3}$$

The magnetic field around the beam may be regarded as a sum of multipoles, each of which has a different effect on the path of the particle. The important multipoles and their effects are listed in Table 2.1.

Table 2.1: The most important multipoles in beam steering and their principal effects on the beam motion.

Multipole	Definition	Effect
Dipole	$\frac{1}{R} = \frac{e}{p} B_{z0}$	beam steering
Quadrupole	$k = \frac{e}{p}\frac{\mathrm{d}B_z}{\mathrm{d}x}$	beam focusing
Sextupole	$m = \frac{e}{p}\frac{\mathrm{d}^2 B_z}{\mathrm{d}x^2}$	chromaticity compensation
Octupole	$o = \frac{e}{p}\frac{\mathrm{d}^3 B_z}{\mathrm{d}x^3}$	field errors or field compensation

If the lowest multipoles are used for beam steering in an accelerator we speak of linear beam optics, since the only bending forces present are either constant (dipole field, entering through the bending radius R) or increase linearly with the transverse displacement from the ideal trajectory (quadrupole field, described by the quadrupole strength k). Higher multipoles (sextupole, octupole) are introduced for compensation or field correction.

As the particle travels through the magnetic structure, its position s is uniquely defined for any time t. This allows us to use the derivatives with respect to the spatial coordinate s, $x' = \mathrm{d}x/\mathrm{d}s$ and $z' = \mathrm{d}z/\mathrm{d}s$.

We assume that the particles have a well-defined momentum $p = p_0 + \Delta p$, where the momentum deviation Δp is very small compared to the nominal momentum p_0 (this condition is well satisfied in accelerators). We obtain the linear equations of motion for a particle travelling through the magnetic structure of an accelerator [20]:

$$\begin{aligned} x''(s) + \left(\frac{1}{R^2(s)} - k(s) \right) x(s) &= \frac{1}{R(s)} \frac{\Delta p}{p}, \\ z''(s) + k(s) z(s) &= 0. \end{aligned} \tag{2.4}$$

As a first approximation, the electron motion can be basically considered decupled in longitudinal and transverse components.

2.2.1 Transverse Particle Dynamics

The solution of the longitudidnal component of Eq. (2.4) describes a transverse oscillation about the orbit and is known as betatron oscillation, whose amplitude and phase depend on the position s along the path. To solve this equation, we introduce the beta function $\beta(s)$, also known as the amplitude function. This is a quasi-periodic function given by focusing properties of the lattice (i.e., quadrupoles). We also use the integration constant ε, known as emittance and get

$$x(s) = \sqrt{\varepsilon} \sqrt{\beta(s)} \cos \left[\Psi(s) + \phi \right], \tag{2.5}$$

where

$$\Psi(s) = \int_0^s \frac{\mathrm{d}s}{\beta(s)} \tag{2.6}$$

is the phase advance of oscillation between point "0" and point "s" in the lattice. Within the magnetic structure, which has a net focusing effect, the particles perform betatron oscillation with position-dependent amplitude given by

$$E(s) = \pm \sqrt{\varepsilon \beta(s)}. \tag{2.7}$$

The particles udergo a transverse motion about the orbit within a range marked out by the envelope $E(s)$.

We write the second derivative of the trajectory function $x(s)$ in the form

$$x' = -\frac{\sqrt{\epsilon}}{\sqrt{\beta(s)}} \left(\alpha(s) \cos(\Psi(s) + \phi) + \sin(\Psi(s) + \phi) \right) \tag{2.8}$$

with $\alpha(s) = -\beta'(s)/2$. In order to arrive at an expression describing the particle motion in the x-x' phase space plane, we eliminate the terms which depend on the phase Ψ. From this we get

$$\varepsilon = \gamma(s)x^2(s) + 2\alpha(s)x(s)x'(s) + \beta(s)x'^2(s), \tag{2.9}$$

where $\gamma(s)$ is defined as $(1+\alpha^2(s))/\beta(s)$. This is a general equation of an ellipse in the x-x' plane with the area $A = \pi\varepsilon$. The plot of it is given in Fig. 2.2. The emitance ε with factor π is the are of the phase ellipse. The functions $\alpha(s)$, $\beta(s)$ and $\gamma(s)$ are called Twiss functions.

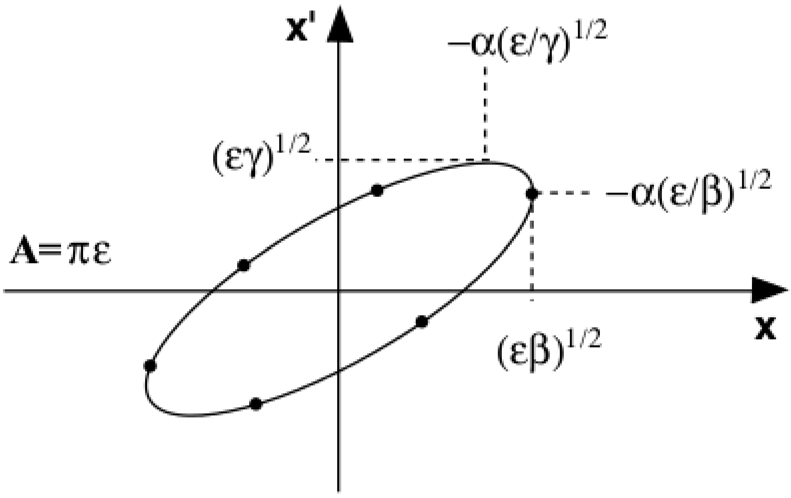
x'
$-\alpha(\varepsilon/\gamma)^{1/2}$
$(\varepsilon\gamma)^{1/2}$
$-\alpha(\varepsilon/\beta)^{1/2}$
$A=\pi\varepsilon$
$(\varepsilon\beta)^{1/2}$
x

Figure 2.2: The phase space ellipse of particle motion in the x-x' plane.

This ellipse is defined by a symmetric, positive-definite matrix called the beam matrix,

$$\sigma = \begin{pmatrix} \sigma_{11} & \sigma_{12} \\ \sigma_{12} & \sigma_{22} \end{pmatrix} = \begin{pmatrix} \langle x^2 \rangle & \langle xx' \rangle \\ \langle xx' \rangle & \langle x'^2 \rangle \end{pmatrix}, \tag{2.10}$$

and the emittance can be calculated as

$$\varepsilon = \sqrt{\det \sigma}. \tag{2.11}$$

The transverse (betatron) motion between point 0 and point s is described in the matrix formalism by

$$\begin{pmatrix} x \\ x' \end{pmatrix}_s = M \begin{pmatrix} x \\ x' \end{pmatrix}_0, \qquad \begin{pmatrix} y \\ y' \end{pmatrix}_s = M \begin{pmatrix} y \\ y' \end{pmatrix}_0 \tag{2.12}$$

with

$$M = \begin{pmatrix} \sqrt{\frac{\beta_s}{\beta_0}}(\cos\Psi_s + \alpha \sin\Psi_s) & \sqrt{\beta_s\beta_0}\sin\Psi_s \\ \frac{(\alpha_0 - \alpha{:}s)\cos\Psi_s - (1+\alpha_0\alpha_s)\sin\Psi_s}{\sqrt{\beta_s\beta_0}} & \sqrt{\frac{\beta_s}{\beta_0}}(\cos\Psi_s - \alpha_s \sin\Psi_s) \end{pmatrix}. \tag{2.13}$$

This transport matrix can be particularized for every optical element which composes a linear accelerator. For a Gaussian particle distribution the beam emittance is defined as

$$\varepsilon = \frac{\sigma_x^2}{\beta_x(s)} \tag{2.14}$$

and the standard deviation of beam size and beam divergence are defined by

$$\begin{aligned} \sigma_x &= \sqrt{\varepsilon_x \beta_x} \;\; \sigma_y = \sqrt{\varepsilon_y \beta_y}, \\ \sigma_{x'} &= \sqrt{\varepsilon_x \gamma_x} \;\; \sigma_{y'} = \sqrt{\varepsilon_y \gamma_y}. \end{aligned} \tag{2.15}$$

2.2.2 Longitudinal Particle Dynamics

Application of radio frequency (RF) fields is exceptionally effective for the acceleration of charged particles. Standing and traveling electromagnetic waves are used in linear accelerators [21]. The degree of acceleration depends on the momentary phase ψ of the field as seen by the particle while traveling through or with an electromagnetic field. Special boundary conditions for accelerating RF-wave must be met such that net acceleration is achieved.

Particle acceleration occurs in short, straight sections along the path. No direct traveling wave exists between adjacent accelerating sections and specific synchronicity conditions must be met for the fields in different accelerating sections to contribute to particle acceleration. For systemic acceleration the phase of the RF field in each of the accelerating sections must reach specific values at the moment the particle arrive. If the phase of the fields in each of N sections is adjusted to be the same at the time of particles arrival, the total acceleration is N times the acceleration of each individual section. This phase is called the synchronous phase ψ_s and is defined by

$$\psi_s = \omega t - ks = \text{const.}, \tag{2.16}$$

where ω is the oscillating frequency of the electromagnetic field and k is its wavenumber. The time derivative vanises and the synchronicity condition is

$$\dot{\psi}_s = \omega - k\beta c = 0, \tag{2.17}$$

since $\mathrm{d}s/\mathrm{d}t = \beta c$. This condition is met if we set

$$k = \frac{2\pi}{L} \tag{2.18}$$

and the frequency of the electromagnetic field is then

$$\omega_1 = k_1 \beta c = \frac{2\pi}{L}\beta c = \frac{2\pi}{\Delta T}, \tag{2.19}$$

where ω_1 is the lowest frequency satisfying the synchronicity condition and ΔT is the time needed for particles with velocity βc to travel the distance L. Also, any integer multiple of the frequency ω_1 satisfies the synchronicity condition and we can define permissible frequencies of the accelerating RF field by

$$\omega_h = h\omega_1 = k_h \beta c = \frac{2\pi}{L} H\beta c = \frac{2\pi}{\Delta T} h, \tag{2.20}$$

where h is an integer called the harmonic number, with $k_h = hk_1$.

In a classical Wideroe linac, fields are generated by an external RF source and applied to a series of metallic drift tubes (Fig. 2.3). Accelerating fields build up at gaps between the tubes while the tubes themselves serve as a field screen for particles during the time the electric field is changing sign and would be decelerating. The length of the field-free drift tubes is determined by the velocity of the particles and is $L = c\beta T_{\mathrm{rf}}$ where T_{rf} is the period of the RF field. As the particle energy increases so does the velocity $c\beta$ and the length L of the tube must increase too. Only when the particles become relativistic will the distance between fields-free drift sections become a constant together with the velocity of the particles.

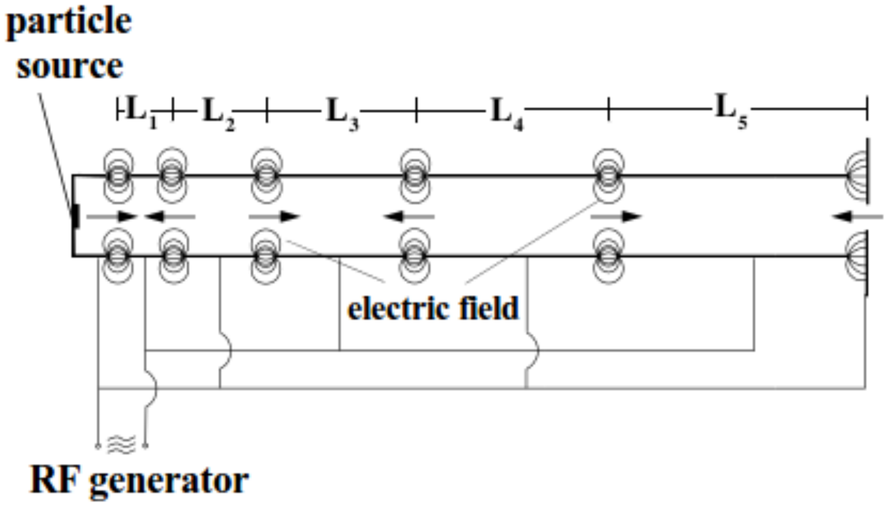

Figure 2.3: Wideroe linac structure [22].

Equations of Motion

Time-of-flight from one gap to the next is the same for all particles while the wavenumber k or the distance between accelerating sections is not. A momentum dependent path length between accelerating sections exists if the lattice between such sections includes bending magnets. The synchronicity condition must be modified to account for such chromatic effects. Removing the restriction of a constant wave number k, we obtain a variation of Eq. (2.17),

$$\Delta\dot{\psi} = -\Delta(k\beta c) = ck\Delta\beta - \beta c \frac{\partial k}{\partial p}\frac{\partial p}{\partial t}\Delta t, \tag{2.21}$$

where

$$k = k_h = h\frac{2\pi}{L_0} = \frac{2\pi}{\lambda_{RF}}. \tag{2.22}$$

The momentum dependence of the wave number comes from the fact that the path length L

between accelerating gaps may be diffrent form the ideal path L_0 for off-momentum particles. The variation of the wave number with particle momentum is

$$\left.\frac{\partial k}{\partial p}\right|_0 = \left.\frac{\partial k}{\partial L}\frac{\partial L}{\partial p}\right|_0 = -\frac{k_h}{p_0}\alpha_c, \tag{2.23}$$

where α_c is the momentum compaction factor. For a linear accelerator the momentum compation factor vanishes since the length of a straight line does not depent on the momentum. With $(\partial p/\partial t)\Delta t = \Delta p$ and $mc\gamma^3\Delta\beta = \Delta p$ we get from Eq. (2.21) with (2.23)

$$\dot{\psi} = -\beta c k_h(\gamma^{-2} - \alpha_c)\frac{\Delta p}{p_0}. \tag{2.24}$$

The term γ^{-2} represents the variation of the particle veloctiy with energy. Even in a linear accelerator where $\alpha_c = 0$, the time of flight between accelerating gaps is energy dependent.

Acceleration is not the only source for energy change of particles. There are also gains and losses from interactions with the vacuum chamber envirement, external fields, synchrotron radiation, etc. We may separate all longitudinal forces into two groups, one for which the energy change depends only on the phase of the accelerating field $V(\psi)$ and the others where the energy change depends only on the energy of the particle $U(E)$ itself. The total energy gain ΔE is in this case

$$\Delta E = eV(\psi) - U(E). \tag{2.25}$$

While the ideal patricle arrives at the accelerating cavities exactly at the synchronous phase ψ_s, most other particles in the beam arrive at slightly different phases. For small deviations $\varphi = \psi - \psi_s$ from the synchronous phase, we get the average rate of change of particle energy with respect to the energy of the synchronous particle

$$\frac{\mathrm{d}}{\mathrm{d}t}\Delta E = \frac{1}{T_0}\left[eV(\psi_s) + e\left.\frac{\mathrm{d}V}{\mathrm{d}\psi}\right|_{\psi_s}\varphi - U(E_0) - \left.\frac{\mathrm{d}U}{\mathrm{d}E}\right|_{E_0}\Delta E\right], \tag{2.26}$$

where the particle energy $E = E_0 + \Delta E$ and $T_0 = L_0/(\beta c)$ is the time-of-flight for the reference particle.

The differential equation of motion for small phase oscillations is

$$\ddot{\varphi} + 2\alpha_s\dot{\varphi} + \Omega^2\varphi = 0, \tag{2.27}$$

where the damping decrement is defined by

$$\alpha_s = \frac{1}{2T_0}\left.\frac{\mathrm{d}U}{\mathrm{d}E}\right|_{E_0} \tag{2.28}$$

and the synchrotron frequency by

$$\Omega^2 = \frac{\beta c k_h \eta_c}{c p_0 T_0} e \left.\frac{\mathrm{d}V}{\mathrm{d}\psi}\right|_{\psi_s}, \tag{2.29}$$

where

$$\eta_c = \left(\frac{1}{\gamma^2} - \alpha_c\right). \tag{2.30}$$

To determine stability criteria, we must make an assumption for the waveform of the accelerating voltage. The RF accelerating field is created in resonant cavities and acceleration voltage can be expressed by sinusoidal waveform $V(\psi) = \hat{V}_0 \sin\psi$ and expanded about the synchronous phase to get

$$V(\psi_s + \varphi) = \hat{V}_0(\sin\psi_s \cos\varphi + \sin\varphi\cos\psi_s). \tag{2.31}$$

Keeping the linear terms in φ, the phase equation is

$$\ddot{\varphi} + \Omega^2\varphi = 0, \tag{2.32}$$

and the synchrotron oscillation frequency becomes

$$\Omega^2 = \frac{ck_h\eta_c}{cp_0T_0} e\cos\psi_s. \tag{2.33}$$

For real values of the synchrotron oscillation frequency the phase equation assumes the form

$$\varphi = \hat{\varphi}\cos\left(\Omega t + \chi_i\right), \tag{2.34}$$

where χ_i is an arbitrary phase function for particle i at time $t = 0$. Any particle with a momentum different from the ideal momentum will undergo oscillations at synchrotron freqency described by

$$\delta = -\hat{\delta}\sin\left(\Omega t\chi_i\right), \tag{2.35}$$

where $\hat{\delta}$ is the maximum momentum deviation.

We notice that Eq. (2.32) describes the motion of a pendulum with the frequency Ω that for small amplitudes ($\sin\varphi \approx \varphi$) becomes equal to the equation of motion for a linear harmonic oscillator. For large oscillation amplitudes we cannot anymore approximate the trigonometric fuction $\sin\varphi \approx \varphi$ by its argument. We now get

$$\ddot{\varphi} = -\Omega^2\sin\varphi \tag{2.36}$$

which is identical to that of a mechanical pendulum. Particle trajectories in phase space can be derived for different values of the energy of the system. These trajectories are shown in Fig. 2.4.

The trajectories are of two types. In one type the trajectories are completly local and describe oscillations about equilibrium points separated by 2π along the abscissa. For the other type, the trajectories are not limited to a particular area in phase and the particle motion assumes the characteristics of libration. The lines separating the regime of libration from the regime of oscillation are called separatrices. Particle motion is stable inside the separatrices due to the focusing properties of the potential well. The area within the separatrices is called an RF bucket describing a place where particles are in stable motion.

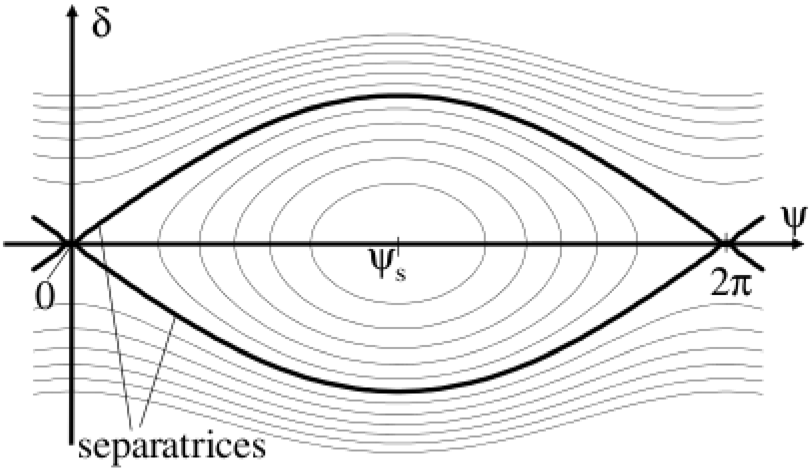

Figure 2.4: Phase space diagrams for a synchronous phase $\psi_s = \pi$ [23].

2.2.3 Wakefield Effects

When intense relativistic particle bunches travel in the vacuum chamber or the cavities of an accelerator, they generate electromagnetic fields that are modified by metalic boundaries. These "wakefields" may act back on the bunch itself or trailing bunches and perturb the motion of the particles and change their energy distribution [24].

Wakefields generally exist as damped, oscillatory elecromagnetic disturbances, which can be described equivalently as a sum of all resonant modes excited within the structure. Wakefields include the higher-order modes and the beam-excited accelerating mode, whose main effect is usually described separately as beam loading. The highest-frequency components comprising the wakefields may act on particles in the same bunch but do not remain localized, and for frequencies higher than the cutoff frequency of the pipe, propagate away along the beam pipe. The lower-frequency modes, below the cutoff frequency of the pipe, remain localized near the structures in which they were born, and may linger, depending on the time constants of the individual modes, to act on particles in trailing bunches. Radiated fields are sometimes classified as short- or long range wakefields.

Short-Range Wakefields

For ultrarelativistic bunches, short-range (longitudinal) wakefields generated by the particles at the head of the bunch affect trailing particles in the same bunch, causing energy loss, energy spread and for off-axis bunches, a transverse deflection of the particles in the tail.

The wakefields do work on the beam and cause the "parasitic energy loss". The energy can be restored by increasing the RF applied voltage. The energy lost to the wakefields per RF cell from an electron beam with N particles per bunch and for a linac section of length L and cell length l_c is

$$\Delta U(L) = \frac{(eN)^2 k_{\text{tot}} L}{l_c}, \tag{2.37}$$

where k_{tot} is the total bunch loss parameter [25]. We must note that the contributions to the wakefield from other components than RF cavities (such as vacuum tubes) are not always negligible.

Long-Range Wakefields

The most serious effect of long-range (transverse) wakefields is caused by the transverse deflecting modes that induce time-varying transverse deflections in trailing bunches. If the deflecting modes are strongly excited by the beam, they may cause a beam-breakup (BBU) instability, leading to effective emittance growth when averaged over time. Eventually the beam is lost on the walls. The long-range wakefields generally consist of a few low-frequency modes.

2.3 Undulators

An undulator is a spatially periodic magnetic structure designed to produce quasi-monochromatic synchrotron radiation from relativistic particles. The field of the undulator magnet is periodic along the beam axis, with a period length λ_u (Fig. 2.5).

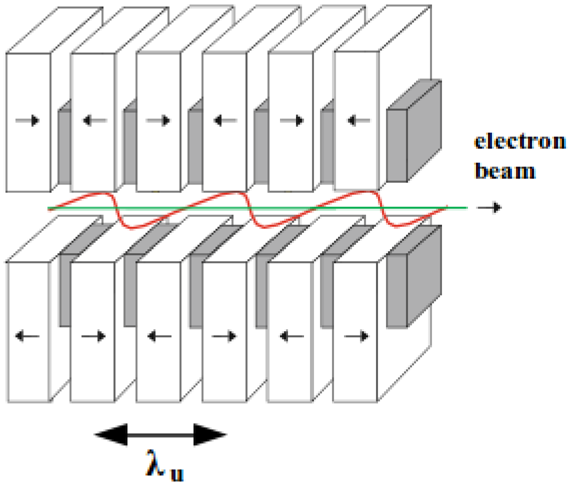

Figure 2.5: Schematic view of a planar undulator magnet with alternating polarity of the magnetic field and of the sine-like trajectory of the electrons.

2.3.1 Undulator Field

The potential of the undulator field may be written in the form

$$\varphi(s,z) = f(z)\cos\left(2\pi\frac{s}{\lambda_u}\right) = f(z)\cos(k_u s). \tag{2.38}$$

The unknown function $f(z)$ describes the vertical distribution of the field and has the solution [26]

$$f(z) = A\sinh(k_u z). \tag{2.39}$$

From this we obtain the vertical field component

$$B_z(s,z) = \frac{\partial \varphi}{\partial z} = k_u A \cosh(k_u z)\cos(k_u s). \tag{2.40}$$

To determine the constant of integration A, we must start with the flux density B_0 in the middle of the pole tip (Fig. 2.6). This point has the coordinates $(s,z) = (\lambda_u/4, g/2)$.

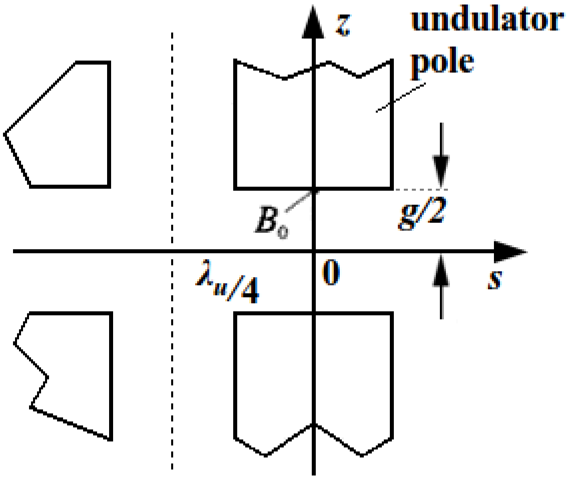

Figure 2.6: Determination of the constants of integration from the field value B_0 in the middle of poletip.

It follows from Eq. (2.40)

$$B_0 = B_z(0, \frac{g}{2}) = k_u A \cosh(k_u \frac{g}{2}) = k_u A \cosh(\pi \frac{g}{\lambda_u}) \tag{2.41}$$

and

$$A = \frac{B_0}{k_u \cosh\left(\pi \frac{g}{\lambda_u}\right)}. \tag{2.42}$$

This gives us

$$\begin{aligned} B_z(s,z) &= \frac{B_0}{\cosh\left(\pi \frac{g}{\lambda_u}\right)} \cosh(k_u z)\cos(k_u s), \\ B_s(s,z) &= \frac{B_0}{\cosh\left(\pi \frac{g}{\lambda_u}\right)} \sinh(k_u z)\sin(k_u s). \end{aligned} \tag{2.43}$$

Along the beam axis the periodically varying field thus has the peak value

$$\tilde{B} = \frac{B_0}{\cosh\left(\pi \frac{g}{\lambda_u}\right)}. \tag{2.44}$$

We are only interested in the field along the axis ($z = 0$). From Eq. (2.43) and (2.44) we write this field in the simple form

$$B_z(s) = \tilde{B}\cos(k_u s). \tag{2.45}$$

2.3.2 Equations of motion in an undulator

As it passes through the undulator magnet, the electron is acted upon by the Lorentz force, (Eq. (2.1)). We assume that the magnetic field has no B_x component, $\boldsymbol{B} = (0, B_z, B_s)$. In addition, we neglect the vertical component of the electron's velocity, $\boldsymbol{v} = (v_x, 0, v_s)$. Both approximations are adequately satisfied in most cases.

From the Lorentz force we can obtain the following set of equations describing the coupled motion in the s-x plane

$$\begin{aligned} \ddot{x} &= -\dot{s}\frac{e}{m_e\gamma}B_z(s), \\ \ddot{s} &= \dot{x}\frac{e}{m_e\gamma}B_z(s). \end{aligned} \tag{2.46}$$

The electrons travel along the s-axis through the undulator and encounter the periodic field $B_z(s)$, which induces a horizontal oscillatory motion. For relativistic electrons the velocity v_s along the s-axis dominates. Approximating $\dot{x} \ll c$, $\dot{s} = v_s = \beta c = \text{const}$, and replacing the time derivative by spatial derivative with respect to s via $\dot{x} = x'\beta c$ and $\ddot{x} = x''\beta^2 c^2$, we get the equations of motion

$$\begin{aligned} x'(s) &= \frac{\lambda_u e\tilde{B}}{2\pi m_e c\gamma}\sin(k_u s), \\ x(s) &= \frac{\lambda_u^2 e\tilde{B}}{4\pi^2 m_e c\gamma}\cos(k_u s). \end{aligned} \tag{2.47}$$

From this we get the dimensionless quantity called undulator strength

$$K = \frac{\lambda_u e\tilde{B}}{2\pi m_e c}. \tag{2.48}$$

We can write the horizontal particle motion in the form

$$x'(s) = \frac{K}{\gamma}\sin(k_u s). \tag{2.49}$$

Using $\dot{x} = x'\beta c$ and $s = \beta c t$ gives

$$\dot{x}(t) = \beta c\frac{K}{\gamma}\sin(\omega_u t), \quad \text{with} \quad \omega_u = k_u\beta c. \tag{2.50}$$

For a finite horizontal velocity $\dot{x}$, the longitudinal velocity component $\dot{s}$ is the projection onto the orbit of the arbitrary but constant particle velocity βc. This may be calculated according to $\dot{s}^2 = (\beta c)^2 - \dot{x}^2$. Using $\beta = 1 - 1/\gamma^2$ and inserting the expression for the horizontal velocity from Eq. (2.50), we can approximate the velocity projection along the beam axis to

$$\dot{s}(t) = c\left\{1 - \frac{1}{2\gamma^2}\left[1 + \frac{\beta^2K^2}{2}(1 - \cos(2\omega_u t))\right]\right\}, \tag{2.51}$$

which consist of the average velocity along the s-axis

$$\dot{s} = c\left\{1 - \frac{1}{2\gamma^2}\left[1 + \frac{\beta^2 K^2}{2}\right]\right\}, \tag{2.52}$$

and a small pertubation

$$\Delta\dot{s}(t) = \frac{c\beta^2 K^2}{4\gamma^2}\cos(2\omega_u t). \tag{2.53}$$

The average relative velocity follows from Eq. (2.52)

$$\beta^* = \frac{\dot{s}}{c} = 1 - \frac{1}{2\gamma^2}\left[1 + \frac{\beta^2 K^2}{2}\right]. \tag{2.54}$$

2.3.3 Undulator Radiation

As an electron passes through the undulator, it performs transverse oscillations as the result of the periodic magnetic field. The oscillations have a well-defined frequency, determined by the period length of the undulator. In the laboratory frame this frequency is

$$\Omega_w = \frac{2\pi\beta c}{\lambda_u} = k_u \beta c. \tag{2.55}$$

For $K \ll 1$, the modulation of the longitudinal particle velocity may be neglected and we effectively have a pure oscillation in the x direction. In a co-moving frame with average velocity β^* this frequency transforms according to

$$\omega^* = \gamma\Omega_w. \tag{2.56}$$

In this reference frame the electron emits semi-monocromatic radiation with a frequency ω^*, typical of undulators. For a sufficiently large number of periods it can be several orders of magnitude more intense than the normal synchrotron radiation.

The undulator radiation can only be observed in the laboratory frame. Hence it is necessary to transform it from the co-moving frame into the laboratory frame, using the relativistic Doppler effect. We consider a photon of momentum p, emitted in the laboratory frame at an angle Θ_0 to the s-axis. In the laboratory frame, the energy and momentum of the photon may be written in the form

$$\begin{aligned} E &= \hbar\omega, \\ p &= \frac{\hbar\omega}{c}, \end{aligned} \tag{2.57}$$

where ω is the radiation frequency. Using these expressions and transforming the photon four-momentum via a Lorentz transformation into a co-moving frame with velocity β^* and energy γ^*, we obtain the expression for the transformed photon energy with $E^* = \hbar\omega^*$

$$\frac{\hbar\omega^*}{c} = \gamma^2\frac{\hbar\omega_w}{c}\left(1 - \beta^*\cos\Theta_0\right). \tag{2.58}$$

Solving this equation with respect to ω yields the required expression for the frequency transformation through the relativistic Doppler effect and inserting the frequency ω^* from Eq. (2.56) into this transformation we obtain

$$\omega_w = \frac{\Omega_w}{1-\beta^*\cos\Theta_0} \Rightarrow \frac{\lambda_u}{\lambda_w} = \frac{1}{1-\beta^2\cos\Theta_0}, \tag{2.59}$$

where

$$\lambda_w = \lambda_u(1-\beta^*\cos\Theta_0) \tag{2.60}$$

is the wavelength of the undulator radiation in the laboratory frame. Replacing β^* by the expression in Eq. (2.54) and using the approximation $\cos\Theta_0 \approx 1-\Theta_0^2/2$, we get to the very importante coherence conditon for undulator radiation,

$$\lambda_w = \frac{\lambda_u}{2\gamma^2}\left(1-\frac{K^2}{2}+\gamma^2\Theta_0^2\right). \tag{2.61}$$

The intensity of coherent radiation from the undulator is proportional to the square of the partial wave amplitudes and it has the form of

$$I(\Delta\omega) \propto \left[\frac{\sin\left(\pi N_u \frac{\Delta\omega}{\omega_w}\right)}{\pi N_u \frac{\Delta\omega}{\omega_w}}\right], \tag{2.62}$$

which is illustrated in Fig. 2.7.

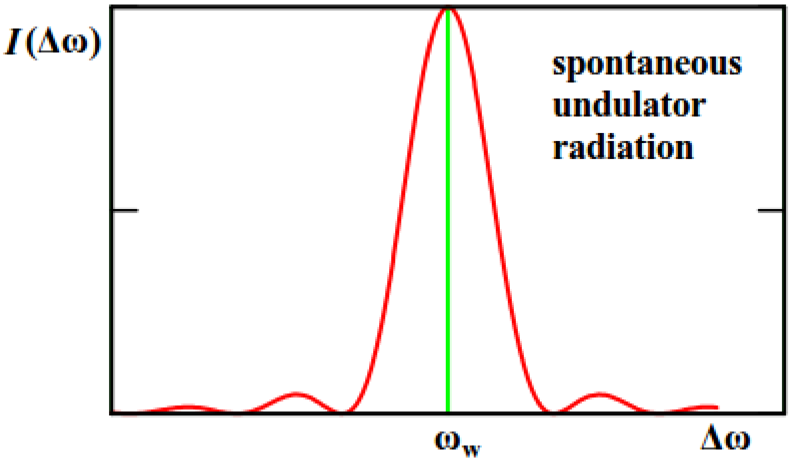

Figure 2.7: Intensity distribution of the undulator radiation.

2.4 The Free Electron Laser

In a free electron laser, electrons and laser beam must travel along the same axis in order to maximize the length of the interaction region and so allow sufficient exchange of energy per beam crossing. The laser electric field $\boldsymbol{E}_L$ and the velocity v of the electrons are then perpendicular to one another. The energy exchange in this case is zero. Direct exchange of energy between electrons and laser is thus not possible. An undulator is therefore inserted, which gives the beam a horizontal velocity component (Eq. (2.50)).

The electric field of the FEL beam can now couple to the horizontal component. A positive yield is only possible if the phase between the undulator period and the laser field satisfies certain conditions. We will introduce these by considering a single electron. We assume that at a particular point in time the electron crosses the orbit and has a transverse velocity v_x. If this time and position coincides with a maximum of the electric field E_L of the laser wave travelling alongside the beam, and this field acts in the same direction as v_x, then the negatively charged electron will be decelerated by the field and hence the energy will be transferred to the laser field.

After half and undulator period, the electron agin crosses the orbit and this time has the velocity component $-v_x$. Since the electron always moves more slowly than the electromagnetic field of the laser, and also since the bending in the undulator forces the electron to travel further, the laser field moves ahead of it. If the system is set up correctly, this phase shift will be exactly $\Delta\Psi = \pi$, and the electric field acting on the electron will now have the value $-E_L$. In this case the electron again loses energy, which is transferred to the laser field. This process is repeated every time the electron crosses the orbit, until it reaches the end of the undulator. The result is thus an overall gain in the energy by the laser field.

If $\boldsymbol{E}_L$ is the electron field of the laser wave, then the change in energy of the electrons travelling along with it is given by the general realtion

$$\Delta W = -e \int \boldsymbol{E}_L \cdot \mathrm{d}s = -e \int \boldsymbol{v} \cdot \boldsymbol{E}_L \mathrm{d}t. \tag{2.63}$$

To a good approximation, the x-component of the laser field may be regarded here as a plane wave of the form

$$E_{L,x} = E_{L,0} \cos(k_L s - \omega_L t + \varphi_0), \tag{2.64}$$

where $k_L = 2\pi/\lambda_L$ is the wavenumber, ω_L the frequency of the laser wave and φ_0 is an arbitrary initial phase. For $\beta = 1$, the horizontal component of the electron velocity is

$$v_x = c\frac{K}{\gamma} \sin(k_u s). \tag{2.65}$$

Inserting Eq. (2.64) and (2.65) into (2.63), the change in the electron energy is given by

$$\begin{aligned} \Delta W &= -\frac{ceE_{L,0}K}{\gamma} \int \cos(k_L s - \omega_L t + \varphi_0) \sin(k_u s) \mathrm{d}t \\ &= -\frac{ceE_{L,0}K}{2\gamma} \int \{ \sin\left[(k_L + k_u)s - \omega_L t + \varphi_0\right] \\ &\qquad - \sin\left[(k_L - k_u)s - \omega_L t + \varphi_0\right] \} \mathrm{d}t. \end{aligned} \tag{2.66}$$

On average, it is possible to transfer energy between the electron and the laser field if the phase

$$\Psi_\pm = (k_L \pm k_u)\bar{s} - \omega_L t + \varphi_o \tag{2.67}$$

between the electron and the electromagnetic wave of the FEL only varies very slowly with time and remains virtually constant within the undulator. Thus, the time derivative must vanish. With

$\omega_L = k_L c$ and $\dot{\bar{s}} = \beta^* c$ it follows that

$$\frac{1}{c}\frac{\mathrm{d}\Psi_\pm}{\mathrm{d}t} = (k_L \pm k_u)\beta^* - k_1 = 0. \tag{2.68}$$

Inserting the average relative velocity from Eq. (2.54) and realizing the fact that $k_u \ll k_L$, Eq. (2.68) yields

$$\begin{aligned} 0 &= (k_L \pm k_u)\left[1 - \frac{1}{2\gamma^2}\left(1 + \frac{K^2}{2}\right)\right] - k_L \\ &\approx -\frac{k_L}{2\gamma^2}\left(1 + \frac{K^2}{2}\right) \pm k_u. \end{aligned} \tag{2.69}$$

It is clear that only the solution with positive sign can exist and if we replace k_L and k_u by the corresponding wavelengths, we obtain the resonant condition from Eq. (2.61),

$$\lambda_L = \frac{\lambda_u}{2\gamma^2}\left(1 + \frac{K^2}{2}\right) \tag{2.70}$$

for a radiating angle $\Theta_0 = 0$. In Eq. (2.66), only the phase $\Psi_+ = (k_L + k_u)\bar{s} - \omega_L t + \varphi_0 \approx$ const. contributes to the energy exchange, while the term with the phase $\Psi_- = (k_L - k_u)\bar{s} - \omega_L t + \varphi_0 \approx$ const. oscillates rapidly and so on average has no effect on the total transferred energy. The angle Θ_0 does not appear in the Eq. (2.70) because we have only considered the problem in one dimension. Transverse effects, such as the sizes of the electron and laser beams and overlapping of the two beams, are neglected here.

2.4.1 Equations of motion for electrons in the FEL

Electrons with $\gamma = E/m_e c^2$ interact with the electromagnetic field of the FEL and undergo a change $\Delta\gamma$ and a phase shift $\Delta\Psi$ relative to the laser field. The functions $\Delta\gamma(s)$ and $\Delta\Psi(s)$ within the undulator give a complete description of the particle motion through the FEL. The relative change in energy per path element $\mathrm{d}s = c\mathrm{d}t$ for the Nth harmonic is

$$\begin{aligned} \left(\frac{\mathrm{d}\gamma}{\mathrm{d}s}\right) = \frac{k_u K_L K}{2\gamma}\left[J_{\frac{N-1}{2}}(N\eta) - J_{\frac{N+1}{2}}(N\eta)\right] \times \sin\left[(k_L + Nk_u)\bar{s} - \omega_L t + \varphi_0\right] \\ \text{with}\ \ N = 1, 3, 5, \cdots, \end{aligned} \tag{2.71}$$

where $K_L = eE_{L,0}/(k_u m_e c^2)$ is the dimensionless laser field parameter, $\eta = k_L K^2/(8N\gamma^2 k_u)$ and $J_n(x)$ is the nth-order Bessel function.

In order to describe the complete motion of electrons in the FEL, we also need to know the change in the phase per path element. To achieve a non-zero overall energy transfer over the path through the undulator, the phase

$$\Psi = (k_L + Nk_u)\bar{s} - \omega_L t + \varphi_0 \tag{2.72}$$

between the Nth harmonic of the electron oscillation and the laser wave must be constant over time. Inserting Eq. (2.54) we have the condition

$$\frac{\mathrm{d}\Psi}{\mathrm{d}t} = \frac{1}{c}\frac{\mathrm{d}\Psi}{\mathrm{d}t} = Nk_u - \frac{k_L}{2\gamma^2}\left(1+\frac{K^2}{2}\right). \tag{2.73}$$

The resonance energy is defined as the energy at wich there is no phase shift relative to the laser field, i.e. $\mathrm{d}\Psi/\mathrm{d}s = 0$. Using this condition we may calculate the resonance energy

$$\gamma_r^2 = \frac{k_L}{2Nk_u}\left(1+\frac{K^2}{2}\right) \tag{2.74}$$

and can express the change in phase per path element as

$$\frac{\mathrm{d}\Psi}{\mathrm{d}s} = Nk_u\left(1-\frac{\gamma_r^2}{\gamma^2}\right). \tag{2.75}$$

The FEL is always operated at electron energies very close to the resonance energy. It is useful to use the difference $\Delta\gamma$ from the resonance energy as an energy variable

$$\gamma = \gamma_r + \Delta\gamma \quad (\Delta\gamma \ll \gamma_r). \tag{2.76}$$

Under this condition we have

$$1-\frac{\gamma_r^2}{\gamma^2} \approx 2\frac{\Delta\gamma}{\gamma_r} \tag{2.77}$$

and from Eq. (2.75) we obtain

$$\frac{\mathrm{d}\Psi(s)}{\mathrm{d}s} = 2\frac{Nk_u}{\gamma_r}\Delta\gamma(s). \tag{2.78}$$

We can write Eq. (2.71) as

$$\frac{\mathrm{d}\Delta\gamma(s)}{\mathrm{d}s} = -\frac{k_u K_L K}{2\gamma_r}\sqrt{F(N\eta)}\sin\Psi(s), \tag{2.79}$$

with

$$F(N\eta) = \left[J_{\frac{N-1}{2}}(N\eta) - J_{\frac{N+1}{2}}(N\eta)\right]^2. \tag{2.80}$$

Differentiating Eq. (2.78) with respect to s and inserting it into Eq. (2.79) leads to the general equation of a pendulum

$$\Psi''(s) + \Omega_L^2\sin\Psi(s) = 0 \tag{2.81}$$

with

$$\Omega_L^2 = \frac{Nk_u^2 K_L K}{\gamma_r^2}\sqrt{F(N\eta)}. \tag{2.82}$$

The length of an oscillation along the s-axis is $L_s = 2\pi/\Omega_L$ and $f_L = c/L_L$ is the frequency with which the electron oscillates in the potential of the laser field. This corresponds to the synchrotron frequency. We can depict the electron motion in a Ψ-$\Delta\gamma$ diagram as shown in Fig. 2.8. At small amplitudes and with strong laser fields, the electron performs stable oscillations, which to a good approximation, would be represented by an ellipse in this diagram. As the amplitude increases, the frequency decreases and reaches zero in the limiting case $\Psi_{\max} \to \pi$ for $\Delta\gamma = 0$.

This represents the limit between stable particle oscillation and the unstable region in which the particles can no longer be contained within the potential of the laser field.

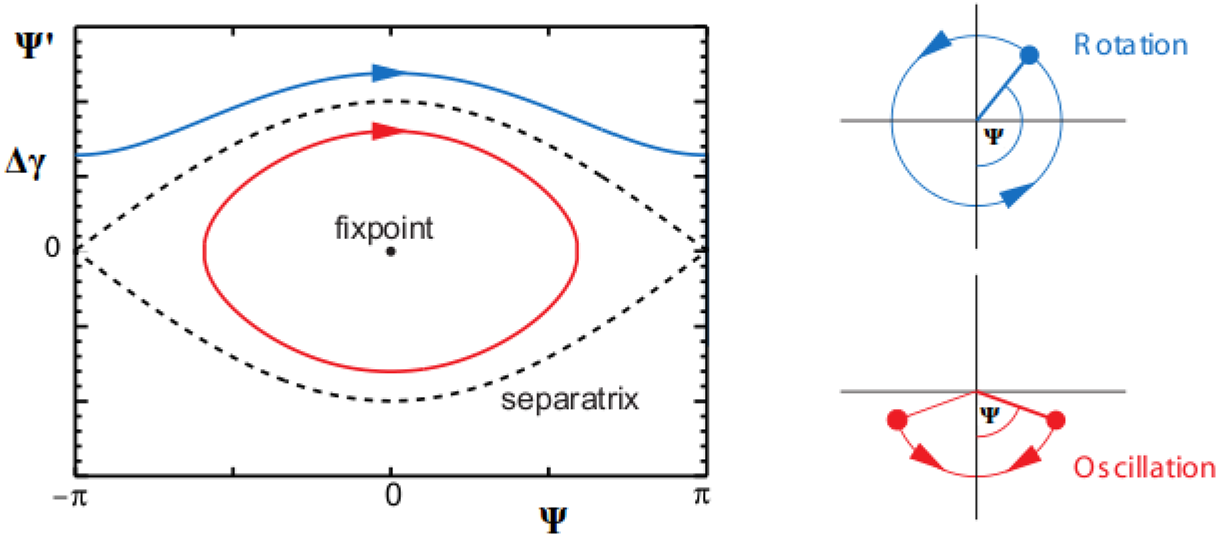

Figure 2.8: Electron motion in the FEL field. The phase shift relative to the laser wave is ploted along the horizontal axis, and the energy difference from the resonance energy is plotted vertically. Two different types of electron motion are plotted and may be visualized in terms of corresponding pendulum motion.

At the resonance energy, $\gamma = \gamma_r$, the curve passes through zero, i.e. there is no amplification. Hence it is important to tune the electron energy to be slightly higher than that required by the resonance condition. If $\Delta < 0$, the electron beam gains energy at the expense of the laser field and the particles are accelerated.

2.4.2 Amplification of the FEL in the low gain regime

The energy stored in the laser field is

$$W_L = \frac{\varepsilon_0}{2} E_{L,0}^2 V, \tag{2.83}$$

where V is the volume occupied by the laser field. The amplification of the FEL due to a single electron is defined as [27]

$$G_1 = \frac{\Delta W_L}{W_L} = -\frac{2 m_e N K_u K^2}{\varepsilon_0 V m_e c^2 \gamma_r^3} F(N\eta) \frac{\Delta \Psi'}{\Omega_L^4}. \tag{2.84}$$

Here

$$\Delta\Psi' = \Psi'_{\text{end}} - \Psi'_{\text{start}} \tag{2.85}$$

is the difference in ψ' that the electron udergoes from the beginning of the undulator Ψ'_{start} to the end Ψ'_{end}.

We need to sum the amplification induced by each electron in a bunch and average all initial phases of the electrons relative to the laser wave as they enter the undulator. This gives the total amplification of the FEL

$$G = -\frac{2m_e N K_u K^2}{\varepsilon_0 V m_e c^2}\frac{n_b}{\gamma_r^3}F(N\eta)\frac{\langle\Delta\Psi'\rangle}{\Omega_L^4} \tag{2.86}$$

for an electron density $n_b = n/V$ in a bunch and with

$$\langle\Delta\Psi'\rangle = \frac{1}{n}\sum_{i=1}^{n}\Delta\Psi'_i. \tag{2.87}$$

The amplification function strongly depends on the injection energy of the electrons. Plotting G as a function of the injection energy $\Delta\gamma$ results in a curve, shown in Fig. 2.9, which is typical of an FEL.

For relatively weak laser fields $E_{L,0}$ the field parameter K_L and the frequency Ω_L are very small. The amplification due to each electron passing through the undulator is also small. Thus the intensity of the laser field only changes slightly and may be assumed to be constant during each pass. This is the so-called low-gain regime of the FEL. Here the laser field is so weak that virtually all the electrons lie outside the separatrix and do not perform stable oscillations in the laser field.

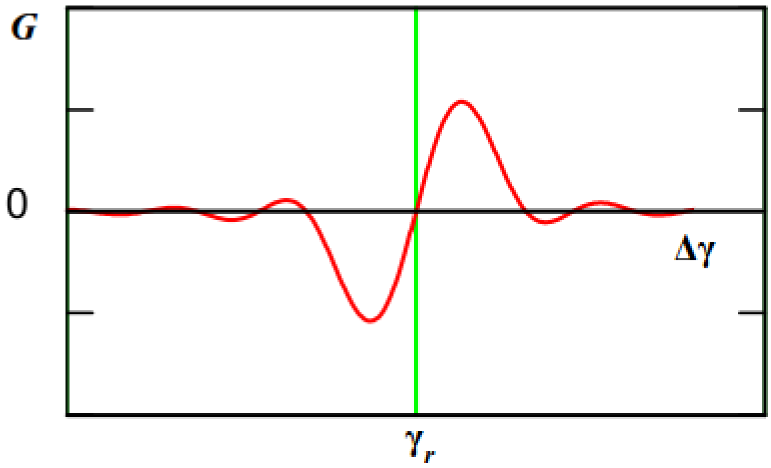

Figure 2.9: Amplification or gain curve of the FEL [28].

2.4.3 FEL amplification in the high gain regime

For very strong FEL fields the separatrix is very broad along the direction of the energy axis. A relatively large number of electrons lie inside the separatrix and perform stable pendulum-like oscillations. In the presence of very strong amplification, we talk of a high-gain regime. The laser field can no longer be assumed to be constant inside the undulator and we must take into account the evolution of the electromagnetic wave. The frequency Ω_L of the electron motion in the FEL field is very high in this regime. Here we must take into account the fact that the particles in the electron beam are approximately evenly distributed along the length of the bunch. We assume that the incoming particles all have the same energy γ_{start}, so they form a horizontal line in the Ψ-$\Delta\gamma$ plane (Fig. 2.10). The electron beam with n particles has the initial energy

$$E_{\text{start}} = n\gamma_{\text{start}} m_e c^2 = n(\gamma_r + \Delta\gamma_{\text{start}}) m_e c^2. \tag{2.88}$$

with $\gamma_{\text{start}} = \gamma_r + \Delta\gamma$. Since we assumed that the electrons are uniformly distributed, we can take each small phase volume containing an electron and associate it with a particular phase, i.e. the ith electron has the initial phase $\Psi_{\text{start},i}$. The relative initial energy, denoted $\Delta\gamma_{\text{start},i}$ is the same for all electrons.

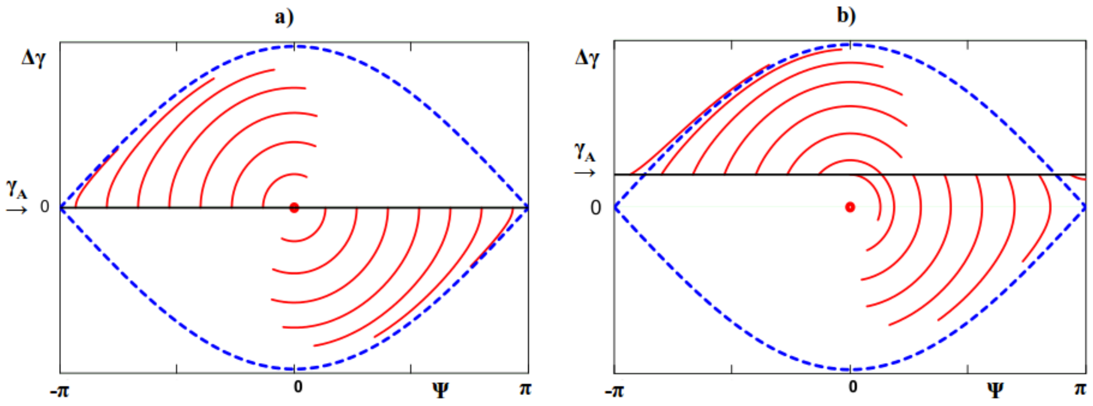

Figure 2.10: Motion of electrons with a flat phase distribution as they pass through the FEL. a) shows the motion when $\gamma_{\text{start}} = \gamma_r$ and b) the motion when $\gamma_{\text{start}} > \gamma_r$ [29].

We take the large number of electrons lying close together in the phase space and combine them into a single macro-particle and then calculate the FEL amplification using a relatively small number of such particles. The final energy of the total assembly of electrons (or macro-particles) as they leave the undulator is

$$E_{\text{end}} = m_e c^2 \sum_{i=1}^{N} (\gamma_r + \Delta\gamma_{\text{end},i}) = E_{\text{start}} + m_e c^2 \sum_{i=1}^{N} \Delta\gamma_{\text{end},i}. \tag{2.89}$$

If we start at the resonance energy ($\Delta\gamma = 0$) it is clear from Fig. 2.10a than for every electron with an initial phase $+\Psi$ there is another with the phase $-\Psi$, which by symmetry will exactly compensate for it in the energy sum. In this situation the total change of energy of the laser field is zero and there is no FEL amplification. This is the same result as in the low-gain regime. This situation changes if the particles are injected at an energy γ_{start} which is higher than the resonance energy. Than the average energy of the outgoing electrons at the end of the undulator is lower than the injected energy, as shown in Fig. 2.10b. The laser field gains energy.

2.4.4 Bunching

When an electron beam starts to interact with an electromagnetic wave, all the particles are randomly distributed in phase with respect to the wave, as shown in Fig. 2.11a. During the interaction, the electrons absorb or loose energy, depending on their phase with respect to the wave (Fig. 2.11b). As the resonance condition is satisfied, half of the particles absorb energy from the electromagnetic wave and the other half transfer energy to the wave. Therefore the net amplification is zero.

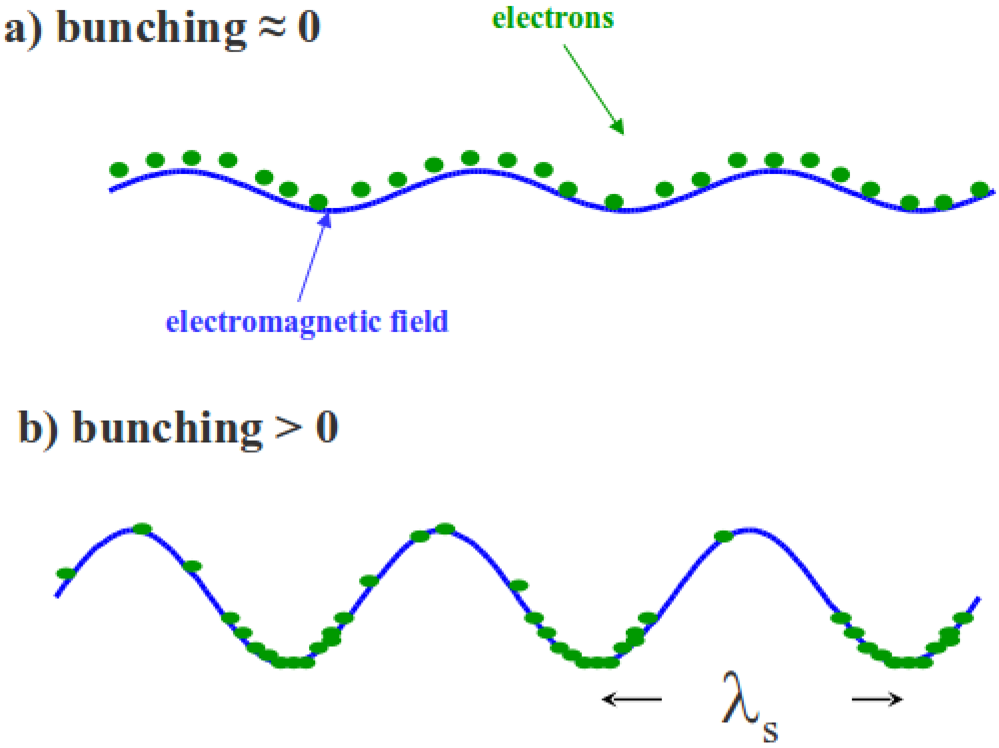

Figure 2.11: Bunching evolution. a) Electrons are randomly distributed in phase (initial condition). b) Electrons start bunching in a λ_s scale and the wave is eventually amplified.

The interaction with the ponderomotive wave (radiation+undulator field) induces a modulation of the electron energy. This energy modulation evolves in spatial modulation, also called bunching. The parameter that regulates the bunching and hence the amplification is called bunching factor and is defined as

$$b = \langle \exp[-i\theta] \rangle, \tag{2.90}$$

where θ is the phase of the electron with respect to the ponderomotive wave.

Fig. 6.10 explains the bunching mechanism, as it occurs in the electron phase space (γ,θ). When electrons exceed the wave of a phase equal to a quarter of the ponderomotrice force period there is maximum gain. Here the process reaches the saturation because the electrons are not able to transfer their energy to the wave anymore. Inside of an electron bunch particles are grouped into "microbunches", separated (approximately) by one wavelength of the laser. The resulting strong radiation field enhances the microbunching even further and leads to an exponential growth of the radiation power. As the beam proceeds further inside the undulator, the spatial modulation arises also where the ponderomotive force is positive and this causes "overbunching".

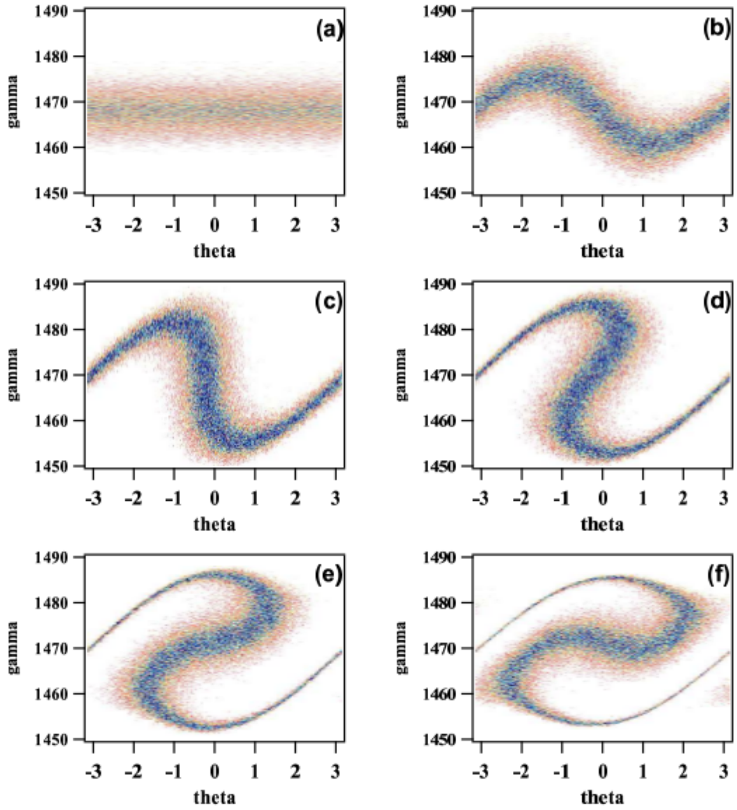

Figure 2.12: Evolution of the electron-beam phase space of one wavlength of the seed laser. a) initial distribution, b) energy modulation c) spatial modulation (bunching) d) slightly overbunching e-f) overbunching [30].

2.4.5 Harmonic Generation

In the single pass case, the usual configuration for harmonic generation (HG) relies on the seeding technique (i.e., the use of an external laser) and makes use of two undulators: the first undulator is tuned to the same wavelength as the external laser and the second one is tuned to the selected harmonic. Between the two undulators there is a dispersive section, which has the role to help the conversion of the energy modulation into bunching. A schematic picture of the scheme under investigation is shown in Fig. 2.13.

In the first undulator the interaction between the seed laser and the electron beam produces a modulation in the energy distribution of electrons at the wavelength of the external laser. At the beginning (Fig. 2.14a), the electron-beam energy distribution has a random phase with respect to the electromagnetic field provided by the seed laser and is characterized by an initial (incoherent) energy spread. During the interaction with the seed, some electrons lose and some electrons gain kinetic energy. As a consequence, the energy distribution is clearly modified, as shown in Fig. 2.14b. The magnetic field of the dispersive section forces the electrons with different energies to follow different paths. Therefore, the passage through the dispersive section converts the energy modulation in spatial bunching. The corresponding phase space is shown in Fig. 2.14c. Finally, in the second undulator which is tuned to one of the harmonics of the seed laser, the electrons

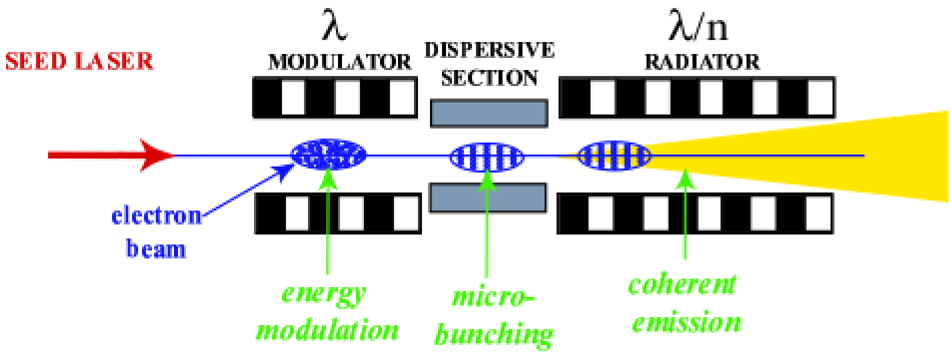

Figure 2.13: Seeded Harmonic Generation scheme.

produce coherent light since each "micro-bunch" emits radiation as a macro-particle.

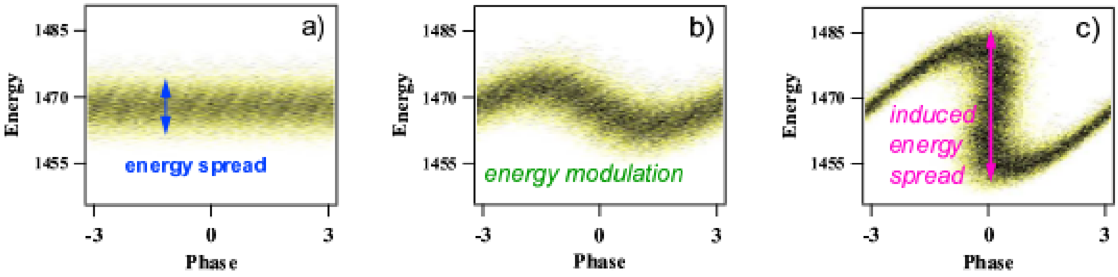

Figure 2.14: Evolution of the bunching in an electron bunch.

If the electron beam is flat in current and energy, i.e. no quadratic (or higher order) chirp in the two energy distributions, the spectrum of the extracted radiation is expected to be close to the Fourier transform limit. As the electron beam has a pulsed structure, the seed pulse has to be synchronized with the electron bunch. The pulse duration at the exit of the radiator is determined by the duration of the seed pulse.

Dispersive Section

An ideal dispersive section can be represented as a 3-pole magnet with total length L_d. The form of the magnetic field is such that at the end of the dispersive section the electrons do not have any transverse or angular displacement with respect to the entrance. This magnetic field induces different paths for particles having different energies. As a consequence, energy separation, $\Delta\gamma$, is transformed in the time separation, Δt [31]:

$$\Delta t = \frac{\mathrm{d}t}{\mathrm{d}\gamma}\Delta\gamma. \tag{2.91}$$

To describe the process one can also make use of the electron phase instead of time. At the end of the first undulator ($z = z_1$) the phase of the jth particle is

$$\theta_j = (k_{s1} + k_{u1})z_1 - \omega_{s1} t_{j1}, \tag{2.92}$$

where t_{j1} is the time of arrival at the end of the first undulator, $k_{s1} = 2\pi/\lambda_{s1} = \omega_{s1}/c$ is the wave number relative to the fundamental wavelength in the first undulator and $k_{u1} = 2\pi/\lambda_{u1}$ is the wave number relative to the first undulator (λ_{u1} is the period of the first undulator). At the entrance of the second undulator ($z = z_2$) the phase is

$$\psi_j = (k_{s2} + k_{u2})z_2 - \omega_{s2} t_{j2}, \tag{2.93}$$

where $k_{s2} = 2\pi/\lambda_{s2} = \omega_{s2}/c$ is the wave number relative to the fundamental wavelength in the second undulator and $k_{u2} = 2\pi/\lambda_{u2}$ is the wave number relative to the first undulator (λ_{u2} is the period of the first undulator). The arrival time at the entrace of the second undulator is given by

$$t_{j2} = t_{j1} + \frac{\mathrm{d}t}{\mathrm{d}\gamma}(\gamma_j - \gamma_0) + t_0, \tag{2.94}$$

where t_0 is a constant depending on the position of the second undulator. The phase-energy relation at the entrance of the second undulator is

$$\psi_j = \frac{\omega_{s2}}{\omega_{s1}}\left[\theta_j + \frac{\mathrm{d}\theta}{\mathrm{d}\gamma}(\gamma_j - \gamma_0) + \theta_0\right]. \tag{2.95}$$

The term $\mathrm{d}\theta/\mathrm{d}\gamma$ represents the dispersion section strength and it can be also written as

$$\frac{\mathrm{d}\theta}{\mathrm{d}\gamma} = 2k_u \frac{\Delta\gamma}{\gamma} z = \frac{2\pi}{\lambda\gamma_0}\mathrm{R56}, \tag{2.96}$$

being R56 the dispersive section strength.

Chapter 3

The FERMI Facility

3.1 Introduction

The FERMI project at the ELETTRA Laboratory of Sincrotrone Trieste (ST) [32] is a user facility for the scientific investigations with high brilliance X-ray pulses of ultra-fast and ultra-high resolution processes in material science and physical biosciences. The full FERMI facility, shown in Fig. 3.1, consists of a linear accelerator, an undulator hall with two principal Free Electron Lasers lines and an experimental hall in the complex environment of a multi-beamline user facility provided by the ELETTRA synchrotron light source.

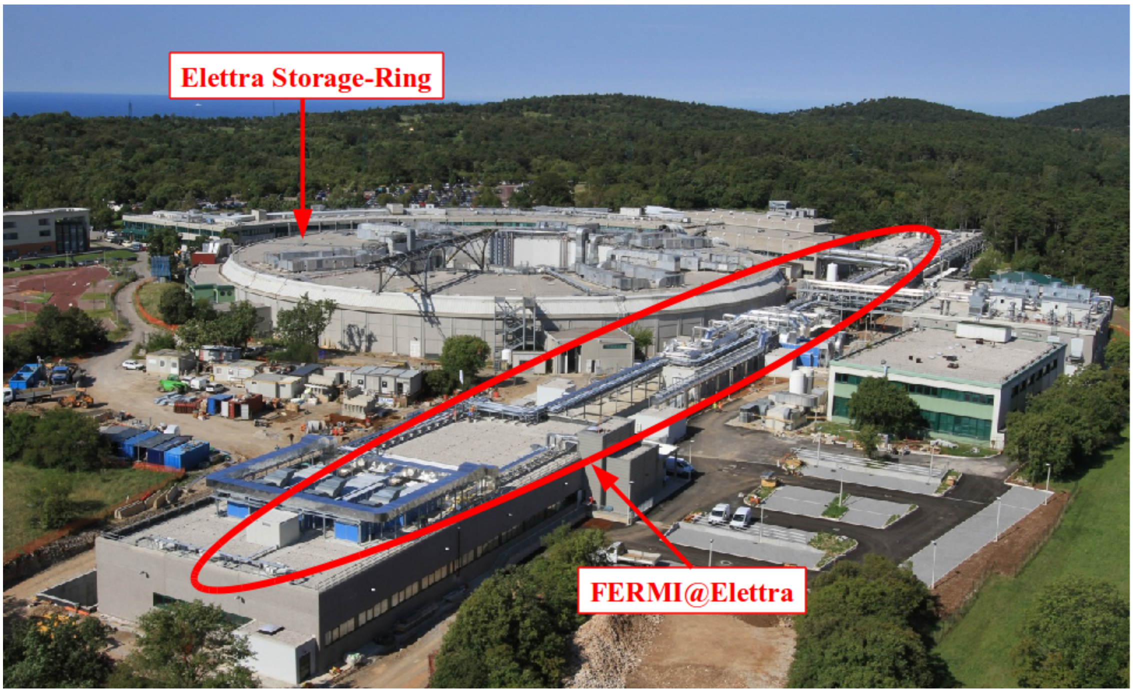

Figure 3.1: A view of the FERMI facility.

The FERMI project utilizes a linear accelerator, part of which was the injector of the ELETTRA storage ring, and a new electron source based on photoinjector technology. The addition of seven accelerating sections brings the linac energy to $\sim$ 1.2 GeV. At this energy, and with state-of-the-art undulator technology, the FEL can operate in the 100-20 nm energy region in the initial phase (FEL-1) and down to 10-4 nm in a subsequent phase (FEL-2). This chapter gives a broad overview of the facility and of the issues relevant to achieving the design objectives.

3.2 Principle of Operation

The FERMI project is based on the principle of high gain, harmonic generation FEL amplifier employing multiple undulators, up-shifting an initial “seed” signal in a single-pass [33, 34, 35]. The initial (master oscillator or seed) signal is provided by a conventional pulsed laser operating at wavelengths in the region of 240-300 nm. The energy modulation induced by the interaction of the laser with the electron beam in the first undulator (called modulator) is converted into spatial modulation after the electron beam passes through a magnetic dispersive section. The bunching further increases the initial bunch modulation at harmonics of the seed wavelength. Thus re-bunched, the electrons emit coherent radiation in a second undulator (called radiator) tuned at a higher harmonic corresponding to the desired fundamental FEL output. This scheme broadly describes the FEL-1 layout, down to 20 nm. To reach the shortest design wavelength of 4 nm, a second stage (modulator + dispersive section + radiator) is added to produce the FEL-2 configuration. As the seed laser determines the duration, bandwidth, and wavelength of the output radiation, all are tunable and controllable, covering a wide spectral range. The choice of design parameters, in fact, allows FERMI to generate FEL radiation with a wide range of characteristics tailored to match a diversity of experimental requirements, ranging from single shot, short ($\sim$100 fs), high brilliance, time-resolved experiments to ultra-fast pump-probe experiments, to high resolution ($1-5$ meV) experiments with close to transform-limited radiation on the ps time scale. The seed laser furthermore provides a reference signal throughout the FERMI facility (including the experimental beamlines) to facilitate the femtosecond level precision timing and synchronization of all systems. Delivering such flexibility to serve a broad range of potential applications imposes severe requirements on the quality of the electron beam. To meet these requirements, the FERMI FEL design is based on extensive studies of possible perturbations that may affect the electron beam dynamics, of means to correct them, and of parameter optimization. These studies show that the most important determinants of the quality of the FEL radiation are the quality and uniformity of the electron beam properties along the bunch (energy, energy spread, transverse emittance, electron optics, peak current, etc.), as well as the pulse-to-pulse stability of such properties.

Table 3.1: Nominal electron beam and FEL parameters.

Parameters	**FEL-1**	**FEL-2**	**Units**
Electron beam energy	1.2	1.5	GeV
Peak current	800	800	A
Bunch duration (FWHM)	700	1400	fs
Repetition rate	10	50	Hz
FEL peak power	1/5	0.5/1	GW
Bandwidth	$\sim$ 20	5	meV

Table 3.1 lists some of the basic parameters of the electron beam and the FEL radiation at FEL-1 and FEL-2 [36].

3.3 General Layout

A general layout of the facility is shown in Fig. 3.2.

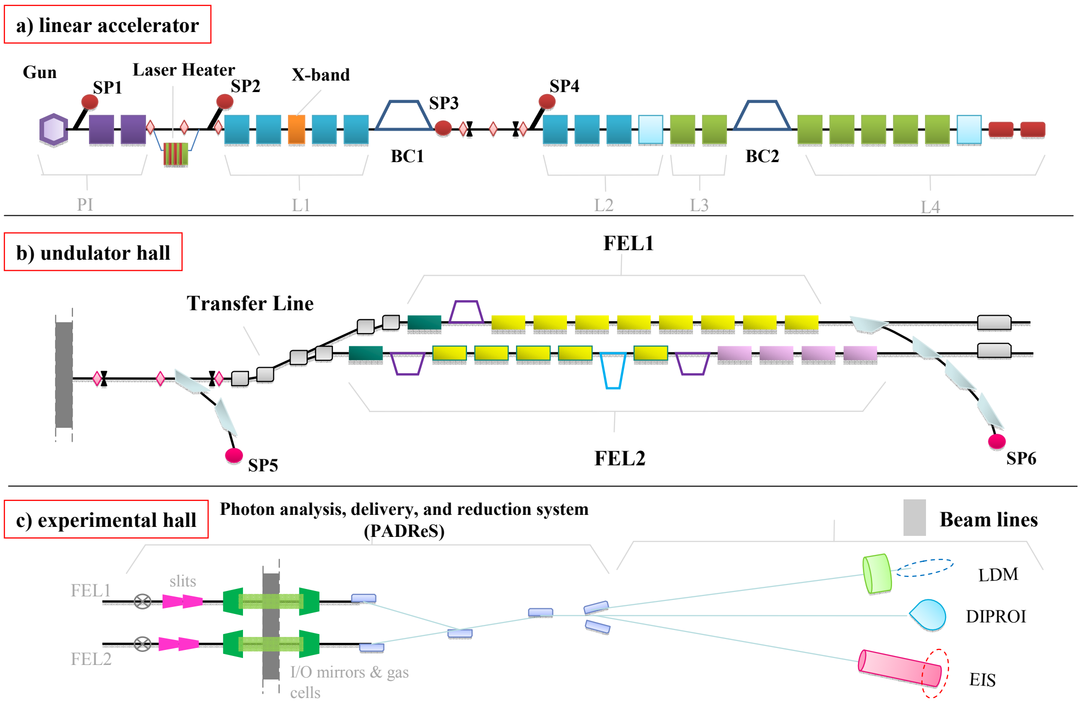
a) linear accelerator
Gun
SP1
Laser Heater
SP2
X-band
SP3
SP4
BC1
BC2
PI
L1
L2
L3
L4
b) undulator hall
FEL1
Transfer Line
SP5
FEL2
SP6
c) experimental hall
Photon analysis, delivery, and reduction system (PADReS)
Beam lines
FEL1
slits
FEL2
I/O mirrors & gas cells
LDM
DIPROI
EIS

Figure 3.2: FERMI@Elettra machine layout, including a) the linear accelerator, b) the undulator hall and c) the experimental hall. The SP1 to SP6 points are location of the electron beam spectrometer lines for beam dump and diagnostics.

The accelerator and FEL complex comprise the following parts:

- A photoinjector and two short linac sections, generating a bright electron beam and accelerating it to $\sim$ 100 MeV.
- The main linear accelerator, where the electron beam is time-compressed and accelerated to $\sim$ 1.2 GeV.
- The electron beam transport system to the undulators.
- The undulators complex, in which the FEL radiation is generated.

- The photon beam transport lines from the undulator to the experimental area.
- The experimental area.

While only two lines (FEL-1 and 2) are envisaged initially, the transverse dimension of the Undulator Area allows installation of up to four undulators side-by-side. An experimental hall will house the FEL radiation beamline optics and the experimental hutches. The following sections offer a brief overview of each major component.

3.4 The Photoinjector

The photoinjector (shown in Fig. 3.3) is based on the proven 1.6 cell electron gun developed at BNL/SLAC/UCLA [37]. The beam tracking optimization studies performed in the past years [38] called for a 800 pC, 11 ps bunch at the gun exit, with a rms normalized transverse emittance of 1.2 mm mrad at 100 MeV [39]. The repetition rate is 10 Hz during the initial stage of operation, but the design allows for upgrading the photoinjector and the main linac to 50 Hz. Following standard layout schemes, the design includes a solenoid for emittance compensation and acceleration to 100 MeV with two S-band RF sections. These sections are part of the present ELETTRA injection system. A laser pulse provides temporal and spatial bunch shaping. The FERMI design calls for a novel temporal bunch profile in which the bunch current increases approximately linearly with time (linear ramp). Such profile at the start of acceleration produces a more uniform energy and current profile at the entrance to the undulators [40].

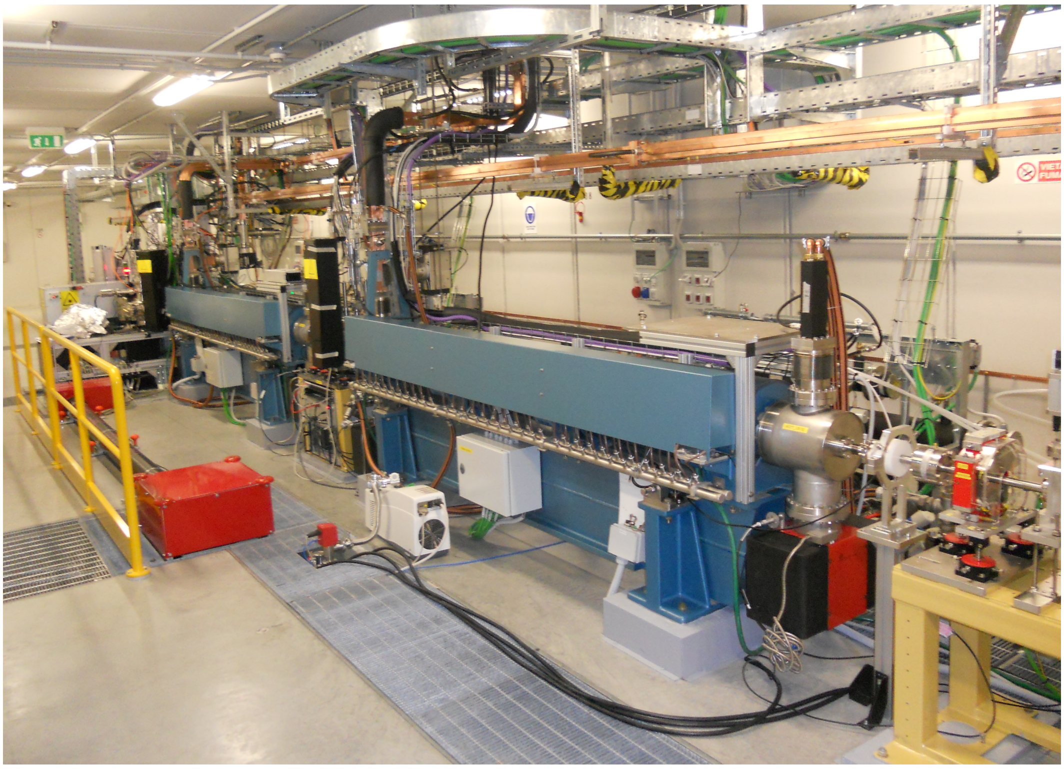

Figure 3.3: The photoinjecor at FERMI.

The front-end injection system of the FERMI linac is designed to produce the high brightness electron beam that determines the FEL performance and the quality of FEL beams delivered to the users. The electron source and the injection system are specifically designed to minimize technical risk and cost by utilizing existing accelerator components and by leveraging on the technical designs of other, contemporary X-ray FEL projects. The major injector components are shown in Fig. 3.4.

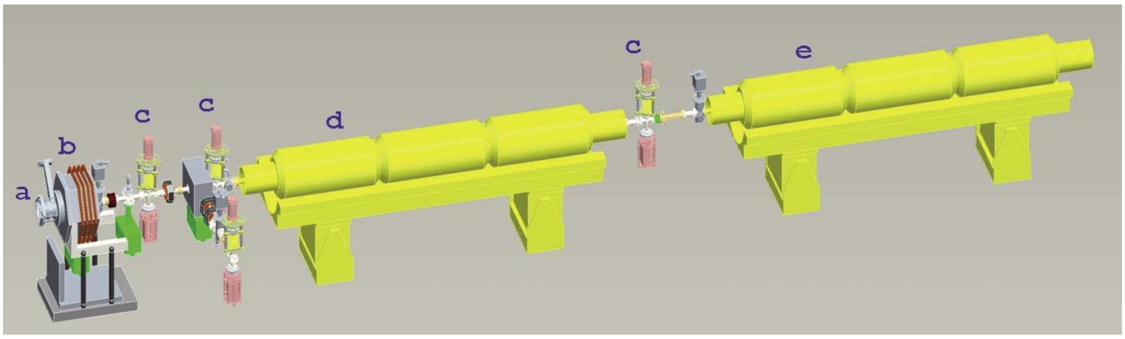

Figure 3.4: The FERMI@Elettra FEL photoinjector. a) RF Gun, b) Solenoid, c) Pop-in screens, d), e) booster accelerating sections.

3.4.1 Electron Source and RF Gun

The FERMI electron source is a metallic photocathode (polycrystalline copper) illuminated by an intense, 263 nm wavelength UV laser whose pulse shape is chosen to optimize the final beam quality. Because the best measured values of the quantum efficiency of copper at 263 nm are in the range $10^{-5} - 10^{-4}$, the laser must deliver ∼500 μJ on the cathode in order to produce a ∼1 nC bunch charge. The photocathode also serves as the conducting back plane of a one and a half cell RF gun. A first stage gun is designed for a pulse repetition rate of up to 10 Hz. An upgraded version, not described here, reaching up to 50 Hz repetition rate, is foreseen as a second stage.

External solenoid magnets are integral to the RF gun operation. A multiple pancake, emittance compensating solenoid provides focusing to help transport the beam from the gun exit to the entrance of the booster linac structures.

3.4.2 Photocathode and Drive Laser Systems

The photoinjector system for FERMI requires a robust, pulsed UV laser system. This laser provides temporal and spatial shaping of the electron bunch. The system requirements for the photoinjector laser are presented in Table 3.2 [41].

Table 3.2: Temporal specifications for the UV laser pulse.

Wavelength	<270 nm
Required pulse energy at the cathode (Cu)	∼0.5 mJ
Pulse duration range (FWHM)	1-20 ps
Pulse repetition rate (rms)	10-50 Hz

3.5 Accelerator

Since the RF photocathode gun produces 0.8 nC distributed over bunch length of 11 ps, the bunch has to be compressed by a total factor of about 11 before it enters the undulator. The two bunch compressors consist of symmetric magnetic chicanes, each 8.0 m long. They include trim quadrupoles for a fine tuning of the dispersion bump. The locations and compression factor of the two chicanes were fixed in order to minimize the 6-dimensional emittance dilution of the electron bunch in presence of space charge forces and wakefields. The electron energy at BC1 is $\sim$330 MeV in order to avoid space charge effects, while compressing the bunch early enough in the linac to reduce the effects of transverse wake fields. The energy of the second compressor is about 670 MeV, which balances the conflicting requirements of minimizing the transverse and longitudinal emittance dilution by coherent synchrotron radiation (CSR) and that of canceling the final correlated energy spread by means of the downstream longitudinal wake field.

Since the whole beam delivery system acts like a huge amplifier of energy and density modulations, a "laser heater" [42] is foreseen at 100 MeV just after the photoinjector. The uncorrelated energy spread induced by this tool is able to suppress the modulation in the energy and density distributions at a scale small with respect to the bunch length. At the same time, it is important for the FEL process to provide slice energy spread not much larger than 150 keV (rms value). Simulations have been made which calculate the emittance dilution in the linac due to transverse wakefields and anomalous momentum dispersion, each of which arises with component misalignments. These simulations include realistic correction techniques and successfully demonstrate that the required level of transverse emittance preservation is achievable.

The beam delivery system ends with a transfer line located between the end of the linac and the entrance of the FEL. This part includes the emittance diagnostic section, the electron beam switchyard for the two FELs, called Spreader, and a matching sections. The design meets the constrains imposed by the existing and planned building boundaries, by the desire to utilize existing equipment and by the demands for various diagnostic instruments.

3.5.1 Overview of Design Specifications

The FERMI accelerator hall is shown in Fig. 3.5. It consists of four linacs, L1 - L4, two bunch compressors (BC1 and BC2), a laser heater and a Spreader. The latter switches the electron beam into one of the undulator lines. The photoinjector is the first component of the accelerator. At its output the energy of the electron beam is $\sim$100 MeV and the peak current is 60-70 A. At the end of acceleration the electron beam energy is approximately 1.2 GeV and the electron peak current is 800 A.

The list of the beam specifications is shown in Table 3.3 [43]. The FERMI linear accelerator (Fig. 3.2a) operates at energy of $\sim$1.2 GeV. A challenging aspect was the demand to produce an electron beam with as uniform as possible peak current and energy distributions along the bunch. For this reason, a new parameter, the "flatness", defines the value of the quadratic component of energy variation along the bunch for which the increase in bandwidth of the X-ray signal due to this variation becomes equal to the Fourier transform limited bandwidth defined by the bunch length.

Figure 3.5: The accelerator hall.

Table 3.3: Main electron beam specifications.

	Electron Beam	Units
Bunch Charge	0.80	nC
Bunch Length (FWHM)	700	fs
Peak Current	800	A
Flatness	< 0.6	MeV/ps^2

3.5.2 Bunch Compressor

The electron bunch is compressed in order to increase the peak current. Compression is achieved by introducing an energy-position correlation along the bunch length using an RF section, followed by a dispersive beamline with an energy dependent path length: in this way, the tail of the bunch can be made to follow a shorter path than the head, and the bunch becomes shorter. The first stage of bunch compression is to introduce a longitudinally correlated energy spread in the bunch; this is accomplished by injecting the bunch into an accelerating section at a phase close to the zero-crossing of the RF waveform. The bunch is then compressed by transporting it through a dispersive section (magnetic chicanes), which provides the necessary path length dependence on energy.

A schematic of the bunch compressor with the foreseen diagnostics is shown in Fig. 3.6. It consists of a chicane built from four rectangular bending magnets (DIP1-4) [44]. Because of its symmetry, this bunch compressor is a perfect achromat. Nevertheless, leakage of the dispersion function after the last bend may occur due to errors; for this reason, trim quadrupoles are added for a fine tuning of the dispersion function. The conceptual scheme is the same for BC1 and BC2, but some components are adapted to the different bunch parameters. At the moment only the first bunch compressor is installed.

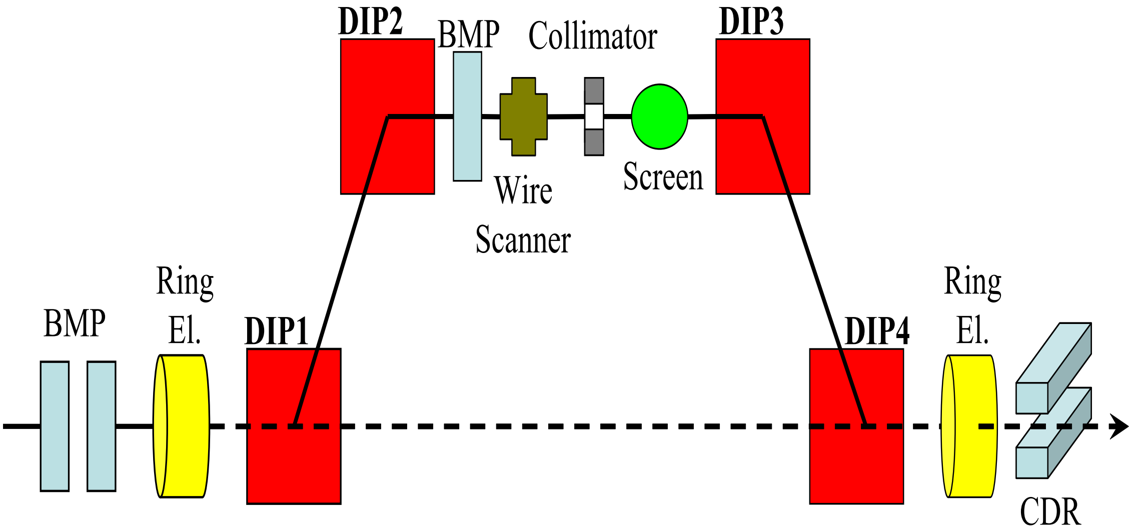

Figure 3.6: Bunch compressor diagnostics layout.

3.6 Undulators

FEL-1 consists of seven undulator magnets (1 modulator, 6 radiators), located in the undulator hall, Fig. 3.7. For FEL-2, they will make use of ten undulators. The magnetic length of induvidual undulators for FEL-1 is 2.34 m. Between the modulator and the first radiator there is a dispersive section (DS). The dispersive section is a three-pole electro-magnet allowing continuous variation of the magnet strength parameter (also denoted as R56) in order to optimize the micro-bunching of the electron beam. The DS strength depends on the length and magnetic field strength.

Due to the requirement that the output radiation polarization be continuously tunable from linear to circular, the FERMI project has chosen the APPLE-II configuration [45] for the final radiators (FEL-1 radiator and FEL-2 second stage radiator). For the initial modulator, a simple, linearly-polarized configuration is optimal both due to its simplicity and because the input radiation seed is linearly polarized. As the short first modulator produces little if any gain, there is little cost or space advantage in using a circular polarization for which the electron beam/radiation coupling is somewhat better. For the case of the first stage radiator and second stage modulator (for the fresh bunch approach [46]), FEL-2, will use linearly-polarized undulators, because of their simplicity and lower cost.

Wavelength tuning in the undulators will be done by changing the gap rather than by changing the electron beam energy. Hence, the maximum wavelength reachable for a given fixed beam energy is set by the magnetic field at the undulator pole tips, the minimum gap obtainable, and the undulator wavelength. These considerations strongly constrain the available parameter space, especially for FEL-1.

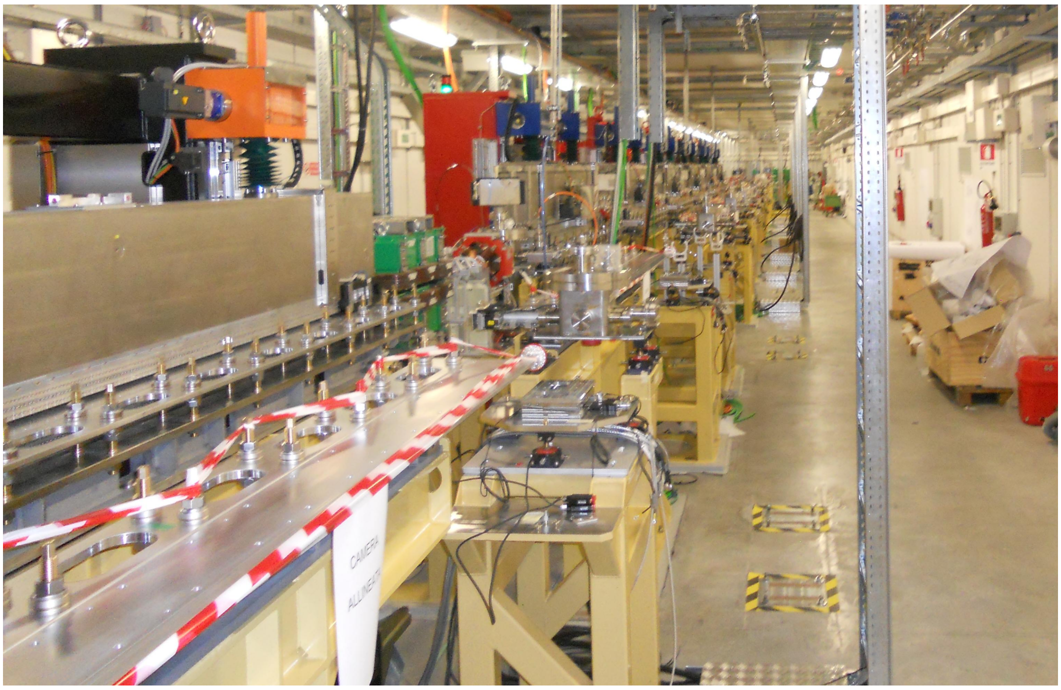

Figure 3.7: Undulator hall of FEL-1.

For the first modulator, which must satisfy FEL resonance over a nominal wavelength range of 240 to 360 nm, the undulator wavelength selected is 260 mm. For the second stage modulator of FEL-2, the adopted undulator wavelength of 55 mm agrees with that chosen for the first stage radiator (see the discussion in the next paragraph).

The choice of undulator wavelength for the radiators is driven by two principal requirements: (1) the FEL resonance be physically possible at the longest desired output wavelength (i.e., 100 nm for FEL-1 and 40 nm for FEL-2) at an electron beam energy of 1.2 GeV; (2) there be reasonable gain at the shortest desired output wavelength. The first requirement drives one to small gaps and longer wavelengths. The second requirement pushes one to shorter wavelengths. The present design choice is a minimum gap opening of 10 mm; this value allows for an 8 mm stay clear, a 1 mm pipe thickness, and 1 mm clearance. With all this in mind, a 65 mm wavelength was chosen for the FEL-1 radiator and first FEL-2 radiator and a 50 mm wavelength for the final FEL-2 radiator.

3.7 The Seed Laser

The seed laser is a multi-stage system including an IR oscillator developed for the laser group in Elettra and a Legend amplifier assembled by Coherent [47]. The oscillator is a passive model locked Ti:Sapphire cavity pumped by a 4.5 mW diode laser. The mode locking allows entering in a pulse regime that is adapted to the total cavity length. When optimized, the oscillator delivers 120 fs (FWHN) pulses with 3 nJ energy per pulse at the fundamental wavelength in the range 780-800 nm. The oscillator emission seeds the Legend amplifier which increases the energy of a single pulse up to 2.5 mJ at the fundamental wavelength. The pulse duration can be changed by means of two compressors with a flipper that allows switching. In particular, two different schemes can be chosen in order to obtain either 100 fs or 1 ps ”transform limited” pulse. The operational repetition rate range is between 1 Hz to 1 kHz.

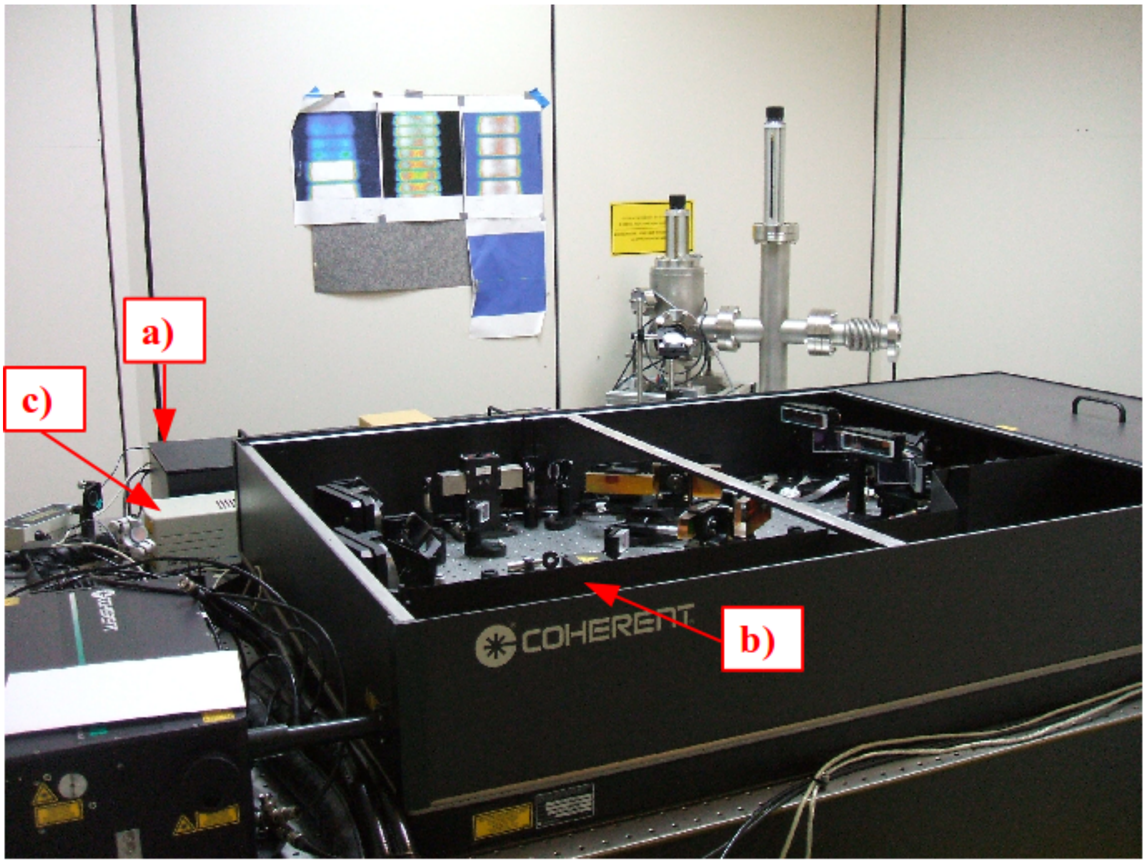

Figure 3.8: The seed laser system. (a) Ti:Sapphire oscillator, (b) Ti:Sapphire amplifier, (c) diode laser.

By second and third harmonic generation in BBO crystals, the wavelength ranges of 390-400 nm and 260-267 nm can also be covered with pulse energies of about 0.8 and 0.3 mJ, respectively. The peak power is thus high enough for seeding the electron bunch also in the blue and UV. Fig. 3.8 shows the laser system that is located in the FEL back-end station. To optimize the energy transfer from the laser to the electron bunch, thus yielding the best micro-bunching with the lowest seed power, the laser pulses must be precisely aligned with respect to the electron bunch both in space and time.

3.8 Experimental Area

After leaving the undulators, the electron beam is dumped into a shielding block by a sequence of bending magnets (see Fig. 3.9), while the FEL radiation is transported to the experimental area, shown in Fig. 3.10.

The transport optics is designed to handle the high power density (up to 10 GW) in a very short temporal interval. In order to handle the high peak photon energy density, the beam line

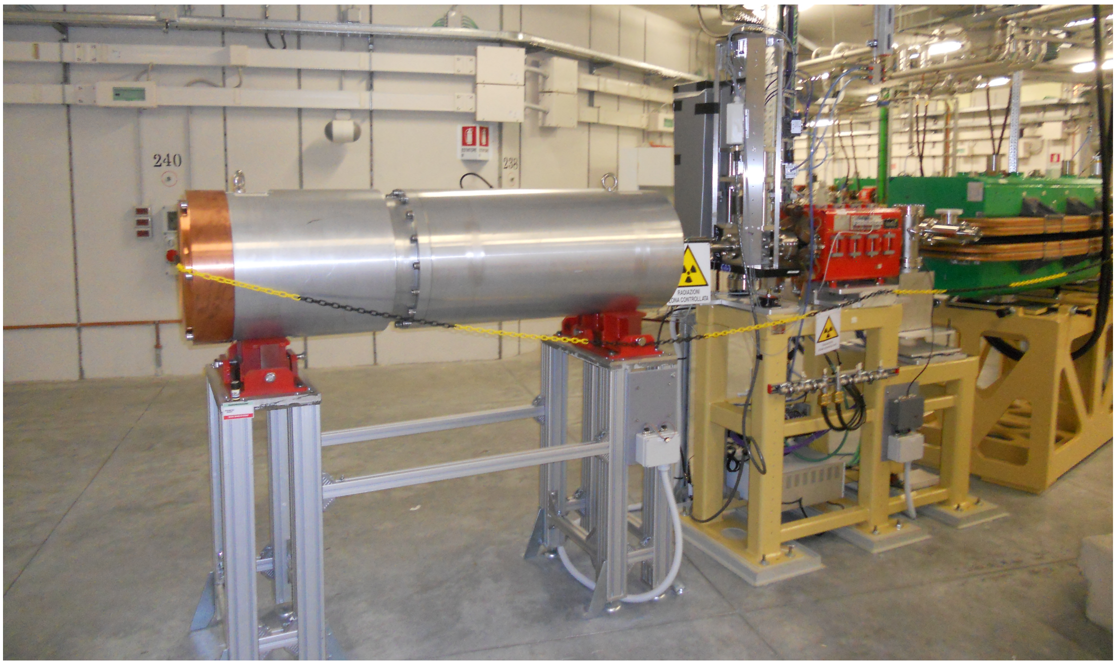

Figure 3.9: The beam dump area.

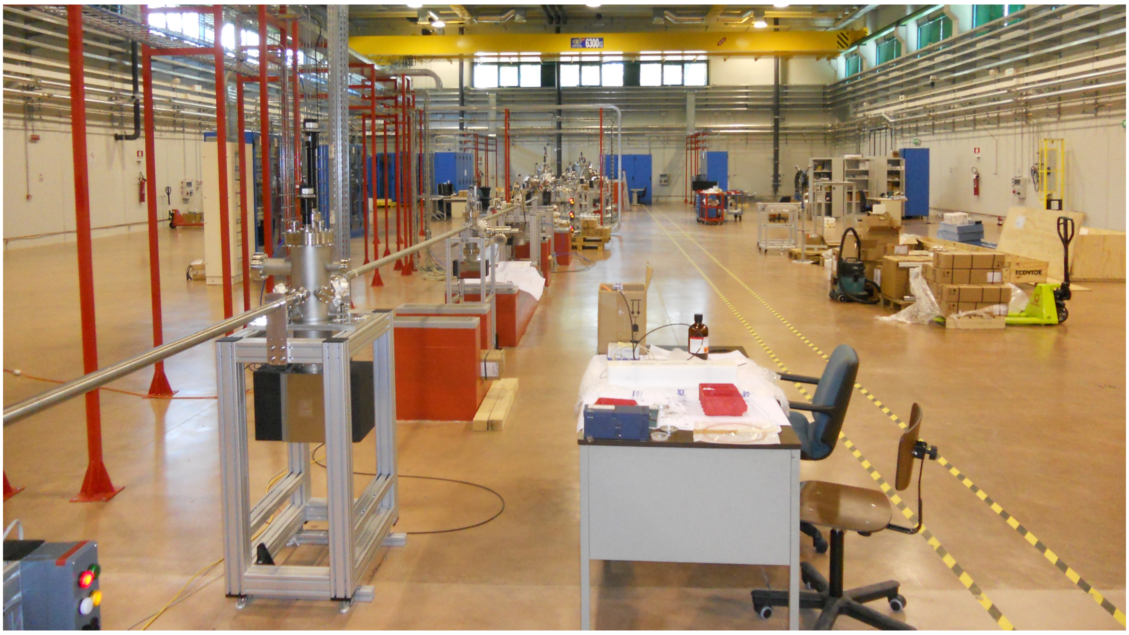

Figure 3.10: The experimental area.

optics operate at low grazing incidence angle with low Z-materials and the radiation intensity can be controlled by a gas absorption cell. The vacuum system is windowless with differential pumping sections. Pulse length preservation, monochromatization, energy resolution, source shift compensation, focusing in the experimental chamber and beam splitting are all included in the design of the FEL radiation transport system [48].

The Photon Analysis Delivery and Reduction System (PADReS) was designed to collect the radiation coming from both the undulator chains (FEL1 and FEL2), to characterize and control it, and to redirect it towards the following beamlines. The first parameters that are checked are the pulse-resolved intensity and beam position. For each of these parameters, two dedicated monitors are installed along PADReS on each FEL line. In this way it possible to determine the intensity reduction that is realized by the gas reduction system, which is capable of cutting the intensity by up to four orders of magnitude. The energy distribution of each single pulse is characterized by an online spectrometer installed in the experimental hall. Taking advantage of a variable line-spacing grating, it can direct the almost-full beam to the beamlines, while it uses a small fraction of the beam itself to determine the spectral distribution of each pulse delivered by the FEL.

3.9 Expected Performance

A campaign of time-dependent start-to-end simulations was performed to predict the performance of the linac and FEL. We were especially interested in the performance of the electron beam emittance and energy jitter. The expected performance of the electron beam for FEL-1 and FEL-2 is shown in Table 3.4 [49].

Table 3.4: The expected electron beam and FEL performance.

Parameters	**FEL-1**	**FEL-2**	**Units**
Emittance (rms)	1.5-3	1	mm mrad
Energy spread	<1.2	<1.5	MeV
Energy jitter (rms)	0.1	0.1	%
Timing jitter (rms)	<150	<150	fs
Output pulse length (rms)	≤50	≤50	fs
Peak power	1-5	>0.3	GW
Photons per pulse	$> 10^{13}$	$> 10^{12}$	

For FEL-1, the output power is relatively insensitive to the actual value of the energy spread so long as the input laser power and modulator length can produce a coherent energy modulation ΔE an order of magnitude greater than σ_E. A nominal laser power of 100 MW has been adopted. The laser beam comes to a focus halfway in the modulator with a rms waist size of 300 μm. This value is significantly greater than the electron beam transverse size so as to minimize the induced incoherent energy spread.

Chapter 4

Commissioning of the FERMI FEL

4.1 Introduction

In this Chapter we present and discuss the work done for the commissioning of the FERMI linear accelerator and free electron laser. The main goal of this commissioning was to produce FEL radiation for the user's activity. Taking advantage of this, I participated in the commissioning process and performed measurements of the electron beam parameters at various locations along the linac in order to characterized the electron beam quality. This is important for the performance of the FEL source, described in the next Chapter. In next phase of commissioning we have overlapped in time and space the electron beam with the external seed laser in the first undulator segment and activated the FEL.

The following beam parameters have been considered:

- The bunch energy distribution, i.e. the average kinetic energy of the electrons and the energy spread around the average value.
- The peak beam current, together with the temporal charge distribution.
- The electron beam optical properties, described in terms of transverse beam emittance and Twiss functions (see Section 2.2.1).

4.2 Measurements of the Electron Beam

Here we report the results of the measurements on the electron beam, performed during the commissioning. We start with the generation of the electrons in the photoinjector and continue with the electron beam characterization.

In this Section, we will also address the problem of unwanted variation of the accelerator settings during operation. The FEL operation imposes stringent tolerances for the stability of the linac output parameters: electron bunch arrival time, peak current and relative mean energy, among others. Generally, electron beam parameters are significantly dependent on RF phase and voltage jitters of the linac. Beam energy fluctuations, induced by the jitter of RF settings, transforms into arrival time jitter at the entrance of the modulator. As we will see, this may spoil the seed-electron overlap inside the modulator and, as a consequence, the FEL stability at the exit of the radiator.

4.2.1 Electron Generation and Acceleration

The drive laser of the photoinjector is the third harmonic (~260 nm) of a Ti:Sa amplifier, with maximum energy per pulse of about 0.5 mJ (see Section 3.4.2). Fig. 4.1 shows the typical uniform transverse intensity (almost flat-top) distribution of the photoinjector laser and the temporal profile.

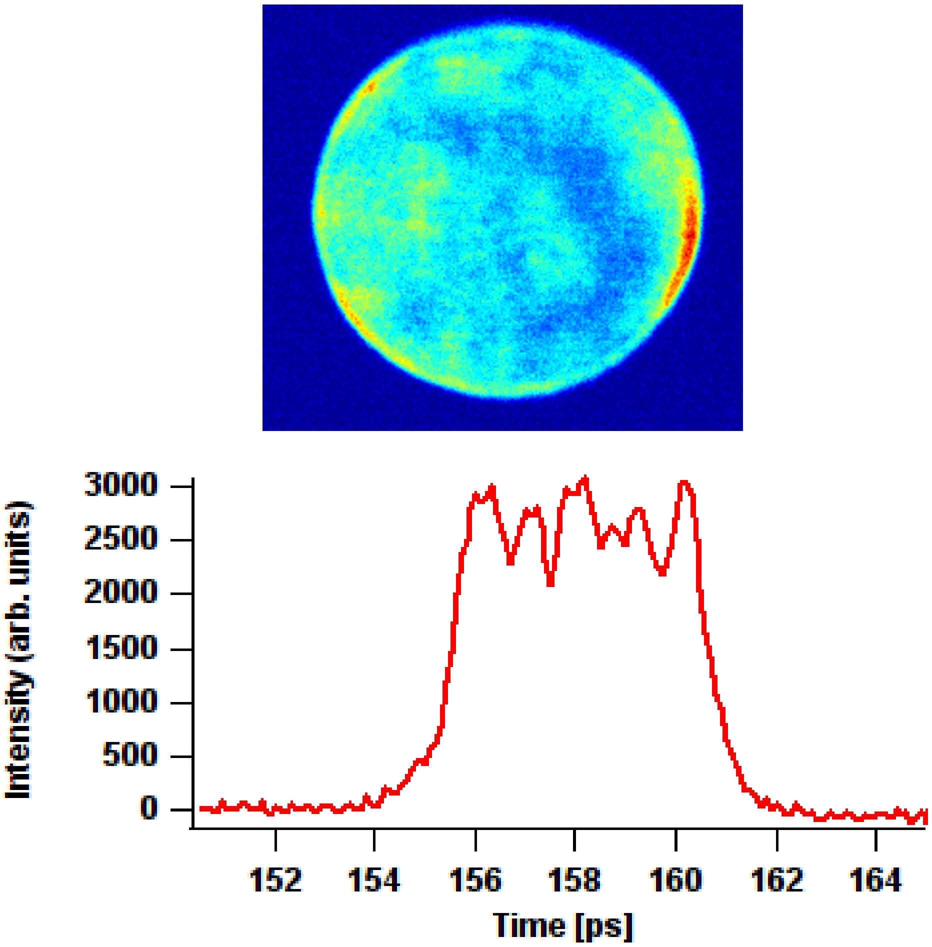

Figure 4.1: (*Up*) Spot of the photoinjecor laser and (*down*) its temporal profile.

After the electrons are extracted from the Cu cathode, they pass through successive accelerating RF cavities. The total extracted charge is selected by the laser power sent on the cathode. During commissioning, we mainly generated beam charge of 350 pC (the nominal charge is 800 pC [50]). This selection of charge was done in order to reduce the instabilities related to space-charge and geometric wakefields (external fields on the beam pipe). The space-charge is the repulsive Coulomb force due to the high density of charged particles in the bunch. This distorts the phase space ellipse (Section 2.2.1), increasing the transverse emittance.

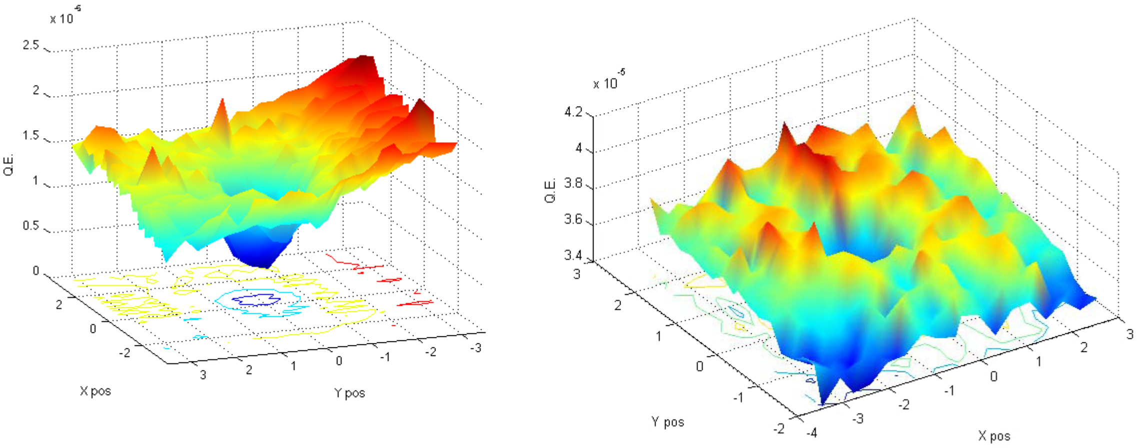

Figure 4.2: Q.E. map before (*left*) and after (*right*) the Ozone gas treatment. This map of the photocathode Q.E. over the region of interest is obtained by sweeping a small size laser spot over the cathode and measuring the emitted electron current.

Degradation of the quantum efficiency (Q.E.)[1] has been experienced, probably due to the deposition of residual gas on the Cu surface induced by the interaction with the UV driven laser or by the electron beam itself. Moreover, the Q.E. drop is localized in the cathode center where the UV laser is more often driven (see Fig. 4.2 left). The Q.E. has been successfully re-established every time with an Ozone cleaning procedure. The cleaning procedure consists of venting the RF gun with Ozone gas for few hours and baking it out for 2 days. Fig. 4.2 shows the comparison between the Q.E. map before and after the ozone cleaning.

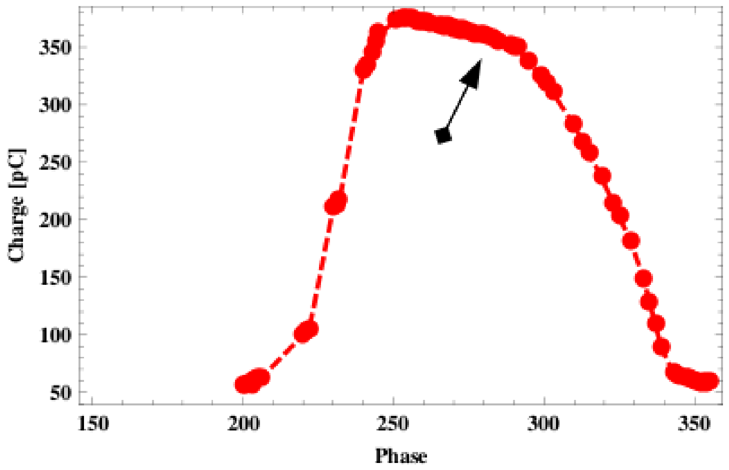

Figure 4.3: Scan of the charge measured by a Faraday cup vs. RF phase of the gun. The arrow indicates the selected phase.

The cathode is located in a resonant RF cavity cell. Inside the cell there is an oscillating electric field that accelerates the electrons. The photoinjector laser is synchronized with the RF cavity, so that the extracted electrons always experience a positive electric field. We must optimize the generated electron bunch. This is done by making a scan of the phase shifter that changes the phase of the photoinjector laser with respect to the RF field inside the cavity and measuring the charge (using a Faraday cup) at the exit of the RF cell. This is shown in Fig. 4.3. We do not select the RF phase corresponding to the maximum degree. Instead, we typically set an offset at about 30 degree (indicated by the arrow). By doing this, we search the maximum of the beam energy at the exit of the gun, consequently reducing the impact of space charge on the emittance.

---

[1] The quantum efficiency is the ratio of the number of emitted electrons to the number of incident photons.

After the optimization of the RF gun, we do a scan of individual RF sections field phase and measure the energy of the electron bunch. We select the energy of individual sections so that we reach the energy at the end of the linac of about 1.2 GeV. This is not the maximum energy but we can achieve this value also without some individual accelerating sections. In case we got faults in some RF sections, we can still operate the linac and consequently the FEL.

4.2.2 Beam Profile

The beam profile monitors (screens) are used to image the full beam at several locations along the beamline. For this purpuse, thin Yttrium-Aluminium-Garnet (YAG) crystal sheets doped with visible light scintillator Cerium are inserted into the beampath to produce an image of the transverse charge distribution.

We can also use these YAG screens for measuring the length of the electron bunch. This is done in combination with a transverse RF deflecting structure that sweeps the beam transversally to the direction of propagation. At FERMI@Elettra, three deflecting cavities are scheduled at two points in the linac. Two, one per plane, will be placed at 1.2 GeV (high energy), just before the FEL process starts; the other at about 300 MeV (low energy), after the first bunch compressor (BC1). For the present study, we only used the low energy deflecting cavity, since the high energy is not yet installed.

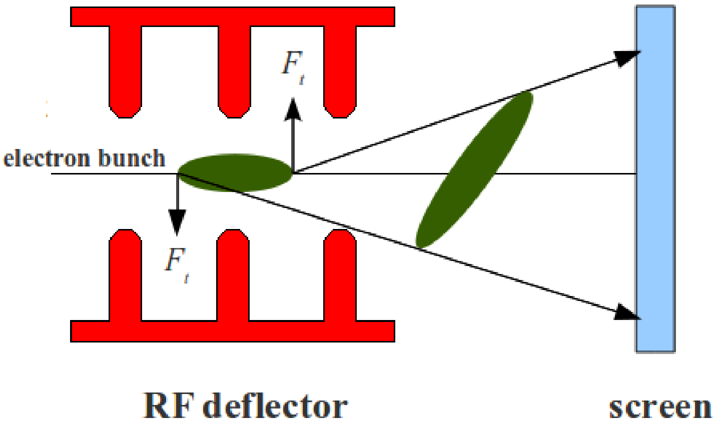

Figure 4.4: Deflection of the electron bunch: the centroid remains on axis while at the end of the bunch the transverse force F_t has opposite directions.

A RF deflector is a structure that produces a standing wave [51] and is composed by the repetition of five basic cells (Fig. 4.4). When the deflector is turned on, the electron bunch is stretched transverse to the axis by a transversal deflecting force F_t of the RF field and it collides with a detector screen that converts the beam signal into an optical signal, which is then processed. When the deflector is turned off, the detector screen is removed and the beam passes through the device without being deflected.

The RF deflector installed after the first bunch compressor was used to evaluate the efficiency of the BC1 compressor. We present two bunch length measurements. The first measurement has been performed with an uncompressed beam (Fig. 4.5), while the second was done with a beam compressed by a factor about 6 (Fig. 4.6).

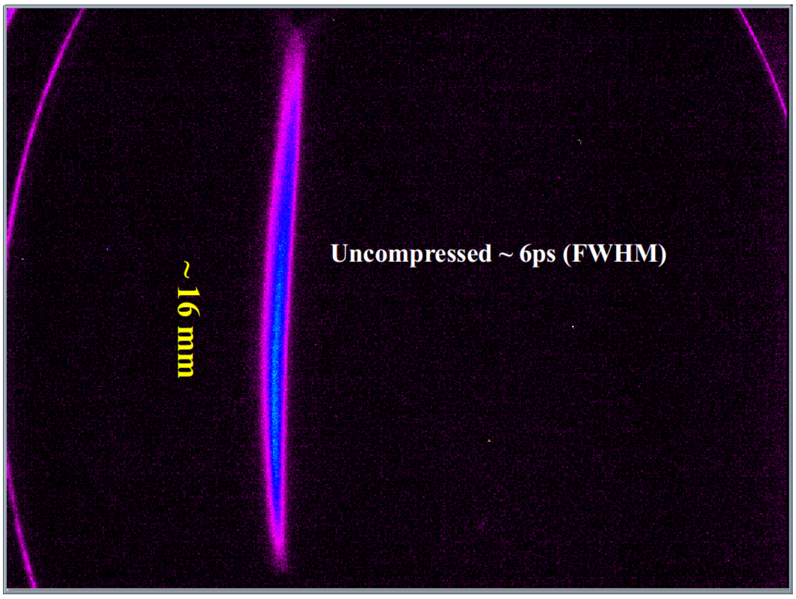

Figure 4.5: Vertical deflection of the uncompressed electron beam on a YAG screen.

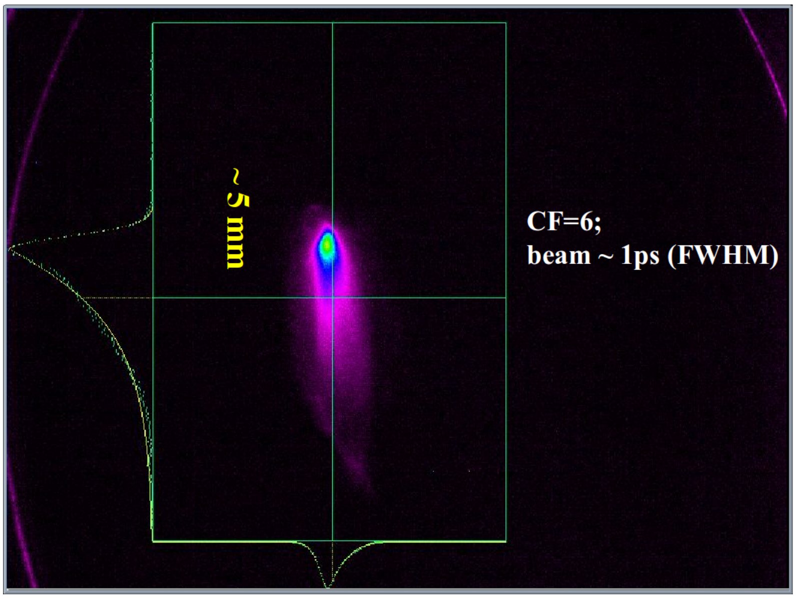

Figure 4.6: Vertical deflection of the electron beam compressed with factor ~6 on a YAG screen.

4.2.3 Energy Spread Measurement

During harmonic generation, the electron beam is separated into micro-bunches. The width of a single micro-bunch is determined by the energy spread of the electron beam (see Fig. 2.14, Section 2.4.5). This determines the maximum harmonic number one can reach.

Measurement of the beam energy spread in the linear accelerator is quite straightforward. For this purpose, Optical Transition Radiation (OTR)[2] screen plus a CCD camera are used in a region of high dispersion (behind a bending magnet). The dispersion determines the offset of the trajectory from the ideal path for particles with a relative energy deviation. The energy spread is computed as the ratio between the horizontal beam size Δx and the value of dispersion η_x in the bending plane [52],

$$\Delta E = \frac{\Delta x}{\eta_x}. \tag{4.1}$$

The technique is destructive and the measurement is performed during the commissioning and operation to keep track of the energy spread value.

We measured the energy spread in multiple parts of the linear accelerator: after the laser heater; after the first bunch compressor BC1 and at the end of the linac, in the main beam dump area. The result is shown in Table 4.1. Together with the increase in energy along the line, we can observe an increase in the energy spread. This increase in the energy spread is induced by off-crest arrival of the electron beam on the RF fields in the accelerating sections and by the presence of longitudinal wakefields in the linac (see Section 2.2.3).

Table 4.1: Energy spread at different energies and at different positions (shown in Fig. 2.2, Chapter 2) along the linac.

Position	**Energy E**	**Energy Spread ΔE**	**$\Delta E/E$**
Laser heater	98.5 MeV	56 keV	0.06%
BC1	319.58 Mev	377 keV	0.11%
Beam dump area	1250 Mev	2609 keV	0.20%

4.2.4 Time Jitter

The arival timing jitter of electron bunches is inevitable in RF accelerators due to RF noise, high power supply ripple and wakefields (see Section 2.2.3) [53, 54]. The fluctuation is induced by the RFs phase and amplitude jitter and my induce beam quality degradation. As the FEL stages are optimised for the parameters of the “on time” part of the bunch, the optimization will not match for different arrival times and a degradation in the performance is expected.

We also examined the effects of magnetic bunch length compression on the electron beam dynamics. The bunch compressor is designed in such a way that due to the energy spread variation (induced by the change of the RF phase), the electrons travel with different trajectories inside the magnetic chicane (Fig. 4.7).

---

[2] Optical Transition Radiation (OTR) is emitted when a charged particle crosses the surface between two materials with different dielectric constant. The emission is similar to the bremsstrahlung effect and is due to the sudden annihilation of the image charge induced in the material.

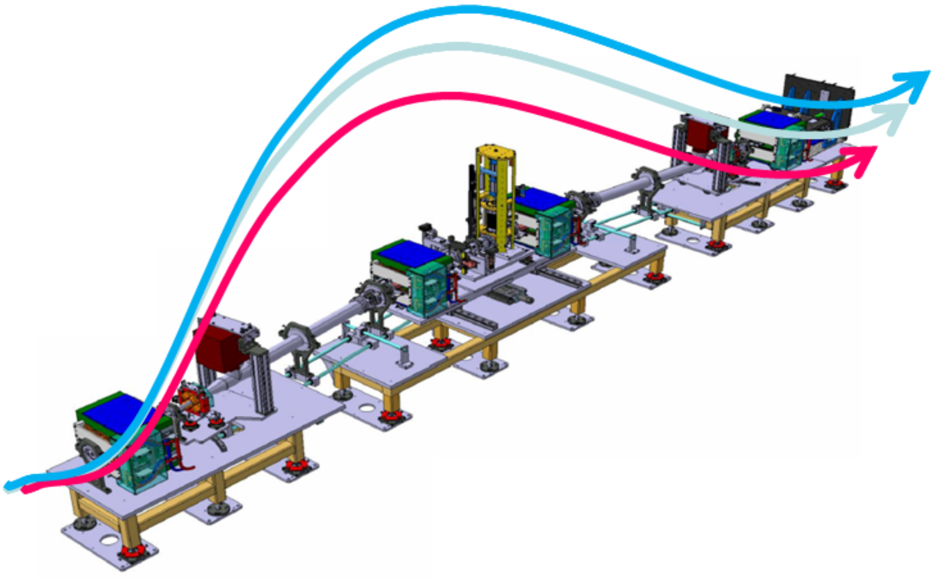

Figure 4.7: The electrons trajectory in a bunch compressor.

Particles with higher energies will perform a longer path than those with a smaller one. The result is an overall bunch length compression. The compression is performed in order to increase the peak current and by this the intensity of the FEL radiation [55]. During the implementation of this procedure, we observed an increase of the bunch arrival jitter and of the electron beam emittance. Especially in the application to seeded FELs, the timing jitter can be a serious operational problem. Indeeed, the external laser is synchronized with the arrival of the electron bunch in the modulator. Due to the jitter, the seeding radiation will interact every shot with a different part of the electron bunch and since different parts of the bunch may have different properties (e.g. energy and charge distribution) this may affect the performance of the FEL. This is also the reason why a X-band cavity will be installed in the future [56], that will homogenize the electron bunch.

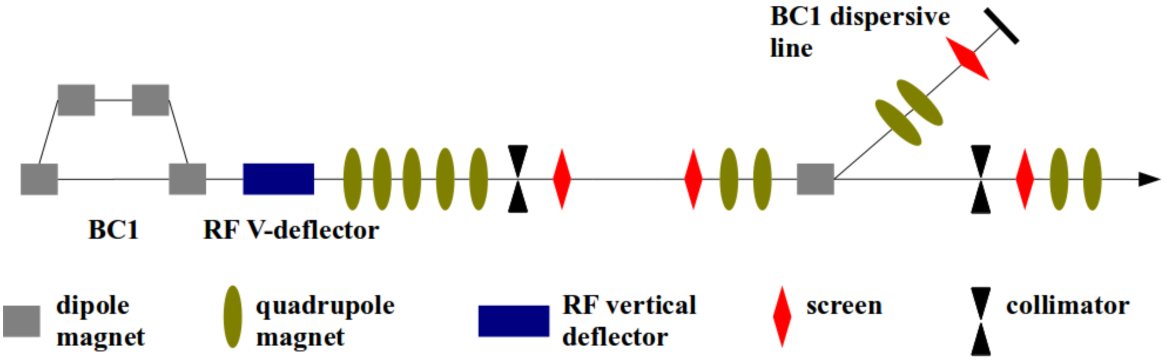

Figure 4.8: Layout of the FERMI BC1 area. A collimator is used in case we want to select just parts of the electron bunch.

Time jitter studies were done in the first bunch compression (BC1) diagnostics area. The layout of the BC1 area is sketched in Fig. 4.8.

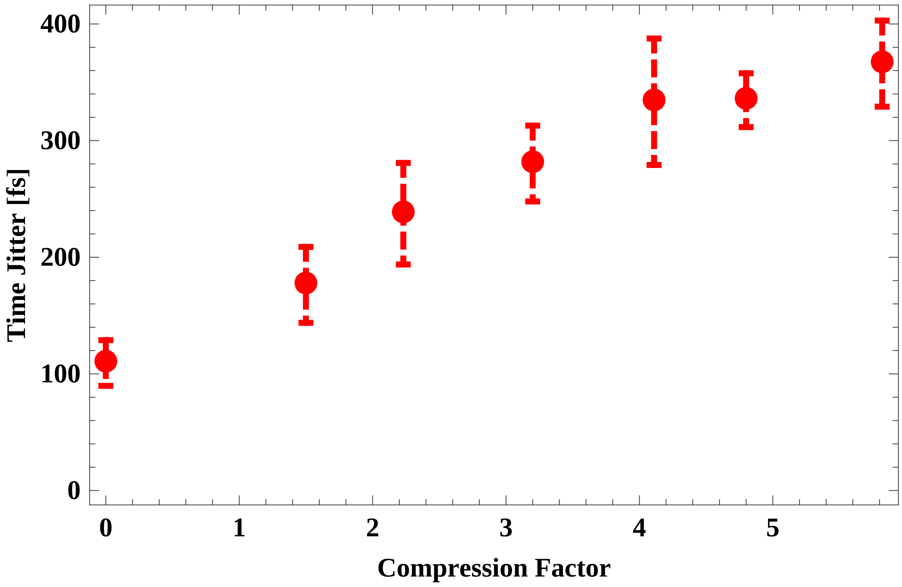

Figure 4.9: Time jitter as a function of the bunch length compression factor.

We investigated the relationship between compression factor and time jitter. We measured the time-jitter at different bunch compressor factors and noticed a significant increase of the timing jitter as we started compressing the beam. The results are shown in Fig. 4.9. Due to the non-perfect stability of the overall system, multiple measurements corresponding to the same compression factor gave us different results, so we plotted the average values with the corresponding error bars. The reason for this increase is that the RF cavities are synchronized with the bunch arrival so that it always arrives on the RF waves crest. During bunch compression we set bunch off-crest, so we are more sensitive to the RF phase jitter that translates into time jitter in BC1.

In the later shifts, a mishandling of the system controlling the RF stability of several parts has been found. After this was fixed, a time jitter around 100 fs was measured downstream of BC1.

4.2.5 Emittance Measurements

In combination with the beam optical functions, the emittance determines the transverse beam size and motion, according to Eq. (2.9) (Section 2.2.1). As emittance increases, the beam size increases as well, so electrons move more off-axis. This is important during the FEL process since undulator field has a sinusoidal dependence on axis, so off-axis electrons experience a different field and thus a different undualtor strength K. This will result in the shift of the wavelength of the emitted radiation. The result of this is in different electrons emitting different radiation (according to the resonance condition in Eq. (2.60)) and as a consequence we will have a broadening of the bandwidth. Also, the spread in the transverse motion degrades the synchronization of the electrons with the seed radiation field because the longitudinal velocity is modulated by the betatron oscillation. This means that FEL amplification is affected by the transverse emittance similar to a larger energy spread, resulting in an increase saturation length with reduced radiation power.

Especially for shorter wavelengths, it is critical to control the beam size and to guarantee a good overlap between the radiation and the beam. The emittance must not be larger than the wavelength of the laser and sets a limitation on the shortest wavelength at which we can achieve FEL. The emittance studies have been focused on a 350 pC beam. We used the quadrupole scan technique to measure the beam emittance. The quadrupole scan is a technique to measure the beam emittance and the optical parameters of the electron distribution as a function of the quadrupole field strength Z.

Quadrupole Scan

Here we explain the quadrupole scan technique and also present the obtained result. For a quadrupole magnet the transport matrix (Eq. (2.11), Chapter 2) has the form

$$R_x = \begin{pmatrix} \cos\bar{\phi} & \frac{1}{\sqrt{|k|}}\sin\bar{\phi} \\ \sqrt{|k|}\sin\bar{\phi} & \cos\bar{\phi} \end{pmatrix}, \qquad R_y = \begin{pmatrix} \cosh\bar{\phi} & \frac{1}{\sqrt{|k|}}\sinh\bar{\phi} \\ -\sqrt{|k|}\sinh\bar{\phi} & \cosh\bar{\phi} \end{pmatrix} \tag{4.2}$$

where $\bar{\phi} = \sqrt{|k|}l$ (l is the device length and k is the beam focusing). Here R_x and R_y represent horizontal defocusing and vertical focusing, respectively. If $k < 0$, R_x and R_y are interchanged and we obtain horizontal focusing and vertical defocusing. If the focal length $\bar{f}$ of the quadrupole is much larger than the length of the quadrupole, we can put $\bar{f} = 1/(kl)$ and simplify the transfer matrices in

$$R_x = \begin{pmatrix} 1 & 0 \\ 1/\bar{f} & 0 \end{pmatrix}, \qquad R_y = \begin{pmatrix} 1 & 0 \\ -1/\bar{f} & 0 \end{pmatrix}. \tag{4.3}$$

We refer to the quantity $Z = 1/\bar{f}$ as the field strength of the quadrupole.

Considering the quadrupole matrix R and a matrix S

$$S = \begin{pmatrix} S_{11} & S_{12} \\ S_{12} & S_{22} \end{pmatrix} \tag{4.4}$$

describing the path from the quadrupole to the screen, the total transfer matrix is given by

$$RS = \begin{pmatrix} S_{11} + ZS_{12} & S_{12} \\ S_{12} + ZS_{22} & S_{22} \end{pmatrix}. \tag{4.5}$$

If we represent the beam matrix at the input section of the quadrupole with

$$\sigma_0 = \begin{pmatrix} \sigma_{11_0} & \sigma_{12_0} \\ \sigma_{12_0} & \sigma_{22_0} \end{pmatrix} \tag{4.6}$$

the beam matrix at the screen is given by

$$\sigma_S = \begin{pmatrix} \sigma_{11_S} & \sigma_{12_S} \\ \sigma_{12_S} & \sigma_{22_S} \end{pmatrix} = (RS)\sigma_0(RS)^T. \tag{4.7}$$

The element $\sigma_{11_S} = \langle x^2 \rangle$ is obtained by observing the bunch image at the screen. This element is related to the quadrupole field strength Z, to the matrix S elements and to the beam matrix elements by means of

$$\begin{aligned}\sigma_{11_S} \;&=\; (S_{11}^2\sigma_{11_0} + 2S_{11}S_{12}\sigma_{12_0} + S_{12}^2\sigma_{22_0}) + \\ &\qquad (2S_{11}S_{12}\sigma_{11_0} + S_{12}^2\sigma_{22_0})Z + S_{12}^2\sigma_{11_0}Z^2 \end{aligned} \tag{4.8}$$

which can be written as

$$\sigma_{11_S} = AZ^2 - ABZ + (C + AB^2) \tag{4.9}$$

where we have placed

$$\begin{aligned} A &= \sigma_{11_0}S_{12}^2, \\ -2AB &= 2S_{11}S_{12}\sigma_{12_0} + 2S_{12}^2\sigma_{22_0}, \\ C + AB^2 &= S_{11}^2\sigma_{11_0} + 2S_{11}S_{12}\sigma_{12_0} + S_{12}^2\sigma_{22_0}. \end{aligned} \tag{4.10}$$

The S matrix and the quadrupole strength are known and for every value of Z can be measured a value of σ_{11_S}. Using three or more different values of Z it is possible to obtain A, $-2AB$ and $C + AB$ with a parabolic fitting. Thus also the value of A, B and C can be calculated. From Eq. (4.10) we can obtain the beam matrix elements σ_{11_0}, σ_{12_0} and σ_{22_0} and hence the emittance can be recovered by the Eq. (2.11) in Section 2.2.1 from which we get

$$\varepsilon = \frac{\sqrt{AC}}{S_{12}^2}. \tag{4.11}$$

The Twiss parameters can be calculated as

$$\begin{aligned} \beta_e &= \sqrt{\frac{A}{C}}, \\ \alpha_e &= 2\sqrt{\frac{A}{C}}(B + \frac{S_{11}}{S_{12}}), \\ \gamma_e &= \frac{S_{12}^2}{\sqrt{AC}}\left[(AB^2 + C) + 2AB\left(\frac{S_{11}}{S_{12}}\right) + A\left(\frac{S_{11}}{S_{12}}\right)^2\right]. \end{aligned} \tag{4.12}$$

Here we report emittance measurement performed in the bunch compressor area BC1. As seen in Fig. 4.8, after the RF vertical deflector five quadrupoles have been placed. During the normal operation, the quadrupole operation is regulated by varying the current I, which is related to the quadrupole strength Z by

$$Z \propto \frac{\bar{l}I}{E_{\text{tot}}} \tag{4.13}$$

where $\bar{l}$ is the quadrupole length. While performing a quadrupole scan in the BC1 area, the first four quadrupoles are left to their nominal current values, which drives the bunch to the design orbit and to maintain a large beam size in focus. The last quadrupole is employed with different current settings, which are used to perform the parabolic fitting of the beam size as a function of Z.

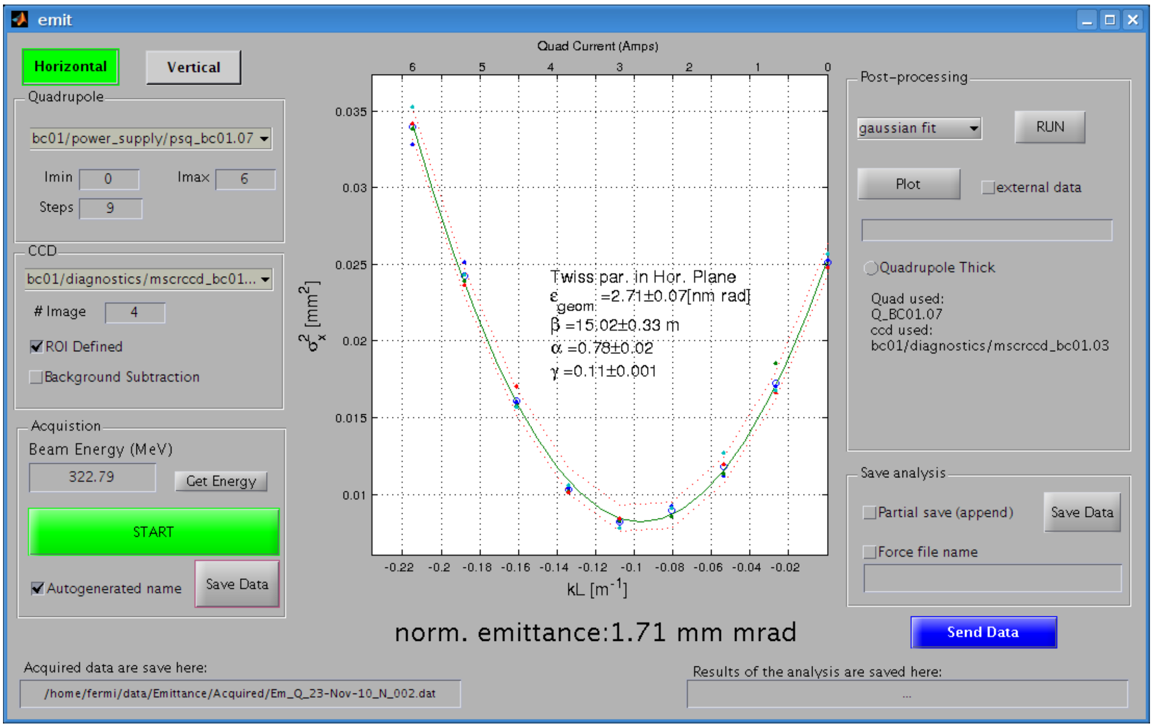

Quadrupole: bc01/power_supply/psq_bc01.07

Imin 0 Imax 6

Steps 9

CCD: bc01/diagnostics/mscrccd_bc01...

Image 4

☑ ROI Defined

☐ Background Subtraction

Beam Energy (MeV) 322.79 Get Energy

☑ Autogenerated name

gaussian fit

☐ external data

○ Quadrupole Thick

Quad used:
Q_BC01.07
ccd used:
bc01/diagnostics/mscrccd_bc01.03

☐ Partial save (append)

☐ Force file name

Twiss par. in Hor. Plane
ε_{geom} =2.71±0.07[nm rad]
β =15.02±0.33 m
α =0.78±0.02
γ =0.11±0.001

norm. emittance:1.71 mm mrad

Acquired data are save here:
/home/fermi/data/Emittance/Acquired/Em_Q_23-Nov-10_N_002.dat

Results of the analysis are saved here:
...

Figure 4.10: Parabolic fitting of horizontal beam size σ_x^2 as a function of $Z = kl$ for a compressed bunch with $E_{\text{tot}} = 322.79$ MeV.

We report in Fig. 4.10 the horizontal emittance ε_x measurement for an uncompressed beam, performed by varying the last quadrupole current from $I = 0$ A to $I = 6$ A in nine steps. The beam energy was $E_{\text{tot}} = 322.79$ MeV. We measured $\varepsilon_x = 1.71$ mm mrad. This is a good value compared to the expected performance (see Section 3.9), although we are still at the beginning of the linac. We will see that traveling through the linac leads to an increase of the emittance.

Later, with installation of new beam optics, $\varepsilon_x \approx 1$ mm mrad are typically measured in the BC1 area for a compressed beam.

Emittance vs. Compression Factor

Effects of the compression on the emittance generally lead to an increase in the horizontal plane. Fig. 4.11 shows the normalized emittance measured in BC1 area as a function of the compression factor (CF). Emittance measurements are reported for the horizontal (upper points) and vertical plane (lower points). Again, due to the instabilities in the linac we got for multiple measurements at the same factor different result and we plotted the average values with corresponding error bars. We noticed an increase of the emittance. This is due to the presence of transversal wakefields along the beamline. Transverse wakefields are excited if the beam traverses an accelerating structure off-axis. The fields excited by the head of the bunch will kick the tails of the bunch even more off axis and induce a dispersion. This can strongly dilute the emittance of the beam. We also notice that the vertical emittance is smaller and also its growth is not so affected by the compression factor. The reason for this is that dispersion induced by the bunch compression is in the horizontal plane and does not affect the vertical phase distribution.

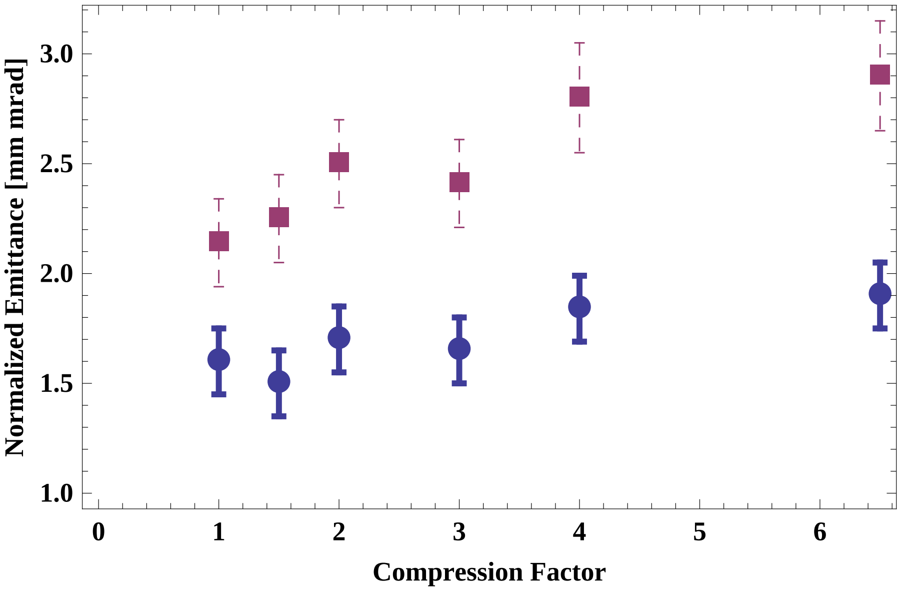

Figure 4.11: Normalized emittance measurement done in the BC1 area vs the compression factor. The dashed square is horizontal emittance ε_x and thick circle is the vertical emittance ε_y.

Finally, we measured the emittance at the linac end. The result for different compression factors is shown in Table 4.2. The results predicted by simulations for the expected performance of the linac (Section 3.9) gives us the emittance result in the range from 1.5 to 3 mm mrad. We see that the experimental results surpass the predictions. This is due to the fact that the linac is still not stable and there are still problems with the stability of the RF accelerating sections.

Table 4.2: Horizontal emittance measured at the end of the linac for different compression factors.

Compression Factor	Emittance [mm mrad]
1	3.28
4.6	4.20
5.2	4.25

4.3 Seed Laser and Electron Beam Overlap

The next commissioning phase is the spatial and temporal overlap between the external seed laser (Section 3.7) and the electron beam inside the undulator and the activation of the FEL. The modulator was tuned to the wavelength of the seed laser (260 nm) and the 6 radiators were tuned to the 5th harmonic (52 nm). The main parameters of the seed laser are presented in Table 4.3.

4.3.1 Spatial Overlap

Spatial overlap between the seed laser and the electron beam is achieved in the modulator. We use two YAG screens located at either sides of the modulator. The laser and the electron beam

Table 4.3: Seed laser parameters.

Parameter	Value
Wavelength (nm)	260
Duration FWHM (fs)	100
Peak Power (MW)	∼10

are superimposed using a steering mirror for the laser light. Before the alignment we can observe the seed laser and the electron beam as shown in Fig. 4.12.

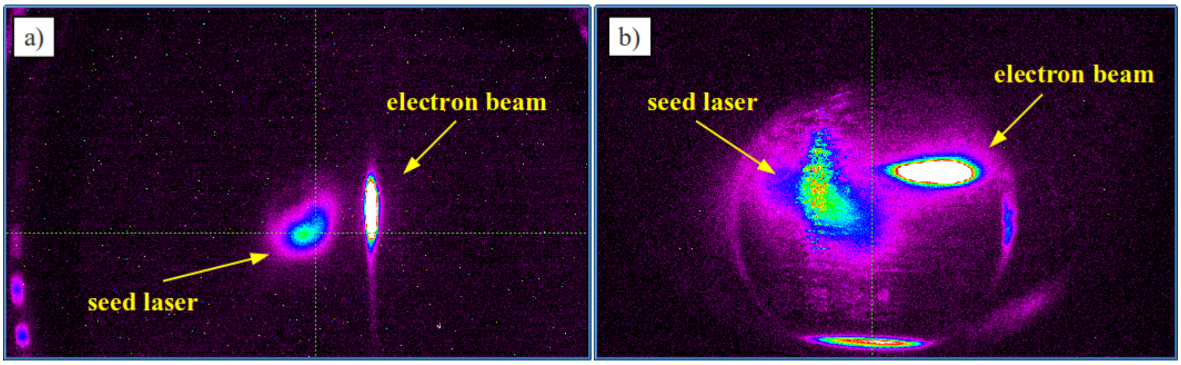

Figure 4.12: Seed laser and the electron beam at the a) beginning and b) end of the modulator, before the alignment.

Changing the inclination of the mirror we have a transverse alignment of the electron beam and the laser, as seen in Fig. 4.13.

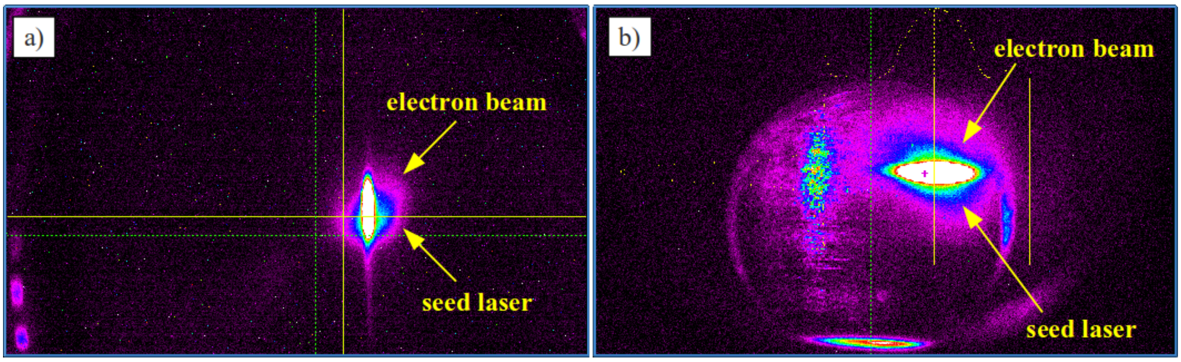

Figure 4.13: Seed laser and the electron beam at the a) beginning and b) end of the modulator, after the alignment.

4.3.2 Temporal Alignment

After the transverse overlap we must achieve a temporal alignment between the seed and the electron beam. The seed laser and the electron beam are detected on a photodiode installed in an electron-optical sampling (EOS) chamber. An aluminum foil is used to reflect the laser out of the chamber and to produce OTR from the electron beam. The two signals are then detected by means of a CCD and a fast photodiode (Fig. 4.14).

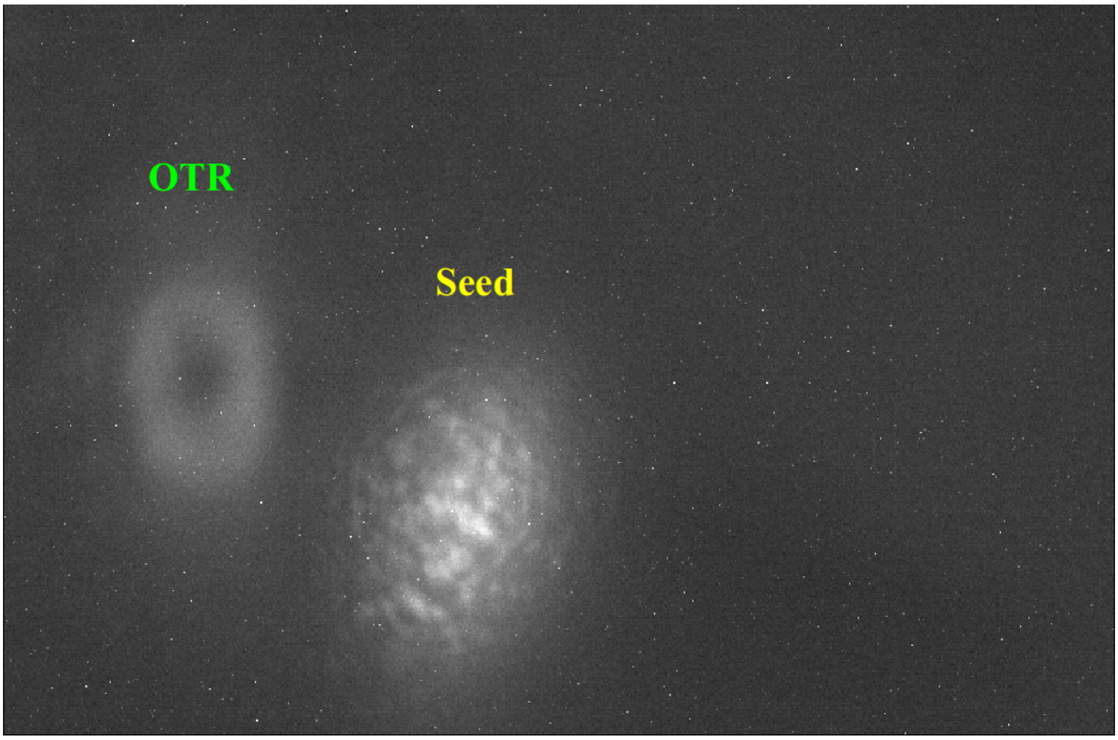

Figure 4.14: Optical transition radiation (OTR) and seed laser on electron-optical sampling (EOS) CCD.

Using a delay line to control the time arrival of the seed laser it is possible to obtain a temporal overlap between the electron beam and the seed laser within sub-ps. We can observe the two signals on Fig. 4.15 a) before and b) after the temporal alignment of the seed and electron beam. Doing this we achieved the activation of the FEL, as we will discuss in the next chapter.

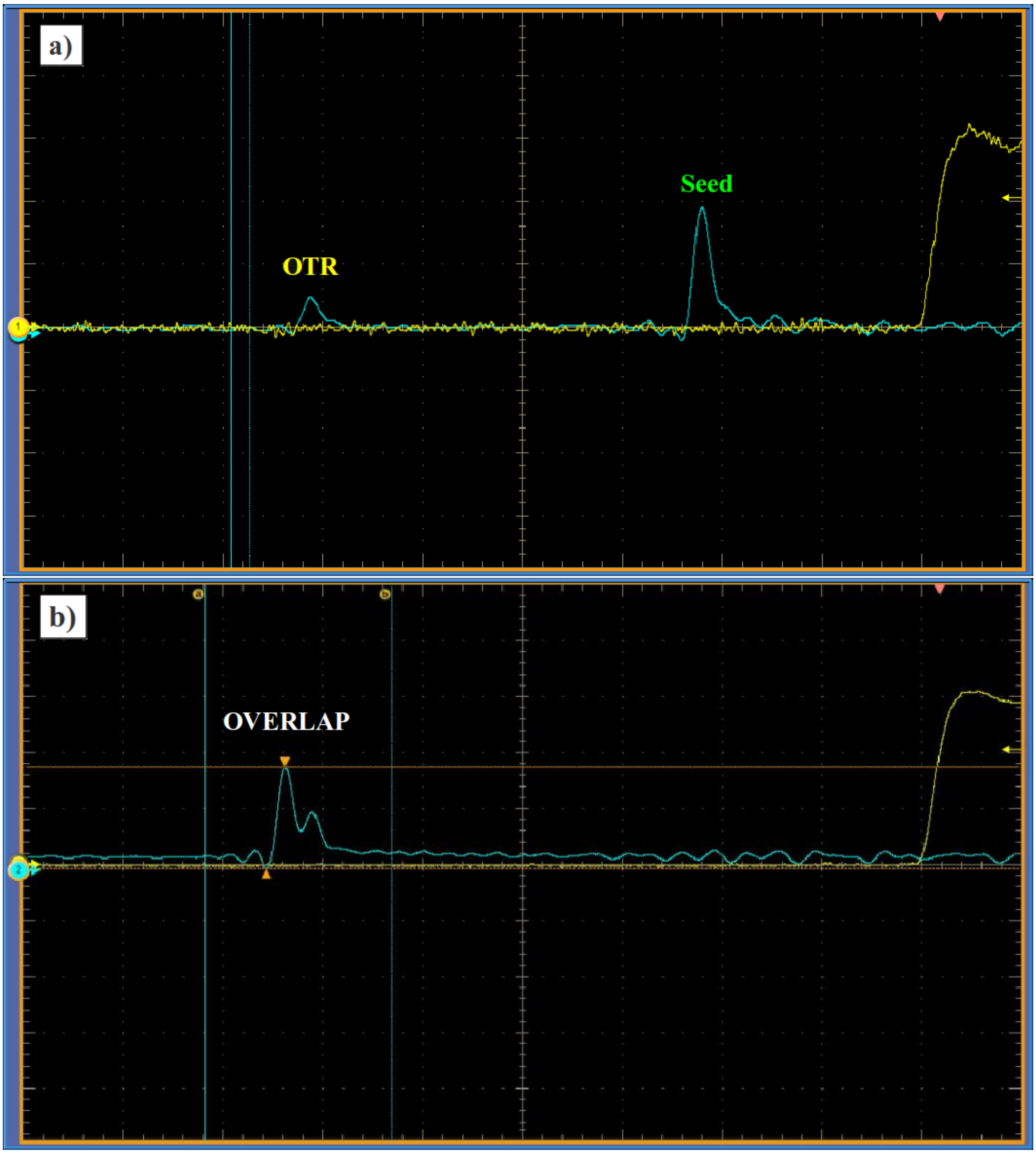

Figure 4.15: OTR and seed laser a) before and b) after the temporal overlap.

Chapter 5

Generation of Coherent Harmonics

5.1 Introduction

In the following, we present the experimental performance of the FEL harmonic radiation. After optimizing the electron beam and achieving a spatial and temporal alignment, we activated the FEL process. This allowed us to proceed with harmonic generation. We tuned the modulator to the wavelength of the seed laser (260 nm) and the 6 radiators to the 5th harmonic (52 nm). The radiation coming from the undulators is transported into the experimental hall where it is collected and characterized by Photon Analysis Delivery and Reduction System (PADReS) [59] (Section 3.8).

The goal of this Chapter is to present:

- The measured spectrum and intensity of the coherent harmonic emission.
- Perform scans of various parameters in order to optimize the coherent radiation.

We also observed the effect of the external seed laser on the electron beam and compared the FEL performance with a compressed and uncompressed electron bunch.

5.2 Measurement of the FEL Emission

The fine tuning of the temporal and spatial overlap, done in the previous Chapter, allows us to generate the FEL emission, see Fig. 5.1. This is first acquired on an oscilloscope by means of a fast photodiode. The curve a) represents a single FEL pulse. The trace b) shows a sequence of seeded FEL pulses, while the trace c) is the spontaneous emission from the electrons. The later was obtained after inducing a temporal detuning between the electron beam and the seed laser inside the modulator. The emission from seeded electrons is several orders of magnitude stronger than the spontaneous emission. We see that there are very strong fluctuations in the FEL emission. This is due to the fact that this was the first lasing and we must still optimize linac and FEL parameters.

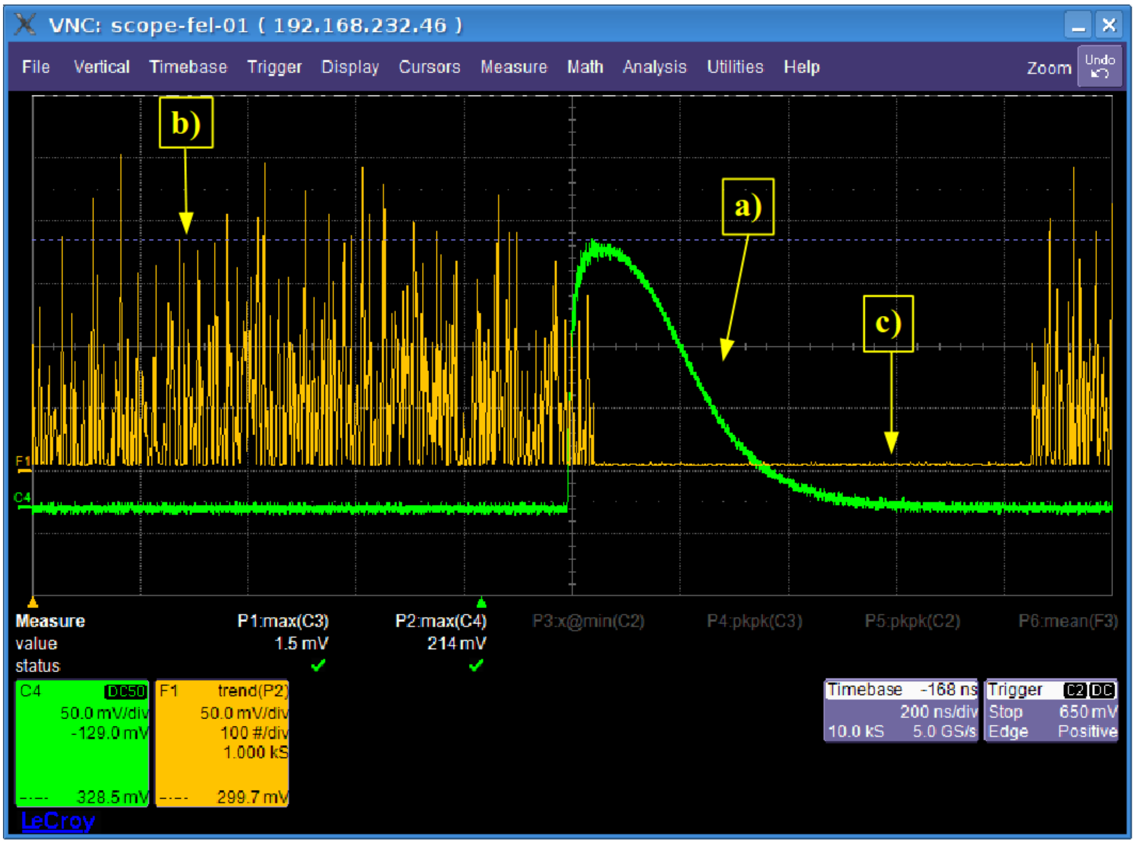

Measure	P1:max(C3)	P2:max(C4)	P3:x@min(C2)	P4:pkpk(C3)	P5:pkpk(C2)	P6:mean(F3)
value	1.5 mV	214 mV				
status	✓	✓				

C4 DC50
50.0 mV/div
-129.0 mV
328.5 mV

F1 trend(P2)
50.0 mV/div
100 #/div
1.000 kS
299.7 mV

Timebase -168 ns
200 ns/div
10.0 kS 5.0 GS/s

Trigger C2 DC
Stop 650 mV
Edge Positive

Figure 5.1: Intensity of the coherent emission, measured by means of a fast photodiode. The trace a) shows the time profile of a single pulse with the photodiode. The b) trace shows a sequence of seeded FEL pulses and c) is the spontaneous emission of the electron beam.

5.2.1 Optimization of the FEL Emission

The aim of the optimization is to find the values of the seed-electron beam temporal overlap, seed laser power, dispersive section strength, modulator and radiators gap at which the optimal output radiation power is obtained. For this reason, we observed FEL emission for different values of the above mentioned parameters.

First, we performed a scan of the seed laser temporal delay with respect to the electron beam and observed the FEL intensity. This is shown in Fig. 5.2. This delay scan also provides information about the active temporal profile (the one that contributes to the FEL process) of the electron bunch. The measured bunch length is around 2 ps which corresponds to the bunch compression factor 3. From this figure we can also observe the particle distribution inside the beam. In the case of a compressed beam the region where FEL emission occurs is strongly asymmetric as a consequence of the asymmetry of the beam current profile. More particles are concentrated in the points of higher output intensity.

Next, we optimize the interaction of the electron beam and the seed laser, in order to achieve optimum bunching. As explained in Section 2.4.4, the seed laser induces an energy modulation in the electron beam and the dispersive section (DS) converts this into bunching. So, the optimum value of the seed laser power corresponds to a specific value of the DS strength (and vice versa)

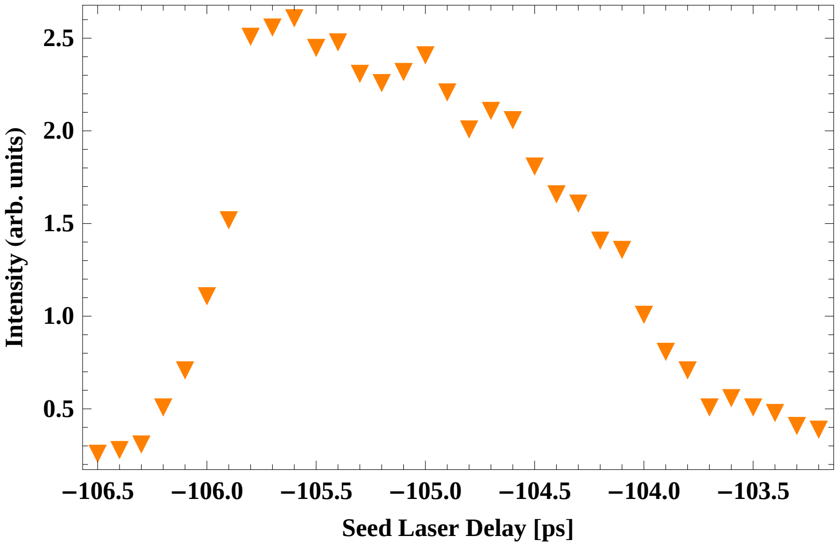

Figure 5.2: Seed laser temporal delay scan vs. FEL intensity.

since this two parameters determine the bunching. We performed a scan of the seed laser power for a value of the DS parameter R56 (see Eq. 2.95, Chapter 2) around 60 µm. This is presented in Fig. 5.3. We see from the figure, that the output intensity reaches a peak and after that starts to decline. This means that the power is too great and the beam goes into overbunching.

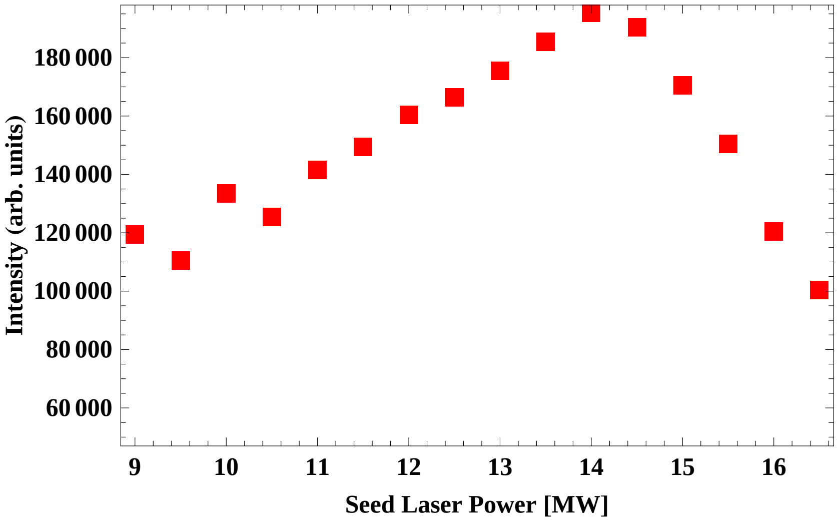

Figure 5.3: FEL intensity vs. seed laser power scan.

We can also do the other way around. Fixing the seed power close to the maximum, we performed a scan of the dispersive section strength by varying the R56. This is shown in Fig. 5.4. The output power experiences a peak around the R56 value of 60 µm and than we experience a decrease.

Measurements have also been done for the undulator wavelengths. From the resonance equation (Eq. (2.70), Chapter 2) we can select the central value of the wavelength and perform a scan

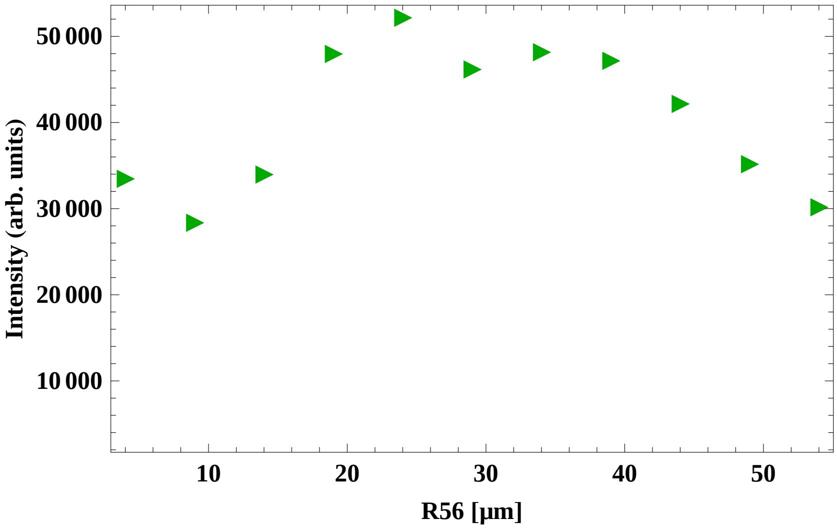

Figure 5.4: Intensity vs. the dispersive section strength.

around that value. This is done by adjusting the gap (see Section 3.6). The reason for this scan is due to the loss of energy that occurs during the electrons passage through the undulators. So, the resonance condition must undergo proper adjustment. The Fig. 5.5 on the left shows the output intensity with respect to the modulator wavelength. The gap that gives us the peak is close to 22.7 mm. This corresponds to the wavelength ∼260 nm which is the wavelength of the seed laser. A similar scan was performed for the radiators. This is presented for the first radiator in Fig. 5.5 on the right. We have a peak around 12.7 mm and this corresponds to the 5th harmonic of the seed (52 nm).

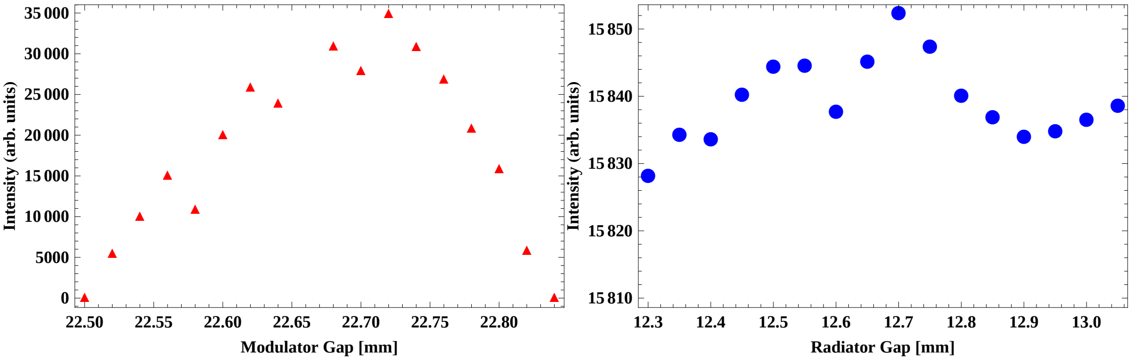

Figure 5.5: (*Left*) The output intensity as a function of the tuned gap of the modulator. (*Right*) The output intensity as a function of the tuned gap of the radiators.

Performing this various scans we achieved an optimization of the FEL emission. A visual comparison before and after the optimization is shown on Fig. 5.6. This figure shows just the transverse spot optimization. We can see that the emission spot of the non-optimized FEL is much more smudged and less intense. The shape of the optimized spot is also close to a Gaussian.

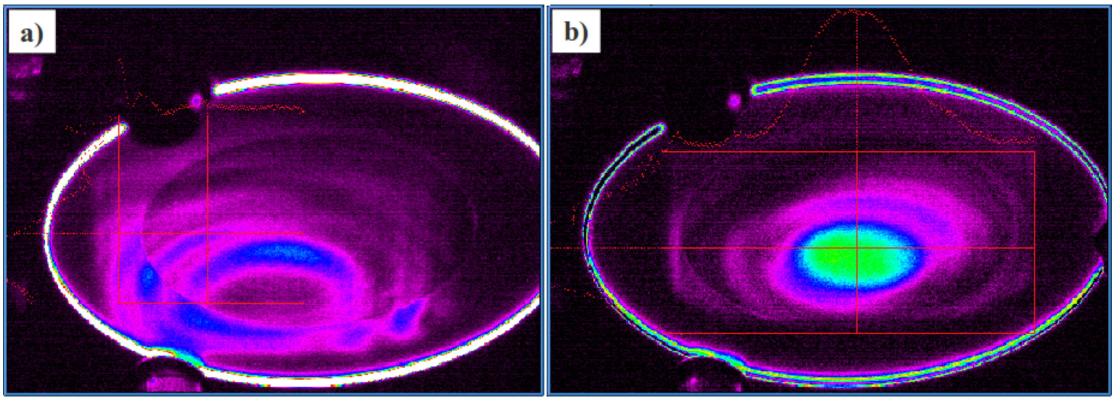

Figure 5.6: Comparison between an a) non optimized and b) optimized FEL emission, acquired on a YAG screen.

5.2.2 FEL Spectrum

In order to determine the spectral distribution of each photon pulse it is necessary to analyze its energy components by means of a diffraction grating. Each grating is designed to deliver and focus the incoming radiation onto spectrometer composed of a YAG crystal, imaged by a CCD detector [60] that is part of PADReS (Fig. 5.7).

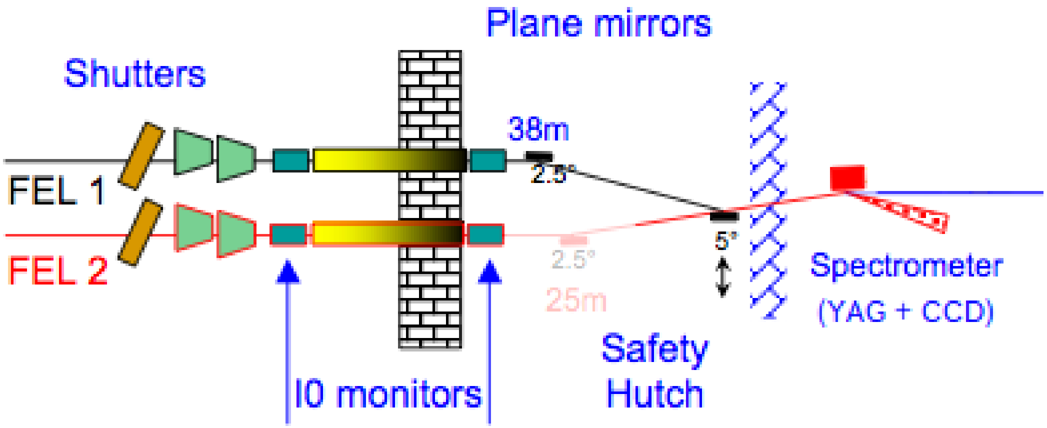

Figure 5.7: Layout of PADReS.

First we measured the spectrum of the harmonic emission at 52 nm before the optimization. This is presented in Fig. 5.8. To measure the number of photons we make use of the Intensity Monitors (I0 monitors) that take advantage of the atomic photo-ionization. The photon beam traveling through a rare gas-filled chamber generates ions and electrons that are then extracted and collected separately [61]. Using the currents generated this way it is possible to derive the absolute number of photons per pulse. The result in this case is 6×10^{11} for a compressed electron beam.

The estimation of the spectral width of the coherent signal gives us a bandwidth $\Delta\lambda$ of about 0.28 nm FWHM. If we assume for the harmonic the same pulse duration of the seed pulse (100 fs,

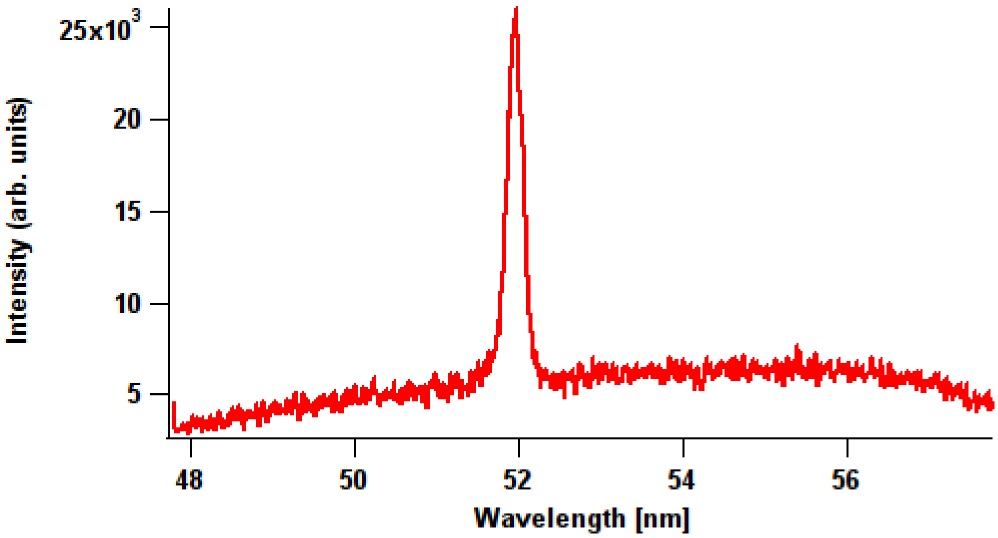

Figure 5.8: Non optimized spectrum of FEL radiation at 52 nm.

FWHM), this value is 7.29 times above the Fourier limit[1], the latter being determined according to the following relation [62],

$$c\Delta t\frac{\Delta\lambda}{\lambda^2} = 0.441, \tag{5.1}$$

where Δt and $\Delta\lambda$ are FWHM quantities (c is the speed of light). This result is quite large and is probably due to the fact that we are still far away from bunch saturation.

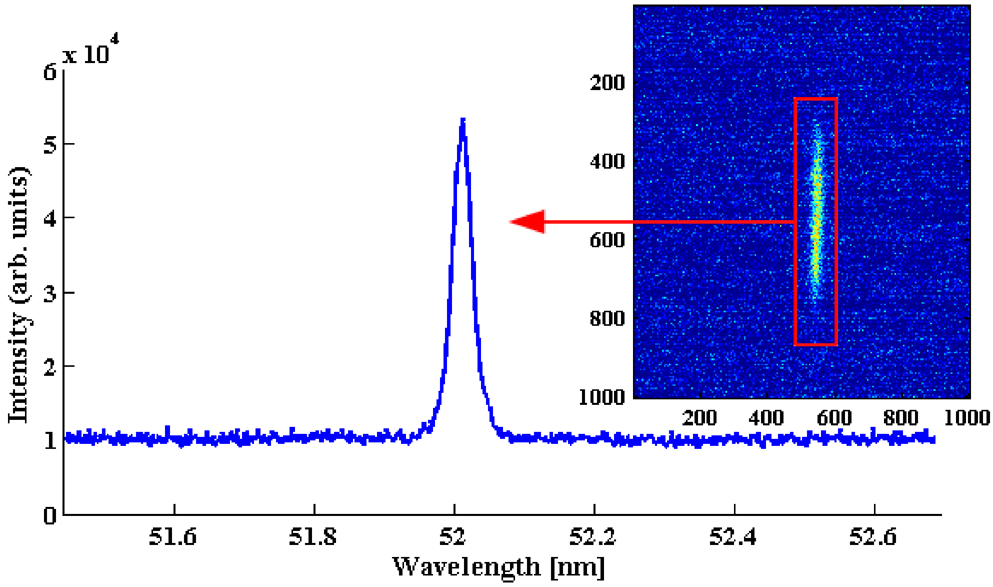

Figure 5.9: The spectrum of coherent harmonic radiation at 52 nm.

The spectrum of the coherent emission after optimization is shown in Fig. 5.9. The number of photons in one pulse is 2.7×10^{12} for a compressed beam. We also measured a bandwidth $\Delta\lambda$ of about 0.08 nm FWHM. This is 2.01 times above the Fourier limit. This is a significant improvement for the optimized case in both number of photons and bandwidth.

---

[1] In ultrafast optics, the Fourier limit is defined as the lower limit for the pulse duration for a given optical pulse spectrum.

5.3 Effect of the Seed Laser on the Electron Bunch

We observed the effect of the external seed laser on the electron beam and on the FEL spectrum. The electron beam profile was measured in the main beam dump area at the end of the undulator area, on a YAG screen (see Fig. 1.2, Chapter 3).

Fig. 5.10 shows the electron beam after the interaction of the laser. This figure gives us the electron bunch energy profile. The energy profile is a consequence of the electrons passing through a dipole magnet. Particles with different energies will perform different paths and collide at different positions on the screen.

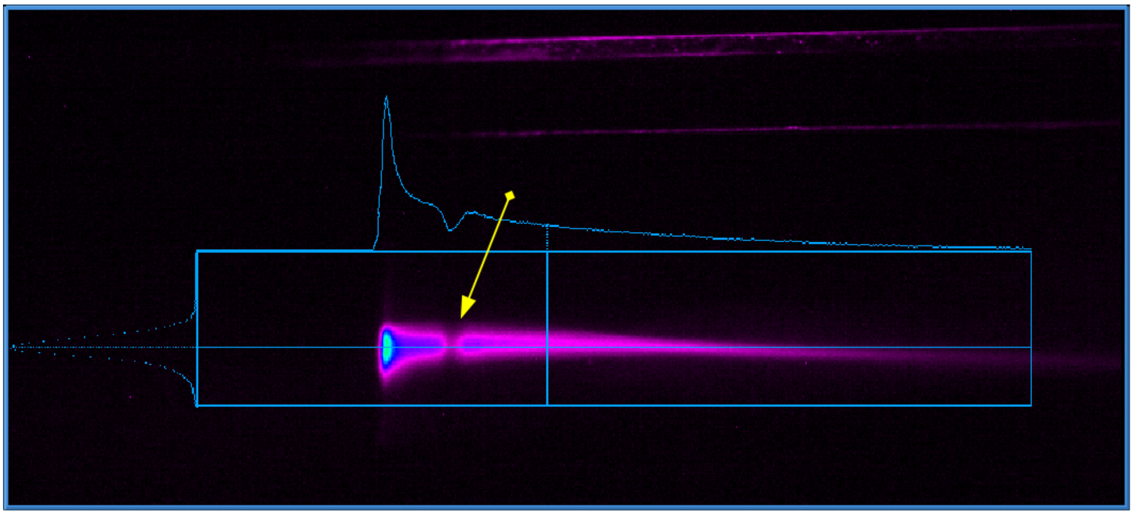

Figure 5.10: The effect of the seed laser on the electron beam. The arrow indicates the spot of the interaction of the electron beam with the seed laser.

The effect of a seeding process is clearly visible. We observe the appearance of a hole in the point (indicated by the arrow) where the seed laser interacts with the electron bunch. The hole is generated by the fact that electrons are either accelerated or decelerated due to the interaction with the seed laser. Due to the large horizontal dispersion induced by the seed, the electrons are moved away from their initial position and as a result we observe this “hole” in the electron distribution. The dimensions of the hole increases with the increase of the seed laser power. This is a clear signature of the superposition of the electron beam and the seed laser and can be used as a diagnostics to switch on the laser.

Also, as the beam goes in overbunching, there is an increase in the bandwidth of the spectrum and a second peak starts appearing, as seen in Fig. 5.11. This is due to the increase of the energy chirp and a loss of coherence in the electron beam. Basically, we have FEL emission at very different wavelength.

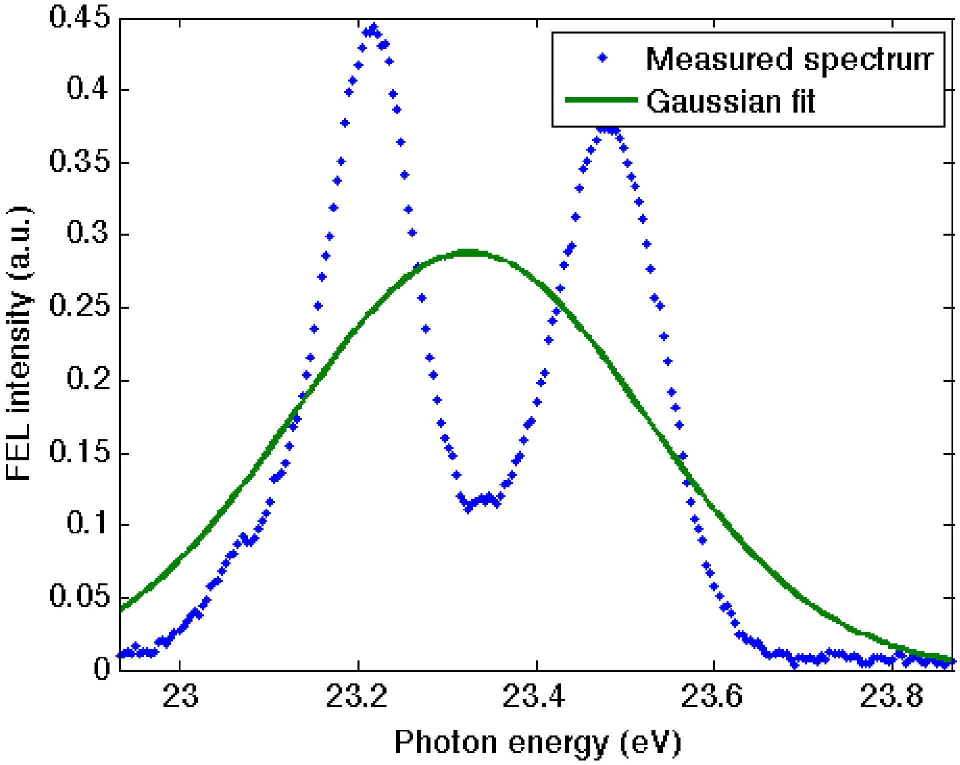

Figure 5.11: The appearance of a second peak in the FEL spectrum due to the overbunching and chirp in the electron beam distribution.

5.4 Bunch Length Compression

Fig. 5.12 shows multiple FEL acquisitions on the Intensity Monitor with an uncompressed electron beam. Every dot on the figures corresponds to a measurement and the line represents the average value. The average value of fluctuations for the uncompressed beam is $(33 \pm 1) \times 1000$ ionization points.

Fig. 5.13 shows measurements with a compression factor 4. The average fluctuations value is $(58 \pm 2) \times 1000$.

We can see that the compressed beam produces less stable but more intense radiation compared to the uncompressed beam. This is of course related to the increase of peak current and time jitter that is the result of bunch compression (Section 4.2.4). The time jitter results in the seed laser interacting with different parts of the electron bunch every consecutive time. The compressed electron beam is much less homogeneous in terms of charge and energy distribution and this translates in larger fluctuations of the FEL emission. The increase in intensity for the compressed beam is due to the increase of the peak current and as a consequence an increase in the charge density.

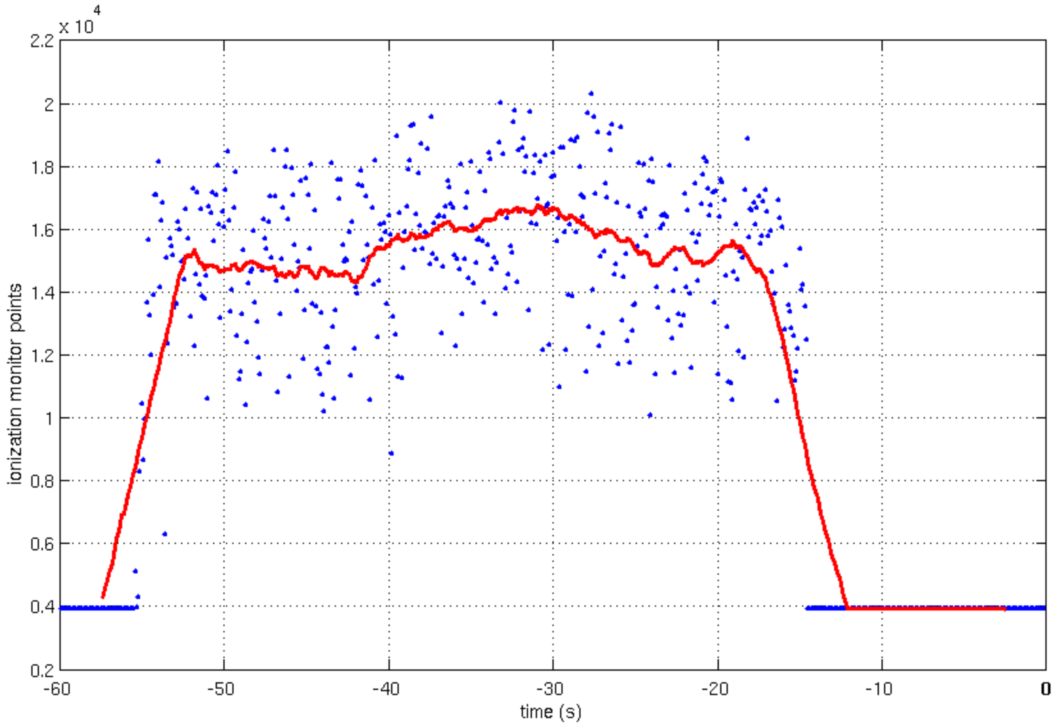

Figure 5.12: FEL with uncompressed electron beam: more stable, less intense.

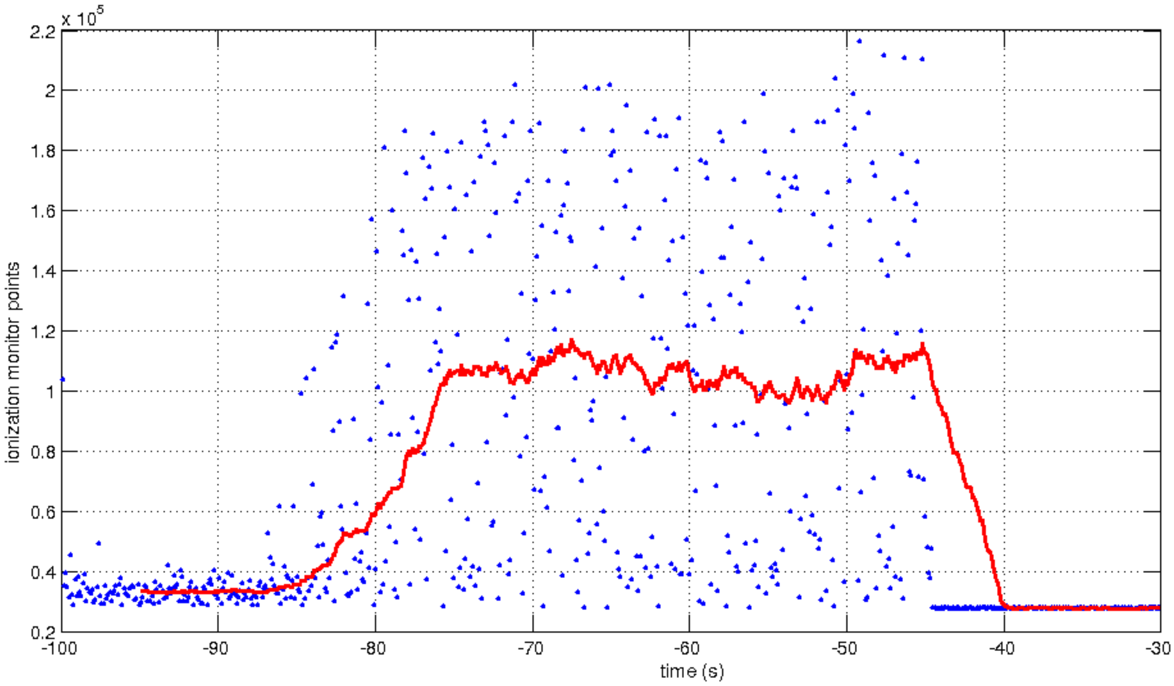

Figure 5.13: FEL with compressed electron beam (compression factor 4): less stable, more intense.

Chapter 6

GENESIS Simulations

6.1 Introduction

To get a complete characterization of the coherent harmonic radiation, we carried out detailed simulations using the 3-dimensional FEL code GENESIS [63]. The aim was to reproduce the experimental results, understand the role of the main parameters and also possibly find improvements to the FEL performance. In GENESIS, the electron beam is represented by macroparticles (a particle with N-times the charge and mass of the electron) propagating in their 6D phase space (x, y, z, p_x, p_y, p_z) and contains all the characteristics of the beam (energy, emittance, energy spread, bunch length and so on). The user has the option to generate the initial distribution of the radiation field and macro-particles as well as the magnetic field of the undulator, or to supply the explicit description of these distributions by additional input files [64].

Simulations can be run either in time-dependent or time-independent mode. Time-independent simulations are based on the assumption of an infinitely long electron bunch and radiation field with no longitudinal variation of any parameter. The time-dependent simulations take into account the finite duration of the electron beam, the possible variations in its longitudinal (i.e. current and energy) and transverse shapes, as well as the longitudinal shape and the FEL spectrum. A description of the GENESIS simulation parameters is presented in Appendix A.

6.2 Preliminary (time-independent) Calculations

The purpose of these preliminary simulations is to find the values of the seed power, dispersive section strength, modulator and radiator wavelengths at which the optimal output radiation power is obtained. For this reason, we run a large number of simulations with slightly different (randomly varying) values of the above mentioned parameters, and observe the obtained output power. All parameters are varied at the same time. This is a different scan than in the previous Chapter where we varied only one parameter at the time.

The central power of the seed is 12 MW, with random values generated in the range from 11 to 13 MW. In Fig. 6.1 the power emitted at the end of the radiator at the 5th harmonic (52 nm) is plotted versus the power of the seed laser. From this figure we can see that the power of the

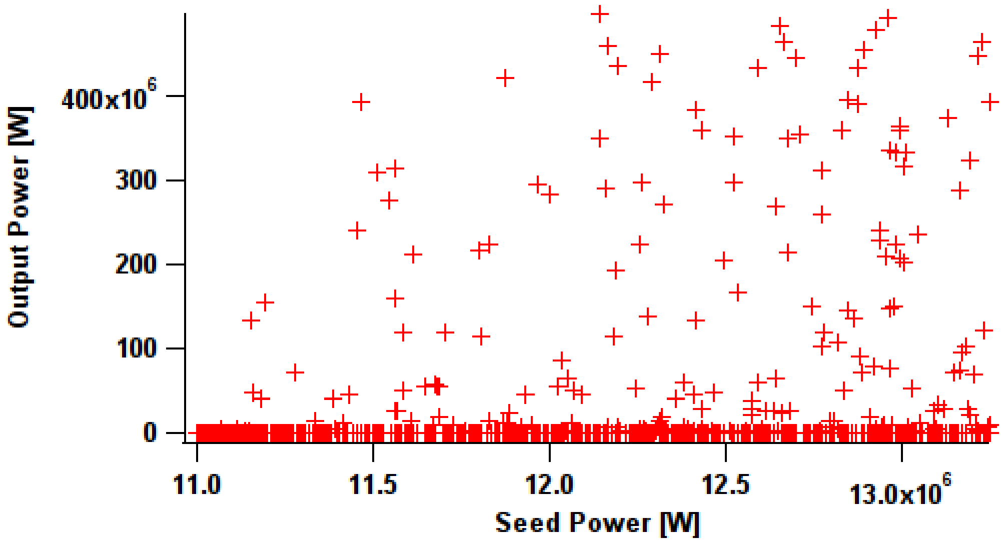

Figure 6.1: Output power at 52 nm as a function of the seed power.

radiation is growing with the seed power. This means that the seed power is not strong enough to induce the overbunching of the electron beam.

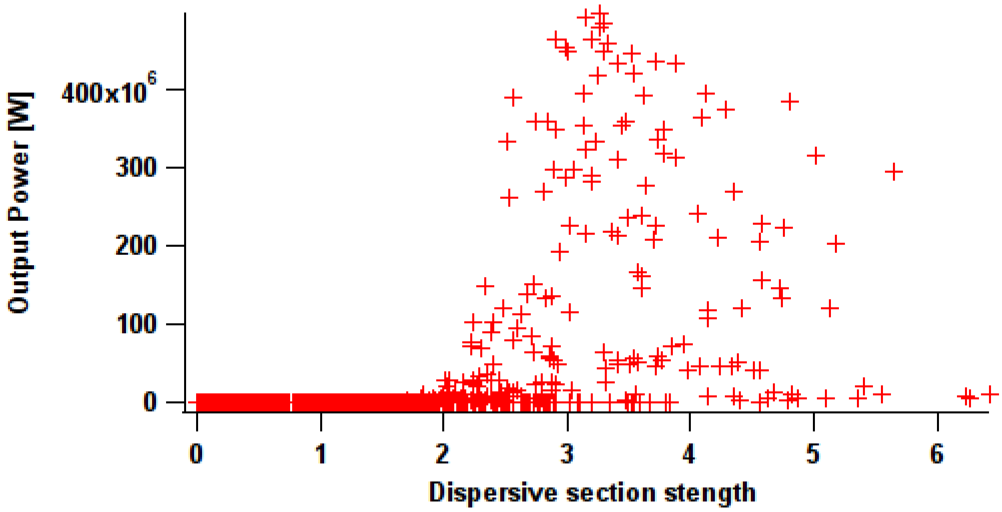

Figure 6.2: Output power at 52 nm as a function of the dispersive section strength (in "GENESIS" units).

In Fig. 6.2 we show the results on the dependence of the output power on the dispersive section strength. We see that the output power is increasing till it reaches a peak. After it there is a decrease in the output power due to the overbunching of the electron beam.

Fig. 6.3 shows the output power with respect to the selected modulator wavelength and Fig. 6.4 is the output power with respect to the radiator wavelength. Predictably, the highest output power for the modulator is close to the wavelength of the seed laser (260 nm) and for the

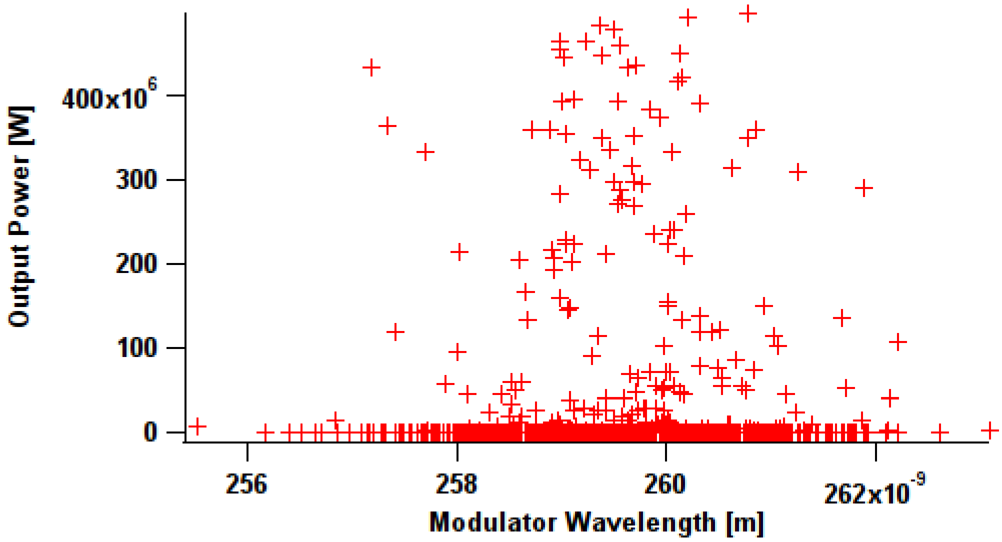

Figure 6.3: Output power as a function of the tuned wavelength of the modulator.

radiator is close to its 5th harmonic (52 nm). The reason for this scan is the same as for the scan performed in Section 5.2.1. In the passage through the undulators, the electron loses energy and the resonance condition most be adjusted accordingly.

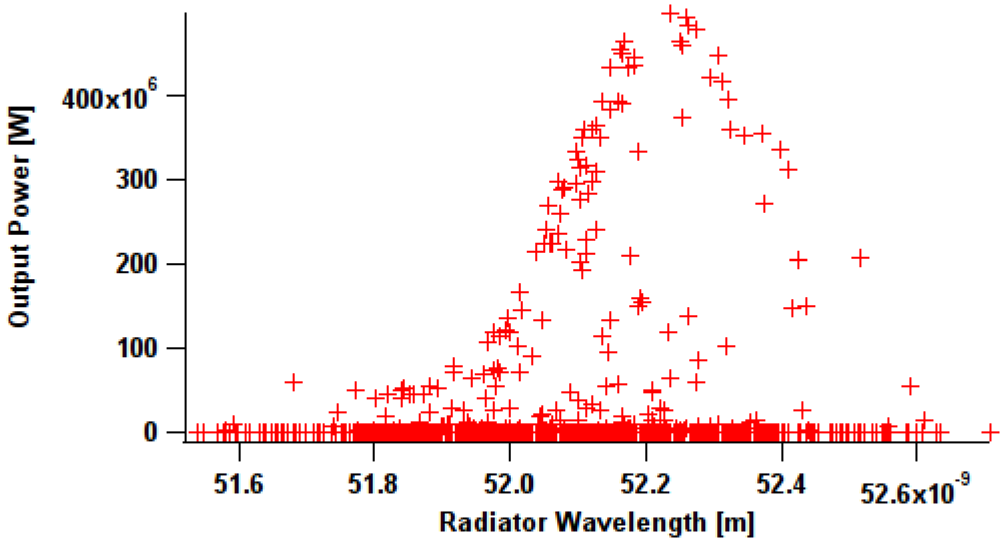

Figure 6.4: The output power as a function of the tuned wavelength of the radiator.

6.3 Expected Performance: Time-Dependent Mode

We performed simulations in time-dependent mode using the parameters obtained from the preliminary calculations in terms of seed laser power, dispersive section strength, modulator and radiator wavelengths. The values of this parameters is reported in Table 6.1. Appendix B gives the input files for simulations.

Table 6.1: Main Parameters used to during the time dependent simulations.

Parameter	Value
Beam Energy (GeV)	1.2
Seed Power - slight overbunching (MW)	12.5
Seed Power - deep overbunching (MW)	28
Modulator Wavelength (nm)	259.531
Radiator Wavelength (nm)	52.222

6.3.1 Seed Laser

For the seed laser we assumed a Gaussian profile with a peak power of 12 MW and a FWHM duration of 100 fs, see Fig. 6.5.

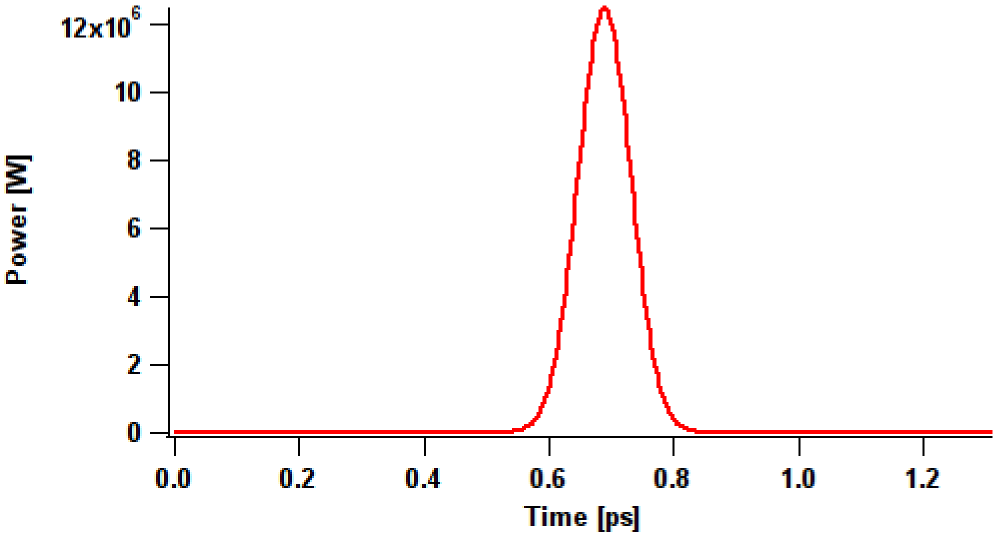

Figure 6.5: Temporal profile of the seed laser.

6.3.2 Electron Beam

The profile of the electron bunch used in the simulations in terms of current vs. time, is shown on Fig. 6.6a. The beam energy profile at the beginning of the undulator, before the interaction with the external seed is shown in Fig. 6.6b. The figure represents only a small portion of the electron beam because we are interested only in what happens to the seeded part of the bunch. We see that the energy of the electrons is decreasing with time. This means that the density of the electrons is smaller at the beginning of the bunch but this electrons are more energetic. This is usually the case after compressing the beam.

We looked at the energy profile of the electron beam at the end of the radiators. The result is shown in Fig. 6.7. Compared to the electron beam energy at the beginning of the modulator (see

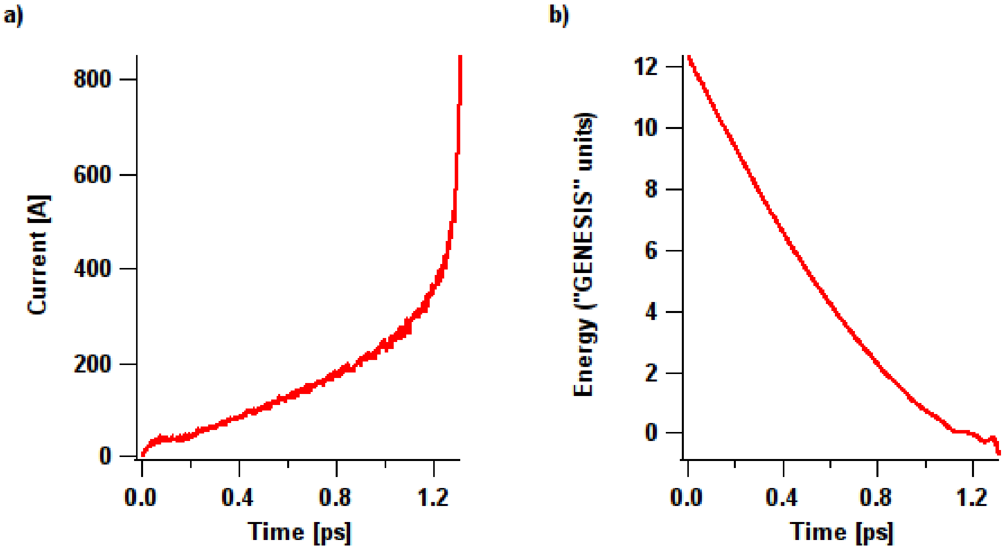

Figure 6.6: a) The profile of the electron bunch in terms of current vs. time; b) the electron beam energy (in GENESIS units) at the beginning of the modulator vs. time.

Fig. 6.6b), a gap appears in the spot of the interaction with the seed laser. This corresponds to the hole shape of the transverse profile we measured in the experiments (Fig. 5.10, Chapter 5).

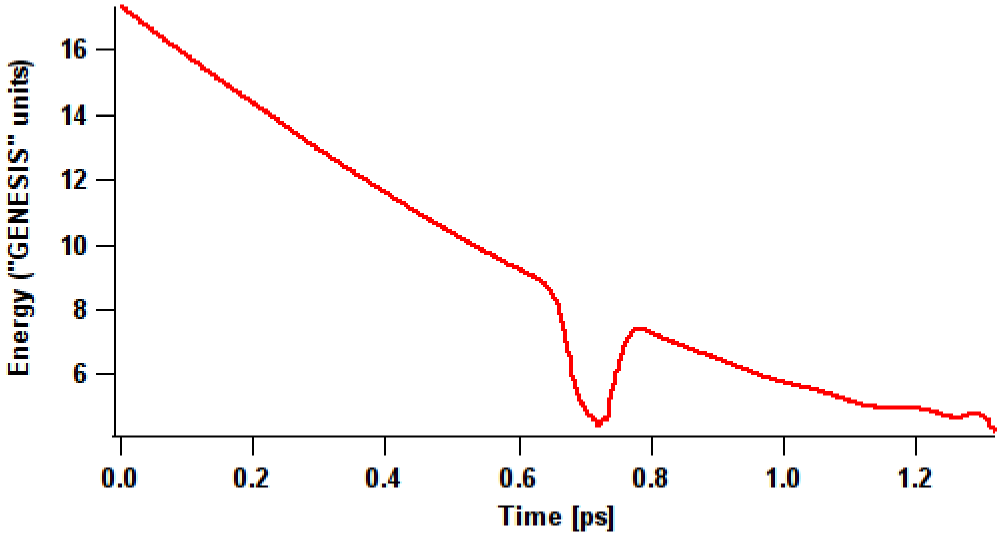

Figure 6.7: The electron beam energy profile at radiator exit.

6.3.3 Performance

As explained in Section 2.4.5, the interaction with the electromagnetic wave of the seed laser induces a modulation of the electron energy. The energy modulation evolves into bunching when the beam crosses the dispersive section. Fig. 6.8 top shows the bunching evolution. On the left there is the bunching profile in terms of the bunching factor (see Eq. 2.89 in Chapter 2) at the beginning of the modulator (before the interaction with the seed laser). The bunching profile at the entrance of the radiator is shown on the bottom. From this we can see the effect of the beam interaction with the seed laser: from a random distribution of electrons at the entrance of the modulator we get an ordered state.

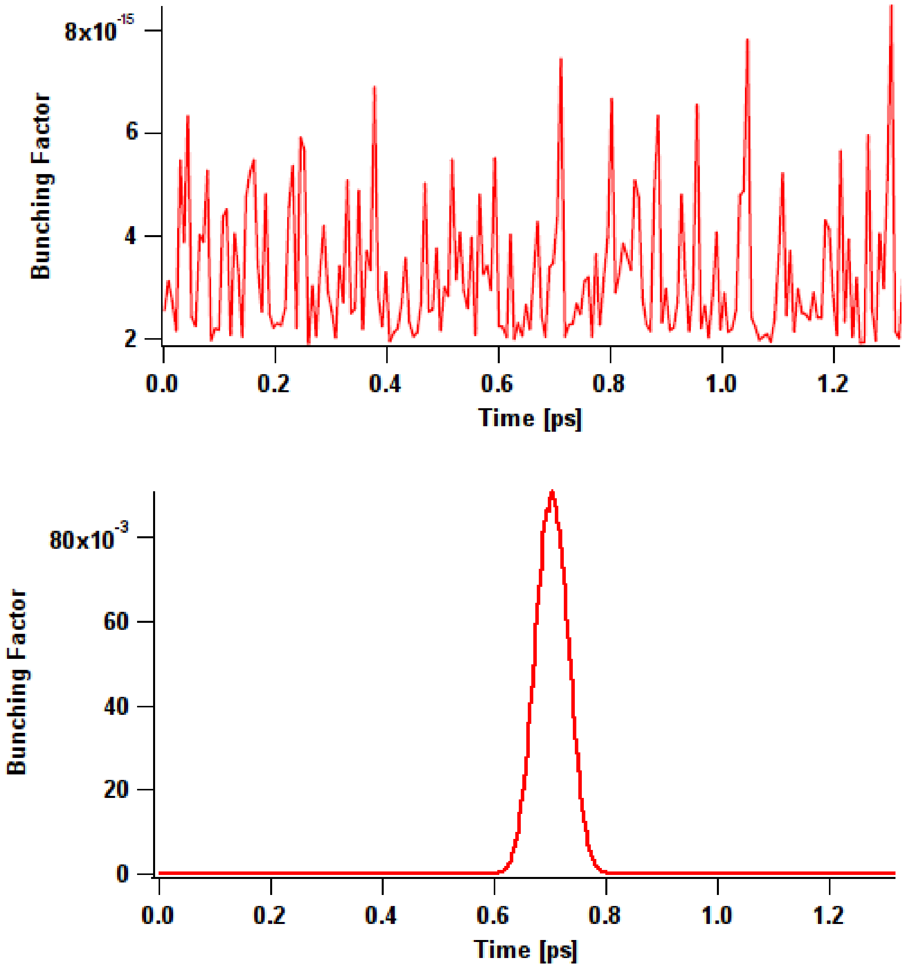

Figure 6.8: (*Top*) Bunching at the beginning of the modulator and (*bottom*) bunching at the entrance of the radiator.

As the beam proceeds further inside the undulator, the process reaches saturation and after it electrons start to loose their coherence. We observed two different cases. First we observed the performance with the beam that just reached saturation and is slightly in overbunching inside the radiators. In the second case we increased the power of the external seed laser and the beam went deep into overbunching.

Slight Overbunching

We now observe the case of the beam in slight overbunching at the entrance of the radiator. The seed laser power was 12.5 MW. Fig. 6.9 shows the bunching profile for the electron beam slightly in overbunching at the exit of the radiator.

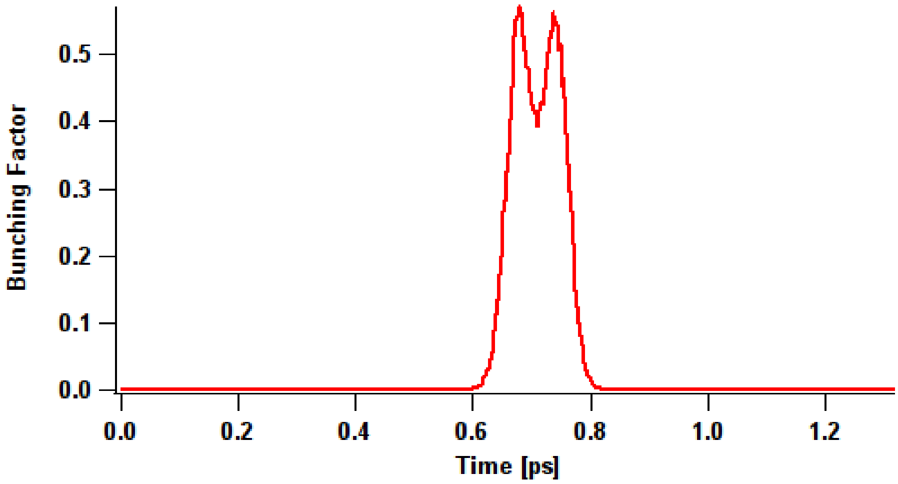

Figure 6.9: Bunching profile at the exit of the radiators.

In Fig. 6.10a we report the temporal profile of the FEL emission at the radiator exit. The measured output power is about 300 MW and the pulse duration os 40 fs. Fig. 6.10b shows the corresponding spectrum of the coherent radiation.

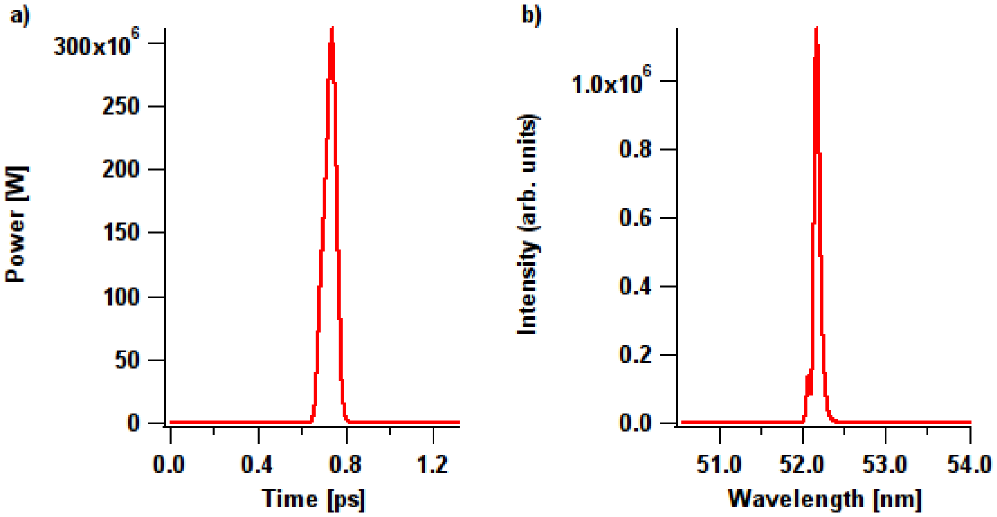

Figure 6.10: a) The temporal profile and b) spectrum of the harmonic signal with the electron beam in slight overbunching.

Performing a Gaussian fit we get the bandwidth of $\Delta\lambda = 0.05$. This is about 1.25 times above the Fourier limit. Compared with the experimental result of 2.01, this is quite a good value. Indeed, this means that the signal is much more monochromatic than in the experiment. Analyzing the spectral profile we can also calculate the number of photons in one harmonic pulse. The number is 5.5×10^{12}.

Deep Overbunching

We then simulated the electron beam in deep overbunching. Fig. 6.11 shows the bunching profile at the end of radiators. This was done by increasing the seed laser power to 28 MW.

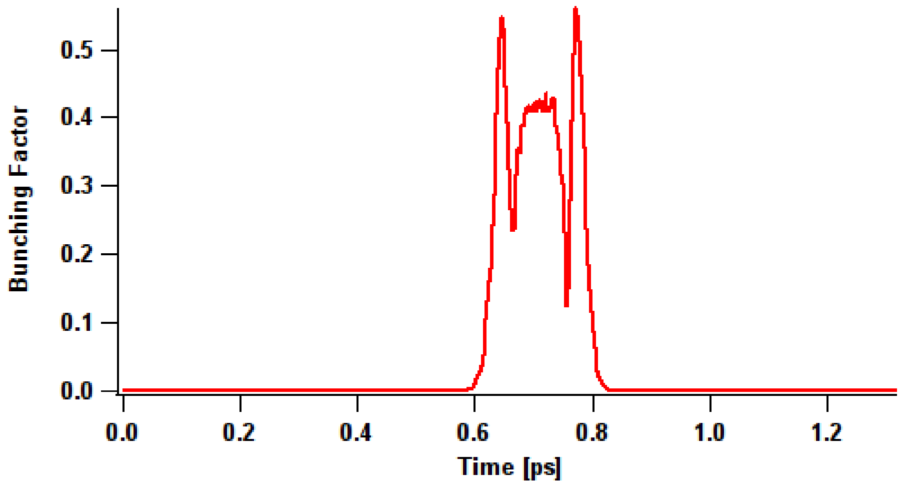

Figure 6.11: The electron beam in deep overbunching.

Again we observed the FEL temporal profile (Fig. 6.12a) and the spectral profile (Fig. 6.12b). Compared to the beam in slight overbunching, we notice a significant increase in the output power (more than 500 MW). On the other hand, the spectrum bandwidth is broader, $\Delta\lambda = 0.09$. This is about 2.26 times above the Fourier limit and is quite large.

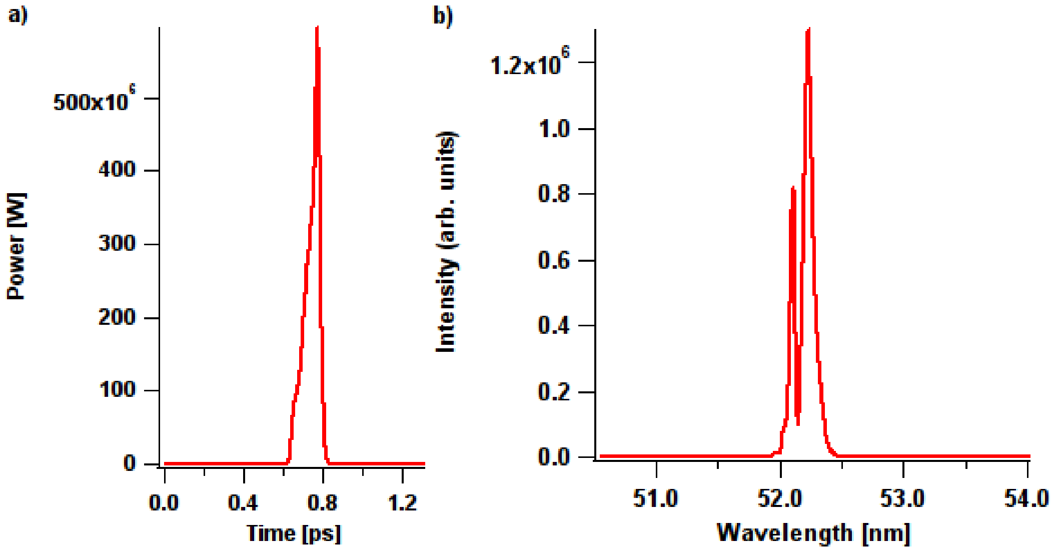

Figure 6.12: a) The output power and b) FEL spectrum.

Analyzing the spectral profile we calculated the number of photons in one pulse. The result is 9.3×10^{12}. We also observe the appearance of a larger second peak. This double peak was also observed during experiments and is due to the increase of energy chirp and a loss of coherence of the electron beam in overbunching (Section 5.3).

6.4 Comparison: Experiments vs. Simulations

In Table 6.2 we present the comparison between simulations and experiments in terms of number of photons per pulse and spectral width.

Table 6.2: Comparison between experiments and simulations.

	Experiments	**Simulations**
Number of Photons	Optimized case: 2.7×10^{12}	Slight overbunching: 5.5×10^{12} Deep overbunching: 9.3×10^{12}
Spectral Width $\Delta\lambda$ [nm]	Optimized case: 0.08	Slight overbunching: 0.05 Deep overbunching: 0.09

FERMI@Elettra is passing from the commissioning phase to the first user experiments and normally, we are still far from the optimum performance. Compared to the experiments, the simulations overestimate the number of photons in both cases. This discrepancy can be in part attributed to the fact that simulations assume a perfect spatial and temporal overlap between the seed pulse and the electron bunch inside the modulator, while such conditions were only partially met in experiments.

Also, the spectral width obtained in experiments is between the case of slight overbunching and deep overbunching. There is no obvious reason for this spectral width degradation but is probably due to the non-optimized electron beam.

Chapter 7

Conclusion and Perspective

Harmonic Generation using Free Electron Lasers (FELs) is motivated by the fundamental and challenging need of generating good quality radiation in VUV/X-ray spectral region, beyond the reach of conventional light sources. Good quality means: high flux, spatial and temporal coherence, adjustable duration (great interest mainly to short-fs-pulses) and good stability. Achieving this challenging goal will provide the opportunity to open the path to more detailed investigations of many new areas of science.

Due to the lack of mirrors in VUV/X-ray spectral region, the standard approach relies on single-pass configurations, i.e. Self-Amplified-Spontaneous-Emission (SASE) and Coherent Harmonic Generation (CHG). CHG is based on the frequency up-conversion of a high-power seeding signal focused into an undulator, which is normally the first one of an optical klystron configuration, and synchronized with the incoming electron bunch. Contrary to SASE, CHG is capable of producing temporally and spatially coherent pulses. When implemented on linear accelerators, both SASE and CHG are characterized by a poor shot-to-shot stability. Indeed, they show strong sensitivity to fluctuations of initial conditions, e.g. electron-beam energy, energy spread, current, emittance (and seed characteristics in the case of CHG). In linac-based devices fluctuations are in general quite strong.

Physics of single-pass free electron lasers has been studied theoretically for many years but very few experimental results are presently available (Desy for SASE and Brookhaven for CHG). On the other hand, many proposals and several funded projects exist to build such sources. So, there is a great interest in experimental results benchmarking theory and opening up new perspectives.

Motivated by the above considerations, we have performed experimental study of the FEL commissioning and CHG on the FERMI@Elettra. The experimental activity was done in the time period from 16 May 2011 to 24 July 2011. The goal of this commissioning run was to make the FERMI FEL radiation available for the users experiments. During this time I was actively involved in the experimental activity. My contribution involved regular participation in the shifts and also independently performing various measurements. For example, measurements of the electron beam profile, its energy spread and investigating the relationship between length compression and jitter of the electron bunch arrival time. I also run GENESIS simulations in order to get a comparison between theory and experiments. The results show that a FEL based on a linear accelerator can be a competitive light source. The FERMI FEL covers the lower energy region of the XUV spectrum. With peak brightness orders of magnitude greater than synchrotron light sources, pulse length of the order of femtoseconds, variable polarization and energy tunability, the FERMI source has the potential of becoming a powerful tool for scientific exploration in a wide spectrum of disciplines

In Section 3.9 we presented the expected performance obtained performing a series of start-to-end simulations. Comparing with the obtained result during the commissioning and harmonic generation, we can see that the FERMI@Elettra is still far from the expected performance terms of photons per pulse ($\sim 10^{12}$ measured vs. $\sim 10^{13}$ predicted). The main future task lies in the optimization and stabilization of the electron bunch. Still, significant progress has been made during the commissioning and now we are already able to provide coherent emission for the user's experiments.

Plans for the future also include increasing the beam charge (500 - 800 pC), installing the second bunch compressor and an X-band RF structure prior to the first bunch compressor in order to linearize the longitudinal phase of the electron beam. This will increase the intensity and stability of the FEL output.

Appendix A

Description of GENESIS parameters

Table A.1: A description of the input parameters for GENESIS simulations.

Parameter	**Description**	**Unit**
AW0	The normalized, dimensionless rms undulator parameter.	unitless
XLAMD	The undulator period lenght	meter
GAMMA0	The mean energy of the electron beam in terms of the electron rest mass energy.	unitless
DELGAM	The rms value of the energy distribution in terms of electron rest mass energy	unitless
RXBEAM	The rms value in x of the transverse, spatial distribution	meter
RYBEAM	The rms value in y of the transverse, spatial distribution	meter
EMITX	The normalized rms emittance in x	meter
EMITY	The normalized rms emittance in y	meter
ALPHAX	Rotation of the transverse phase space distribution in x	unitless
ALPHAY	Rotation of the transverse phase space distribution in y	unitless
XLAMDS	The resonant radiation wavelength	meter
PRAD0	The input power of the radiation field	Watt
NWIG	The number of periods within a single undulator module	unitless
CURPEAK	Peak current of the electron beam.	Amperes
IBFIELD	Magnetic field of the dispersive section	Tesla

Appendix B

Input files for GENESIS

The input files for GENESIS used in Section 6.1.3. are presented in Table B.1

Table B.1: The input files for GENESIS simulations.

MODULATOR	
AW0	5.3459
XLAMD	0.10
GAMMA0	2.385000E+03
DELGAM	3.400000E-02
RXBEAM	6.49143E-005
RYBEAM	7.45299E-005
ALPHAX	-0.300775
ALPHAY	0.636789
EMITX	1.5E-6
EMITY	1.5E-6
XLAMDS	2.5953154E-007
PRADO	1.1841076E+008
NWIG	30
CURPEAK	200
RADIATORS	
AW0	3.1234
XLAMD	5.500000E-02
GAMMA0	2.385000E+03
DELGAM	3.400000E-02
RXBEAM	5.391170E-05
RYBEAM	4.082330E-05
ALPHAX	9.300360E-01
ALPHAY	-6.180000E-01
EMITX	1.5E-6
EMITY	1.5E-6
XLAMDS	5.2227475E-008
PRADO	1.1841076E+008
NWIG	36
CURPEAK	200
IBFIELD	1.5937907E+000

Bibliography

[1] DELSY, http://wwwinfo.jinr.ru/delsy/

[2] G. C. Baldwin, Origin of Synchrotron Radiation, *Physics Today* **28**, No. 1 (1975) 9.

[3] T. Shintake, Proceeding of PAC07, Albuquerque, New Mexico, USA (2007).

[4] K.J. Kim, 'Three-Dimensional Analysis of Coherent Amplification and Self-Amplified Spontaneous Emission in Free-Electron Lasers", *Phys. Rev. Lett.* **57**, 18711874 (1986).

[5] L. H. Yu, "Generation of intense uv radiation by subharmonically seeded single-pass free-electron lasers", *Physical Review A*, **44**, 8, (1991).

[6] See http://www.elettra.trieste.it/FERMI/

[7] E. Allaria, G. De Ninno, M. Trovo, Proceedings of FEL 2006, BESSY, Berlin, Germany.

[8] *FERMI@elettra Conceptual Design Report*, Chapter 3, Trieste, Italy (2007) p. 41.

[9] LEUTL, http://www.aps.anl.gov/aod/mcrops/leutl

[10] VISA, http://lcls.slac.stanford.edu/

[11] Tesla Test Facility, http://tesla-new.desy.de/

[12] Talk by T. Shintake, "Status of the SCSS Prototype Accelerator and XFEL Project in Japan", EPAC2006.

[13] LCLS, http://lcls.slac.stanford.edu/

[14] X.J. Wang et. al., Proceeding of FEL 2006, BESSY, Berlin, Germany.

[15] SPARC, http://www.lnf.infn.it/acceleratori/sparc/

[16] A. Renieri, Proceeding of the 27th International Free Electron Laser Conference, Stanford, California, USA.

[17] B. Girard et. al., *Phys. Rev. Lett.* **53**, 2405 (1984).

[18] M. Labat et al., *Eur. Phys. J.* D **44**, 187 (2007).

[19] K. Willie; *The Physics of Particle Accelerators, and introduction*, Oxford University Press, 2005, p. 45.

[20] E.B. Courant, H.S. Snyder, Theory of the Alternating Gradient Synchrotron, *Ann. Phys.* **3**, 1-48 (1958).

[21] H. Wiedemann; *Particle Accelerator Physics*, Third Edition, Springer, 2007, Chapter 6, p. 191-235.

[22] *ibid.*, p. 197.

[23] *ibid.*, p. 206.

[24] T.P. Wangler; *Principles of RF Linear Accelerators*, John Wiley & Sons, 1998, Chapter 11, p. 314-330.

[25] H. Wiedemann; *Particle Accelerator Physics*, Third Edition, Springer, 2007, Chapter 19, p. 680.

[26] K. Willie; *The Physics of Particle Accelerators, and introduction*, Oxford University Press, 2005, p. 217.

[27] P. Schmuser, M. Dohlus, J. Rossbach; *Ultraviolet and Soft X-Ray Free-Electron Lasers*, Springer, 2008, Chapter 3, p. 33.

[28] *ibid.*, p. 34.

[29] *ibid.*, p. 32.

[30] F. Curbis, *Generation of VUV ultra-short coherent optical pulses using electron storage rings* PhD Thesis, University of Trieste, 2008, Chapter 2, p. 38.

[31] L.H. Yu, *Phys. Rev. A* **44**, 5178 (1991).

[32] http://www.elettra.trieste.it/FERMI/

[33] R. Coisson and F. De Martini, *Quantum Electronics* **9** (1982) 939.

[34] R. Bonifacio et al., *Nucl. Instrum. and Meth. A* **296** (1990) 787.

[35] L.H. Yu, *Phys. Rev. A* **44** (1991) 5178.

[36] *FERMI@elettra Conceptual Design Report*, Chapter 2, Trieste, Italy (2007) p. 29.

[37] M. Trovo et al., Proceedings of FEL 2006, BESSY, Berlin, Germany.

[38] D. Palmer, *The next generation photoinjector*, Stanford University dissertation, 1998.

[39] A. Zholents et al., *Formation of Electron Bunches for Harmonic Cascade X-Ray Free-Electron-Lasers*, Phys. Rev. Spec. Topics Accel. Beams, **9**, 120701 (2006).

[40] M. Cornacchia et al., PRST-AB 10th European Particle Accelerator Conference, EPAC2006 (2006).

[41] *FERMI@elettra Conceptual Design Report*, Chapter 5, Trieste, Italy (2007) p. 108.

[42] M. Cornacchia et al., ST/F-TN-06/15 (2006).

[43] *FERMI@elettra Conceptual Design Report*, Chapter 6, Trieste, Italy (2007) p. 144.

[44] W. Fawley and G. Penn, *Thoughts on Spectral Broadening Effects in FERMI and other FELs Based upon Seeded Harmonic Generation*, ST/F-TN-06/07, May 2006.

[45] D. La Civita et al., Proceedings of PAC07, TUPMN030, Albuquerque, New Mexico, USA.

[46] I. Ben-Zvi, K.M. Yang, and L.H. Yu, *Nucl. Inst. Meth. A* **318**, 726 (1992).

[47] Coherent, http://www.coherent.com

[48] E. Allaria et al., *FERMI@ELETTRA: A SEEDED FEL FACILITY FOR EUV AND SOFT X-RAYS*, Proceedings of FEL 2006, BESSY, Berlin, Germany (2006).

[49] *FERMI@elettra Conceptual Design Report*, Chapter 4, Trieste, Italy (2007) p. 82-101.

[50] *FERMI@Elettra Conceptual Design Report*, Trieste, Italy (2007).

[51] P. Craievich et al., Proceedings of FEL2010, WEPB43, Malm, Sweden.

[52] H. Wiedemann; *Particle Accelerator Physics*, Third Edition, Springer, 2007, Chapter 2, p. 60.

[53] R. L. Gluckstern and L. Smith, Fermilab Preprints, FERMILAB-FN-0199, 1969.

[54] F. J. Decker et al., Stanford Linear Accelerator Center Publications No. SLAC-PUB-7260, 1996.

[55] M. Veronese et al., Proceedings of FEL 2006, THPPH029, BESSY, Berlin, Germany.

[56] G. D'Auria et al., Proceedings of IPAC10, TUPE015, Kyoto, Japan.

[57] M. Petrinio, *Research and Applications of Radio-Frequency Deflecting Cavities*, Phd Thesis, Universita degli studi di Trieste, Chapter 3, p. 49 (2010).

[58] R. Assmann and A. Chao, Dispersion in the Presence of Strong Transverse Wakefields. Proc. 17th IEEE Part. Acc. Conf. (PAC 97), Vancouver, Canada, 12-16 May 1997. SLAC-PUB-7577.

[59] http://www.elettra.trieste.it/FERMI/index.php?n=Main.Science

[60] G. Gaio et al., Proceedings of PCaPAC 2010, WEPL018, Saskatoon, Saskatchewan (2010).

[61] M. Zangrando, Proceedings of FEL2010, FROAI2, Malm, Sweden (2010).

[62] J.-C. Diels and W. Rudolph, "Ultrashort Laser Pulse Phenomena", Second Edition, Elsevier, Chapter 1 (2006).

[63] S. Reiche, http://corona.physics.ucla.edu/∼reiche/

[64] S. Reiche, "Numerical Studies for a Single Pass High Gain Free-Electron Laser"", PhD Thesis, Hamburg University, Chapter 4, 1999.